This electronic thesis or dissertation has been downloaded from the King’s Research Portal at https://kclpure.kcl.ac.uk/portal/

Light-Matter Interactions of Metal-Semiconductor Nanostructures

Po, Steve

Awarding institution:
King's College London

The copyright of this thesis rests with the author and no quotation from it or information derived from it may be published without proper acknowledgement.

END USER LICENCE AGREEMENT

Unless another licence is stated on the immediately following page this work is licensed under a Creative Commons Attribution-NonCommercial-NoDerivatives 4.0 International licence. https://creativecommons.org/licenses/by-nc-nd/4.0/

You are free to copy, distribute and transmit the work

Under the following conditions:

- Attribution: You must attribute the work in the manner specified by the author (but not in any way that suggests that they endorse you or your use of the work).
- Non Commercial: You may not use this work for commercial purposes.
- No Derivative Works - You may not alter, transform, or build upon this work.

Any of these conditions can be waived if you receive permission from the author. Your fair dealings and other rights are in no way affected by the above.

Take down policy

If you believe that this document breaches copyright please contact librarypure@kcl.ac.uk providing details, and we will remove access to the work immediately and investigate your claim.

Download date: 26. Dec. 2024

Light-Matter Interactions of Metal-Semiconductor Nanostructures

Steve Po

Supervisor:
Dr. Aliaksandra Rakovich
Dr. Francisco Rodríguez Fortuño

This dissertation is submitted for the degree of
Doctor of Philosophy

Department of Physics
King's College London
April 2023

Abstract

The field of plasmonics has been shown to possess a versatile property of localized field enhancement around noble metal nano-systems that has been researched extensively in the context of sensing, communication, and microscopy, among others. Additionally, semiconducting nanotechnologies has seen great advances in recent history owing to their attractive optical properties that has landed them in the cutting edge of research with applications into display technologies, microscopy, and sensing. Therefore, it seems natural to see the two fields joined resulting in exciting research outputs that continue to shape the way nanotechnology is studied. To this end, this thesis focuses on the combined optical behaviour of plasmonic and semiconducting nanoparticles to help advance this progressive field. Here, Quantum Dots (QDs) were used as the semiconducting nanoparticles of choice. To do so, different methods of fabrication were explored that utilises both gold nanostructures and QDs, and their optical behaviours were investigated in terms of their energy coupling and transfer.

Firstly, a relatively sophisticated lithographic method will be introduced, allowing for fine control of nanoparticle and nanostructure positioning. The viability of such a technique shall be discussed for certain industrial purposes and how recent developments may be used to overcome certain shortcomings including throughput and resolution limits related to electron scattering. Secondly, the fluorescence lifetime of an alternative gold-QD layered structure and a colloidally shelled gold-QD hybrid construction are investigated as a potential platform for light harvesting applications. For both, a pulsed laser source is used to excite the samples and the excitation behaviour over each pulse cycle is studied. It was demonstrated that the structures fabricated possess excellent optical energy transfer characteristics that may make them suitable for energy harvesting platforms.

Acknowledgements

Firstly, I express my sincerest gratitude to my supervisor Dr. Aliaksandra Rakovich who has provided me with the opportunity to learn and grow under her guidance, while providing me with an incredible level of support both academically and pastorally – particularly through a globally and personally challenging time.

I would also like to thank both Chow Tsz Him and Prof. Wang Jianfang from the Chinese University of Hong Kong for teaching me the synthesis of colloidal nanoparticles which has proved invaluable.

I thank my family for their endless love and support throughout the past four years and especially to Flurina and Valentina for their constant reminders of the joys in the world.

I am also thankful for my friends and colleagues who have provided insightful and fruitful discussions, but mostly for helping with making this a pleasant journey.

I would like to acknowledge and thank EPSRC and King's College London for funding the PhD.

Finally, I give my greatest love and appreciation to Johanna Steiner, without whom this endeavour would have been infinitely more difficult. She provided me with stability and support, and I will forever be grateful.

Steve Po

Contents

List of Abbreviations and Acronyms

μCP	Micro-Contact Printing
AFM	Atomic Force Microscope
AuNP	Gold nanoparticle
BF	Bright Field
BTN	Biotin
CAD	Computer Aided Design
CAPA	Capillary-Assisted Particle Assembly
CdSe/ZnS	Cadmium Selenide/Zinc Sulfide
CET	Cascaded Energy Transfer
CW	Continuous Wave
DF	Dark Field
DLS	Dynamic Light Scattering
DT	Dead Time
EBL	Electron Beam Lithography

ET	Energy Transfer
FLIM	Fluorescence Lifetime Imaging Microscopy
FRET	Förster Resonance Energy Transfer
IRF	Instrument Response Function
LbL	Layer-by-Layer
LDV	Laser Doppler Velocimetry
LSPR	Localised Surface Plasmon Resonance
MCS	Main Chain Scissions
OD	Optical Density
PDI	Polydispersity Index
PE	Polyelectrolyte
PL	Photoluminescence
PLQY	Photoluminescence Quantum Yield
PMT	Photomultiplier Tube
QD	Quantum Dot
QY	Quantum Yield
ROI	Region of Interest
RS	Raman Spectroscopy
SAM	Self-Assembled Monolayer

SEM	Scanning Electron Microscope
SERS	Surface Enhanced Raman Spectroscopy
SNR	Signal-to-Noise Ratio
SPAD	Single Photon Avalanche Diode
STV	Streptavidin
TCSPC	Time Correlated Single Photon Counting
UVVis	Ultraviolet - Visible

Chapter 1

Introduction

The need for energy is, globally, a constantly increasing endeavour with electricity consumption gradually climbing since records began [1]. With a shift away from non-renewable sources, such as coal and natural gas, alternative sources must be found to make up the deficit. In fact, the UK's renewable energy consumption share is increasing at an exponential rate [2, 3]. According to the International Energy Agency, of the renewable energy sources, the share of solar electricity generation globally is also increasing at an exponential rate [4]. This will only continue to grow with major economic blocs, such as China, the EU, and USA, introducing policies to increase funding for such technologies. Alongside electricity generation by renewable sources, storage is also a technological challenge that is quite active. The most common method of energy storage is in the form of hydropower, in which water is pumped uphill and stored as gravitational potential energy [5]. Another highly attractive option is through chemical storage i.e., using batteries integrated into the grid for on-demand use when power generation is low such as during the night. An emerging solution through alternative chemical storage is using Hydrogen generation by water splitting. As Hydrogen usage produces zero emissions (the only product being water after combustion), as well as having the highest gravimetric energy density, it is seen as a highly promising and attractive potential fuel source [6]. Currently, technologies often rely on electrolysis which is ill suited for commercial purposes due to high captial costs from the equipment needed and its high energy cost needed for production. A recent study by Hodges *et al.* demonstrated a water electrolysis cell with near unity efficiency with a consumption of 40.4 kWh kg^{-1} H_2 [7]. This is compared to commercially available cells with an energy consumption of 47.5 kWh kg^{-1} H_2 with 1 kg of hydrogen containing 39.4 kWh worth of energy. In recent efforts, integration of plasmonics and semiconducting nanoparticles has been seen to be a promising avenue for renewable hydrogen generation via water splitting [8].

Briefly, the main mechanism of interest is the photoexcitation of charge carriers in semiconductors from the coupled decay of plasmons. Either an electron excited in the metal with enough energy can be transferred to the semiconductor - known as indirect electron transfer - or the plasmon decay can directly excite an electron in the semiconductor to the conduction band - direct electron transfer. Through these two mechanisms, a sufficiently high energy excitation (such as a high frequency laser source) is therefore necessary to generate hot carriers [9, 10]. Although in this scheme, generated hot electrons have extraordinarily short lifetimes before they thermalize back to the Fermi-level (on the order of femtoseconds), thus the use of semiconductors are required to extract these carriers [11]. A final mechanism is the excitation of the semiconductor, producing an electron-hole pair by a resonant energy transfer processes [12, 13]. These photo-generated charge carriers can then be used to drive reduction (through the hot electrons) or oxidation (hot holes) reactions [14].

The use of plasmonics so far has been to supplement existing semiconducting materials, such as TiO_2, which alone are only active in the UV range due to its wide energy bandgap. The addition of plasmonics serves to widen the spectral region in which such a mixed plasmonic-semiconductor system can operate, allowing photoexcitation to occur in the visible region, increasing the solar harvesting efficiency. Excitingly, relatively new materials and geometries of semiconductors have been exploited and shown great optical properties that can be beneficial to solar harvesting technologies. These are known as Quantum Wells or Quantum Dots (QD - which will be discussed further in later chapters). Although plasmonics has been used previously to enhance the electron-hole pair generation in semiconductors, like QDs, the reverse process has also been demonstrated. A study by Walters *et al.* had shown to generate surface plasmons by the direct coupling of radiative decay of electrically excited QDs to plasmon modes [15, 16]. Therefore, it stands to reason that QDs of an adequately high emission energy may be able to couple to plasmon modes to generate hot carriers for further photo-chemical reactions - such as water splitting.

As the majority of Hydrogen is still generated using non-renewable sources, such as Liquefied Natural Gas, it remains a relevant and active field of research to find cleaner alternatives [17]. In this thesis, the aim is to study light-matter interactions in the context of photoexcited nanoparticles as potential energy harvesting structures. To do so, two different geometries of gold nanoparticles coupled with QDs will be studied by examining the energy transfer dynamics through fluorescence lifetime measurements. The properties of plasmonics (field enhancements) and QDs (stable, tunable photoemissions) will be exploited to create directed energy transfer (akin to a funnel) that may be attractive for purposes that require spatially concentrating the harvested energy to specific regions. Furthermore, methods to fabricate substrate based nanoparticle arrays with nanometric control will be discussed for other light-matter based applications. As the applications and concepts in each chapter are quite varied, they will be introduced individually. Overall, the main aim of this thesis is to develop methodologies to create multilayered QD platforms where each layer consists of different emission energy QDs, around gold nanoparticles which provides enhancements to the local electric field and energy transfer rates between layers of QDs.

Chapter 2

Theoretical Background

2.1 Fluorescence

The natural starting point for this work is to explore light-matter interactions, particularly the concept of photoluminscence (PL), but specifically fluorescence. In essence, this process involves the absorption and subsequent re-emission of light at a different spectral location, typically of lower energy - what we now attribute to Stoke's law [18]. However, PL is just one of the possible de-excitation pathways in which an excited fluorophore can release this absorbed energy. Other pathways include internal conversion, intersystem crossing, vibrational relaxation etc. These optical processes are often summarised graphically in a Jablonski diagram - a basic example is shown in Fig. 2.1 which principally includes the most relevant processes (absorption, vibrational relaxation, fluorescence, and energy transfer) with others omitted for clarity.

An important quantity used to characterise a fluorophore is the fluorescence Quantum Yield (QY), which is defined by the following expression [19]

$$\Phi_F = \frac{k_r}{k_r + k_{nr}}, \tag{2.1}$$

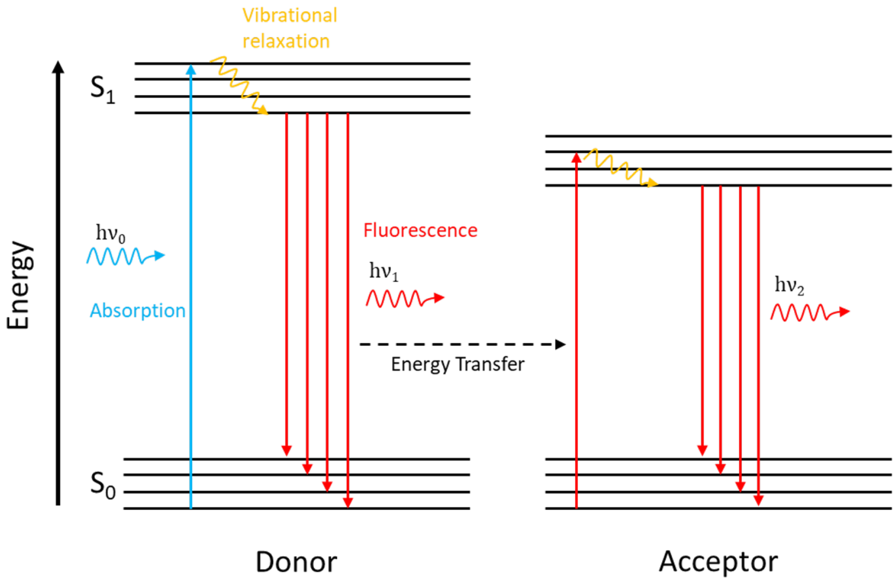

Figure 2.1: Basic Jablonski diagram demonstrating the excitation from the ground state (S_0) to the first excited state (S_1) of a fluorescing body and de-excitation via vibrational relaxation, fluorescence, and energy transfer to a nearby acceptor. Note: not all possible absorption lines are shown here for clarity and that typically $h\nu_0 > h\nu_1$ in Stoke's shift fluorescence and $h\nu_1 > h\nu_2$ for energy transfer processes.

where k_r is the radiative rate constant and k_{nr} is the non-radiative rate constant which encapsulates all possible relaxation processes that do not involve the emission of a photon. As such, the QY is the ratio between emitted and absorbed photons per unit time and volume. Therefore, a fluorophore with high QY approaching unity often displays bright emissions as most photons couple into the far-field. Another important quantity that describes the optical characteristics of a fluorophore is the fluorescence lifetime which describes the average amount of time a fluorophore stays in its excited state before relaxing to the ground state. The equation describing this fluorescence lifetime is similar to Eq. 2.1 and is given by

$$\tau = \frac{1}{k_{rad} + k_{nr}} \,. \tag{2.2}$$

Therefore, given knowledge of a fluorophore's intrinsic, average lifetime and its

QY, it is possible to calculate the proportion of radiative to non-radiative decay rates of the molecule/particle. For typical fluorescent probes, the lifetimes are generally of the order of 1-10 ns which are well within the measurement capabilities of current time-resolved spectroscopic methods which will be discussed later.

2.1.1 Energy Transfer

Non-radiative Energy Transfer (ET) is a process in which the energy of excited electrons is transported between species, typically denoted as Acceptors, A, and Donors, D, via transition dipole-dipole coupling [20–22], as illustrated in Fig. 2.1. The rate at which this resonance energy transfer occurs can be described by

$$k_{ET} = \frac{1}{\tau_D}\left(\frac{R_0}{d}\right)^6 , \tag{2.3}$$

where k_{ET} is the energy transfer rate, τ_D is the lifetime of the donor in the absence of an acceptor, d is the separation between donor and acceptor, and R_0 is the Förster radius which is defined to be distance at which the transfer efficiency is 50% which is expressed by [23]

$$R_0 = 0.02108\left(\frac{\kappa^2\Phi_D}{n^4}J(\lambda)\right)^{\frac{1}{6}} . \tag{2.4}$$

Here κ is the orientation factor, n is the refractive index of the environment, Φ_D is the donor quantum yield, and J is the spectral overlap integral between the donor emission and acceptor emission spectra:

$$J(\lambda) = \int F_D(\lambda)\varepsilon_A(\lambda)\lambda^4 d\lambda\, , \tag{2.5}$$

with $F_D(\lambda)$ being the normalized emission of the donor, and $\varepsilon_A(\lambda)$ is the extinction coefficient of the acceptor. For ease in the calculations, particularly in solution based samples, it is often assumed that $\kappa^2 = \frac{2}{3}$ for dipoles oriented randomly [24].

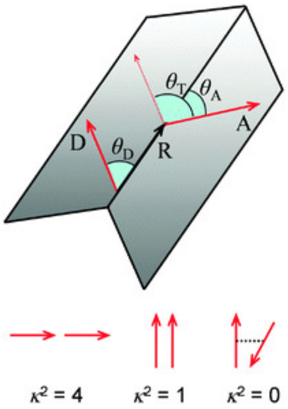

Figure 2.2: Relative transition dipole orientation between an acceptor and donor. R is the vector between the centre of the two dipoles with θ_D and θ_A being the angles between this vector and the donor and acceptor dipoles, respectively. θ_T is the angle between the two dipoles. Image taken from [25].

In general, the orientation factor describes the spatial orientation of the transition dipoles as given by

$$\kappa^2 = \left(\cos\theta_T - 3\cos\theta_D\cos\theta_A\right)^2, \tag{2.6}$$

where θ_T is the angle between the acceptor and donor dipole moments, θ_A and θ_D are the respective angles between the line joining the centres of the two dipoles with the acceptor and donor transition dipole moments. As shown in Fig. 2.2, the value of κ^2 can take a value from 0 to 4 depending on the relative dipole orientation. Hence for a system allowed to orient randomly, this value works out to be $2/3$. In the case where the energy transfer system is extended from a single acceptor case to a 2-dimensional array of acceptors (such as in film based systems), the concentration of the acceptors must be taken into account, which modifies Eq. 2.3 to [26, 27]

$$k_{ET} = \frac{\pi}{2}\frac{c_{acc}}{\tau_D}\frac{R_0^6}{d^4}, \tag{2.7}$$

where c_{acc} is the concentration of acceptors. Since the ET rate is an additional de-excitation decay pathway [28], it can be calculated directly using experimentally measured fluorescence lifetime values by

$$k_{ET} = \frac{1}{\tau_{DA}} - \frac{1}{\tau_D}\,, \tag{2.8}$$

with the subscripts DA and D indicating the donor-acceptor and donor only systems, respectively.

One can then define an energy transfer efficiency which takes the form

$$E_{FRET} = \frac{k_{ET}}{k_{ET} + k_{rad} + k_{nr}} = \frac{R_0^6}{R_0^6 + d^6}\,. \tag{2.9}$$

Due to the dependence of the donor emission and acceptor absorption profile, the value for R_0 will be unique for each acceptor-donor pair, and it has been determined for many dyes [29] and fluorescent protein [30] combinations. Given a value of R_0, it is then possible to calculate the theoretical FRET efficiency as a function of fluorophore separation. Experimentally, the modification of the steady-state PL or lifetime of the donor is used to measure the FRET efficiency and, hence, used as a proxy to determine the fluorophore separation by

$$E_{FRET} = 1 - \frac{I_{DA}}{I_D}\,, \tag{2.10a}$$

$$E_{FRET} = 1 - \frac{\tau_{DA}}{\tau_D}\,, \tag{2.10b}$$

where I is the PL intensity and the subscripts DA and D are as before. This technique has been used in biology/biochemistry fields as a "spectroscopic ruler" for example in monitoring the structural changes in certain biomolecules [31]. Often, the lifetime dependent efficiency (Eq. 2.10b) is used over the intensity dependency (Eq. 2.10a) due to the invariance of fluorescence lifetime to the fluorophore concentration below a reasonable concentration limit whereas the intensity does not share the same characteristic [32]. There have been recent works that has shown a concentration dependency on the lifetime of high QY dyes at concentrations of the order $10^{-6} - 10^{-5}$ M, however the authors attribute this effect to the interaction between the dye molecules and evanescent waves at the container boundary [33]. Thus, at significantly lower concentrations (10^{-9} M), it is expected to have insignificant effects on the fluorescence lifetimes, so the efficiency is exclusively calculated by the changes in lifetime.

2.2 Plasmonics

In this section, some basic interactions between light and matter will be introduced - specifically with noble metals such as gold. The free electron cloud present in metals are able to couple to external electric fields which causes the electrons to coherently oscillate, producing a Localised Surface Plasmon Resonance (LSP resonance, or LSPR). Two properties of LSPR, which has given it so much attention, is that it significantly enhances electric fields near the surface of the nanoparticle and has an absorption maximum at the plasmon resonance frequency. With nanoparticle diameters much smaller than the incident wavelength ($d \ll \lambda_0$, often $d < 100$ nm), spatial retardation effects may be ignored due to the negligible phase difference across the geometry of the particle - this is known as the quasi-static approximation. As such, one may evaluate the electric field distribution over these nanoparticles using electrostatics and add the time-dependence separately to observe the radiative, dipole-like emission [34, 35].

Fortunately, the simplest case is also the most relevant in that a spherical nanoparticle can be considered here. The sphere is assumed to be homogeneous and isotropic, of radius a and with a complex, frequency-dependent dielectric function $\varepsilon(\omega)$ in an environment with permittivity ε_d. Following the derivation provided by Jackson [36], the electric field potential inside and outside of the sphere is given by

$$\Phi_{in} = -\frac{3\varepsilon_d}{\varepsilon + 2\varepsilon_d} E_0 r \cos\theta \,, \tag{2.11a}$$

$$\Phi_{out} = -E_0 r \cos\theta + \frac{\mathbf{p}\cdot\mathbf{r}}{4\pi\varepsilon_0\varepsilon_d r^3} \,, \tag{2.11b}$$

where the frequency dependency is dropped for clarity ($\varepsilon(\omega) = \varepsilon$). It is also possible to see that Eq. 2.11b indicates the external potential is a superposition of the applied field with an internal dipole at the sphere's centre. Furthermore, let one define a dipole moment $\mathbf{p}$ as

$$\mathbf{p} = 4\pi\varepsilon_0\varepsilon_d a^3 \frac{\varepsilon - \varepsilon_d}{\varepsilon + 2\varepsilon_d} \mathbf{E}_0 \,, \tag{2.12}$$

in which a quantity known as the (complex) polarizability α is introduced as

$$\alpha = 4\pi a^3 \frac{\varepsilon - \varepsilon_d}{\varepsilon + 2\varepsilon_d} \,, \tag{2.13}$$

defined from Eq. 2.12 as $\mathbf{p} = \varepsilon_0\varepsilon_d\alpha\mathbf{E}_0$. One immediately recognizes that the polarizability becomes enhanced as $|\varepsilon + 2\varepsilon_d| \to 0$. If $Im[\varepsilon]$ is small (or slowly varying) around the resonance then this condition simplifies to $Re[\varepsilon(\omega)] = -2\varepsilon_d$; known as the Fröhlich condition.

From Eq. 2.11a and 2.11b the electric field distribution can be evaluated using $\mathbf{E} = -\nabla\Phi$ which yields

$$\mathbf{E}_{in} = \frac{3\varepsilon_d}{\varepsilon + 2\varepsilon_d} \mathbf{E}_0 \,, \tag{2.14a}$$

$$\mathbf{E}_{out} = \mathbf{E}_0 + \frac{3\mathbf{n}(\mathbf{n}\cdot\mathbf{p}) - \mathbf{p}}{4\pi\varepsilon_0\varepsilon_d} \frac{1}{r^3} \,, \tag{2.14b}$$

with $\mathbf{n}$ being the unit vector in the direction of some arbitrary point, P, outside of the nanoparticle. Therefore, upon meeting the Fröhlich condition, there is an enhancement of the internal and external electric fields around the nanoparticle giving rise to the sought after property of metallic nanoparticles - greatly enhanced electric fields.

Extending this scheme to allow for time-varying fields, consider now an external, oscillating electric field of the form $\mathbf{E}(\mathbf{r}, t) = \mathbf{E}_0 e^{-i\omega t}$ impinging on the spherical nanoparticle as a plane wave. This induces an oscillating dipole moment $\mathbf{p} = \varepsilon_0 \varepsilon_d \alpha \mathbf{E}_0 e^{-i\omega t}$ in the sphere leading to the scattering of the plane wave.

Finally, in this thesis, since the separation distance between the AuNP sphere and a fluorescent probe (dye or QD) is very close (much smaller than the diameter of the AuNP) such that the near field must be considered, it is useful to consider the total electric and magnetic fields. These are given by

$$\mathbf{H} = \frac{ck^2}{4\pi}(\mathbf{n} \times \mathbf{p})\frac{e^{ikr}}{r}\left(1 - \frac{1}{ikr}\right), \tag{2.15a}$$

$$\mathbf{E} = \frac{1}{4\pi\varepsilon_0\varepsilon_d}\left[k^2(\mathbf{n} \times \mathbf{p}) \times \mathbf{n}\frac{e^{ikr}}{r} + [3\mathbf{n}(\mathbf{n} \cdot \mathbf{p}) - \mathbf{p}]\left(\frac{1}{r^3} - \frac{ik}{r^2}\right)\right]. \tag{2.15b}$$

Here $k = 2\pi/\lambda$ is the wavenumber of the electric field. Considering the near field ($kr \ll 1$), one recovers the electrostatic expression given in Eq. 2.14b.

2.2.1 Absorption, Scattering, Extinction

A few useful and experimentally measurable properties of plasmonic nanoparticles are the absorption, scattering, and extinction cross-sections. In general, the absorption cross-section can be described as the ratio of the total power absorbed by the particle with the power per unit area of the incident field. Similarly, the scattering cross-section can be described as the ratio of the total power of scattered light to the incident plane wave power per unit area. In the special case of spherical nanoparticles, the absorption and scattering cross sections are given by

$$C_{abs} = \frac{8\pi}{3} k^4 a^6 \left| \frac{\varepsilon - \varepsilon_d}{\varepsilon + 2\varepsilon_d} \right|^2 , \tag{2.16a}$$

$$C_{sca} = 4\pi k \alpha^3 Im \left[\frac{\varepsilon - \varepsilon_d}{\varepsilon + 2\varepsilon_d} \right] . \tag{2.16b}$$

Here, both equations imply that a resonance in the polarizability further leads to a resonant enhancement in both absorption and scattering of the particle. In the quasi-static limit, the extinction is simply the summation of the two quantities $C_{ext} = C_{abs} + C_{sca}$, and hence it will also be resonant under the above condition.

2.2.2 Plasmon coupled fluorescence

It was shown by Purcell in 1946 that the spontaneous emission of an atom or molecule is dependent on its local environment due to the change in the local density of optical states [37, 38]. This has been verified for a number of fluorescent probes placed near different geometries of metal structures [39–42]. However, the change in the fluorescence rate does not appear to be consistent in the literature. In one study by Shimizu *et al.*, it was shown that CdSe/ZnS QDs placed on smooth gold films exhibited significant quenching of the PL whereas the fluorescence intensity increased as the roughness of the film increased [43]. Additionally, a study by Cade *et al.* found a 6-fold enhancement in the fluorescence intensity of a layer of CdSe/ZnS QDs close to a Au nanotip [44], and is supported by similar experiments from Huang and Richards, demonstrating a 4-fold enhancement in similar QD fluorescence intensities by a blunt Au nanotip [45]. However, Dulkeith *et al.* was able to demonstrate that dyes near AuNPs are quenched due to the reduction in the radiative decay rate whilst also showing the non-radiative decay rate is virtually unaffected. It has been pointed out by Anger *et al.* that this discrepancy in the literature arises from the fluorescent process being a product of two processes [46]. The first being the excitation, which is influenced by the local environment, and the second being the competition between radiative and non-radiative decay, as briefly discussed in the previous section. These two processes can be treated independently as there is no coherence between them. The change in fluorescence for a source near a metal nanoparticle is expressed by [47]

$$\frac{k_{em}}{k_{em}^0} = \frac{k_{exc}}{k_{exc}^0}\frac{\Phi}{\Phi^0}\,, \tag{2.17}$$

where k_{em} and k_{exc} are the fluorescence rate and the excitation rate, respectively. The superscipt 0 denotes the corresponding intrinsic quantities (i.e., not in the presence of a metal). Furthermore, $k_{exc} \propto |\mathbf{p}\cdot\mathbf{E}|^2$ where $\mathbf{p}$ is the transition dipole moment of a fluorescent particle and $\mathbf{E}$ is the local electric field. In the presence of an optical antenna such as a metal nanoparticle, an extra decay pathway is introduced, which is denoted as k_{sp} and is the de-excitation rate due to the coupling with Surface Plasmons (SP), such that the QY becomes

$$\Phi = \frac{k_r}{k_r + k_{nr} + k_{sp}}\,. \tag{2.18}$$

Then, combining Eq. 2.18 with the intrinsic QY given by 2.1 gives

$$\Phi = \frac{k_r/k_r^0}{k_r/k_r^0 + k_{sp}/k_r^0 + (1-\Phi^0)/\Phi^0}\,. \tag{2.19}$$

The new k_r is the radiative decay rate of the fluorescent probe near the metal nanoparticle. As per above, the assumption that the nonradiative rate is unaffected implies $k_{nr} = k_{nr}^0$. The original decay rate is also recovered for large separations between the metal and molecule so that $k_{sp} \to 0$ and $k_r \to k_r^0$. Furthermore, if the fluorescent probe of interest has a Φ^0 close to unity (which is not uncommon for QDs), then it stands to reason that k_{nr} is negligible and one obtains $\Phi = k_r/(k_r+k_{sp})$.

The ratio between the spontaneous emission rate from a free QD (k_0) and one in the vicinity of a resonator ($k_{AuNP@QD}$) is quantified by a value known as the Purcell factor (F_P). This effectively translates to a ratio of the spontaneous lifetimes [48]

$$F_P = \frac{k_{AuNP@QD}}{k_0} = \frac{\tau_0}{\tau_{AuNP@QD}} , \tag{2.20}$$

with $\tau_{AuNP@QD}$ being the experimentally obtained fluorescence lifetime of the AuNP coupled QD sample. Usually, it is given as a result of the modification of the radiative rates due to microcavity effects influencing fluorescent probes [49]. The separation between the change in the radiative rate due to plasmonic coupling and the addition of the nonradiative transfer of energy to the plasmonic mode is particularly challenging, and therefore difficult to obtain the new radiative decay rate. However, it has been shown previously that this change can be deduced, rather elegantly by, [50, 51]

$$k_r = k_r^0 \frac{I(t = 0)}{I^0(t = 0)} . \tag{2.21}$$

Here, I refers to the count intensity (or number of photon events detected) of the fluorescence lifetime curve at some time, t, which, for $t = 0$ is the maximum of the lifetime decay curve, and the 0 superscript refers to the QD only case. Hence, given the PL QY and fluorescence lifetime of the probe, it is possible to calculate the change in radiative decay rate and, thus, the Purcell factor.

An alternative, but similar treatment to the plasmonically coupled fluorescence is to instead assume that the plasmonic particle does not affect the intrinsic decay rate of the plasmonically coupled fluorescent probe [52, 53]. This modification of the total decay rate from the decoupled case is captured by a separate decay pathway in addition to the intrinsic decay such that $k_{AuNP@QD} = k_r^0 + k_{nr}^0 + k_{sp}$. With this treatment, the Purcell factor given in Eq. 2.20 becomes

$$F_P = 1 + \frac{k_{sp}}{k_0}\,, \tag{2.22}$$

assuming the plasmon coupled de-excitation pathway is radiative. As the two methods are mathematical treatments of the same phenomenon, they are essentially equivalent descriptors.

2.3 Quantum Dots

Quantum Dots (QDs) are semiconducting particles typically of a few nanometers in size with distinct optical and electronic properties, in comparison to their bulk counterparts, which have been known since the 1980s [54]. When QDs are excited, they are promoted to a higher energy state by producing an energetically bound electron-hole pair, known as an exciton. Recent studies have shown exciting applications in Quantum computing using QDs [55], LEDs [56], lasers [57], heat energy harvesters [58], display technologies [59–62], to name a few. Furthermore, studies have also shown great advantages of using QDs over conventional fluorescent probes such as dyes. Such advantages include great thermal-, and photo-stability for adequately passivated QDs [63–65], as well as size dependent tuneable emission [66]. Additionally, QDs typically display longer fluorescence lifetimes (5-30 ns) than dyes (1-5 ns) enabling far simpler temporal discrimination of QD signals from scattering events. QDs have also been shown to exhibit high QYs, reaching as high as 60% and above for CdSe/ZnS QDs [67] including those used in this thesis. Coupled with their often greater extinction coefficients, QDs typically exhibit higher brightnesses over dyes. Hence, they are valuable as potential ideal fluorescent probes and display pixels (here the brightness is defined as the product between extinction coefficient and quantum yield).

Unfortunately, there are factors that hinder the widespread use of QDs such as composition, and blinking. Often, colloidal QDs are made using toxic materials such as Cd, Se, Pb, As, among others, which itself presents obvious health hazards in their use, with fabrication protocols that require dangerous environments ($>$200 °C) [68]. Although, there have been recent developments in tackling the hazards in the synthesis procedure of QDs notably in the temperatures required [69] and in using safer elements without the use of heavy metals, some even showing low level toxicity in cell studies using 800 nm emitting Si QDs [70]. Another unfavourable aspect of QDs is their irregular luminescence behaviour characterised by a series of stochastic "on"-"off" events known as blinking, limiting their use in single-molecule experiments such as in particle tracking [71]. This phenomena is believed to be caused by the photo-induced charging of the QD to a trap state causing a non-radiative Auger-recombination [72] and by the trapping of generated holes in recombination centres at defect sites [73]. Previous works have been shown to decrease the probability of blinking by employing surface modifications such as shells or surface ligands [74, 75] which may be explained briefly by the suppression of trap states by charges, although the exact nature of this phenomenon is still debated. Despite this limitation, excellent studies by Lidke *et al.* [76], and Chien *et al.* [77] demonstrated super-resolution imaging by exploiting blinking of QDs, reaching a spatial resolution down to 10 nm. The work conducted by Wang *et al.* introduced an algorithm that could reconstruct super-resolution 3 dimensional images of a distribution of QDs achieving similar spatial resolutions along the x-y plane and around 60 nm in the z direction [78].

2.3.1 Optical properties

As the size of QDs are small, it is possible to treat them as a 3D excitonic potential well [54] in which the electronic wave equation becomes spatially confined. When the QD size is comparable to the Bohr exciton radius of the material, the bulk semiconductor energy band structure becomes quantized with the band gap increasing with decreasing size of the QD as $1/R^2$ - this is the quantum confinement effect [79]. The Bohr radius for a bulk material is found by

$$a_B = \frac{\varepsilon \hbar^2}{\mu e^2}\,, \tag{2.23}$$

where ε is the semiconductor dielectric constant, e is the charge of an electron, and μ is the reduced mass of the exciton given by $\frac{1}{\mu} = \frac{1}{m_e} + \frac{1}{m_h}$ with effective electron (m_e) and hole (m_h) masses. For example, the Bohr radius of CdSe was previously found to be 5.3 nm [80], thus, one is able to comment on the confinement strength of the QD by comapring the physical radius to this Bohr radius. Although the diameter may be measured by microscopy (such as with *Transmission Electron Microscopy*), it may also be estimated provided information about certain physical parameters of the QDs such as the bulk material and QD band gap energy (E_g^{bulk} and E_g^{QD}, respectively), and dielectric constant. This relationship is illustrated by the Brus equation [81–83]

$$E_g^{QD} = E_g^{bulk} + E_{conf} + E_{Coulomb} = E_g^{bulk} + \frac{h^2}{8\mu R^2} + \frac{1.8e^2}{4\pi\varepsilon_0\varepsilon R} \tag{2.24}$$

where h is the Planck constant, ε_0 is the vacuum permittivity, and R is the QD radius. Additional to the confinement contribution (E_{conf}) to the band gap shift, there is also a significant contribution from the Coulombic interaction ($E_{Coulomb}$) between the electron and hole from the smaller spatial separation between the two particles. This model assumes the QD is spherical in shape with radius R, and is not always valid in all semiconducting materials, particularly for small sizes where the effective mass approximation breaks down. However, Eq. 2.24 still provides a useful tool for the calculation of size dependent energy shifts of the band gap and

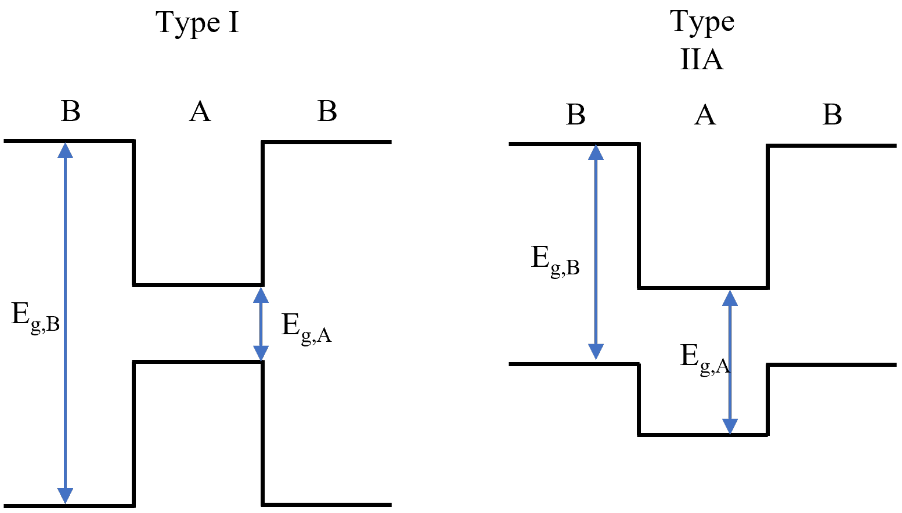

Figure 2.3: Simplified schematic of the two main types of core-shell energy gap offsets. In Type I, the core energy gap is smaller than the shell and hence the electron and hole pair is confined in the core. In Type IIA, the energy gap is shifted, thus the electron and hole is confined to different layers.

the understanding of the quantum confinement effects.

2.3.2 Core-shell types

As discussed above, certain factors limit the optical efficiency of QDs due to defect sites. One method to improve the QY of such QDs is to cap the core material with a shell that has an offset energy bandgap to the core. As such, there are different "types" of QDs depending on the offset level. The two main types discussed here are Type I and Type IIA, for which the energy gap offset is shown in Fig. 2.3. The aim of this band engineering is to spatially localise the excitons to different layers of the QD. As such, in Type I structures, an exciton generated is confined to the core. Whereas in Type IIA, the core conduction and valence band is lower (or higher in Type IIB) than in the shell and so the carriers are localised to different layers [84, 85]. For example, the QDs used in this thesis are CdSe/ZnS core/shell and are type I with a core bandgap of approximately 1.9 eV and shell gap of 3.8

eV. The sharpness of the interface (heterojunction) between the core and shell can affect the quality of the bandgap emission of the QDs. Although many factors can affect this including source purity, environment temperature *etc*, the main factor is the amount of crystal lattice mismatch [86]. Large mismatches between the core and shell crystals can lead to the creation of defects which may cause carrier trapping and thus, quenching of radiative emission [87].

Chapter 3

Materials and Methods

List of Chemicals

The following chemicals listed were used to synthesise the nanostructures. Cetyltrimethylammonium Bromide (CTAB), Cetyltrimethylammonium Chloride (CTAC), Gold(III) chloride ($HAuCl_4$), Sodium Borohydride ($NaBH_4$), and Ascorbic Acid, all purchased from Sigma-Aldrich. Other chemicals used include the polyelectrolytes (PE) Polydiallyldimethylammonium chloride (polyDADMAC), and Poly (styrenesulfonic acid sodium salt) (PSS) (nominal molecular weight of 32,000), both purchased from Sigma-Aldrich. For Electron Beam Lithography fabrication, the resist used was Poly(methyl methacrylate) (PMMA) 495K A4, purchased from EM Resist. The development of the PMMA mask involved Methyl-IsoButyl-Ketone (MIBK) in a 1:3 ratio with Isopropanol (IPA) and covered with espacer - the supplier of MIBK and espacer was EM Resist. For the nanostructures on quartz, the binding agents used were (3-Aminopropyl)triethoxysilane (APTES), and Silane-PEG-Biotin (M_w =1000) with Phosphate Buffered Saline (PBS - pH 7.4), purchased from Sigma-Aldrich. The Quantum Dots (QDs) used here were QDot™ 655 ITK™ Carboxyl, QDot™ 605 ITK™ Carboxyl, and QDot™ 585 ITK™ Carboxyl Quantum Dots purchased from Invitrogen™, Thermo Fisher Scientific. Unless otherwise stated, all aqueous solutions were made, and reactions performed in deionized water (18.2 MΩ·cm).

List of Equipment

Plasma treatment of substrates were conducted using a Diener Electronic FEMTO using ambient air as the process gas (unless otherwise stated). Sample centrifugation was done using an Eppendorf MiniSpin Plus for volumes less than 2 mL, a Beckman Coulter 64R Allegra benchtop centrifuge for volumes between 2 mL and 10 mL, and an Eppendorf Centrifuge 5804 for larger volumes. Spin coating was done with a Laurell WS-650MZ-23NPPB Spin Coater. A Stuart US152 hotplate was used for drying of substrate based samples. *Electron Beam Lithography* (EBL) was done using a Raith e-LINE system. The base dosages used were 150 μC cm^{-2} and 100 μC cm^{-1} for area and line writes, respectively. Metallic thin films and substrate-based metallic nanostructures were fabricated with Thermal Evaporation using an Angstrom® EvoVac Physical Vapor Deposition platform. *Scanning Electron Microscopy* (SEM) measurements were performed using a ZEISS-EVO® LS15 microscope (at 30 kV accerlating voltage and 30 μm aperture). *Atomic Force Microscopy* (AFM) images were obtained using a Bruker Dimension Icon operating on standard tapping mode in air. *Dynamic Light Scattering* (DLS) as well as *Zeta Potential* measurements were performed using a Malvern Zetasizer Nano ZS. A Shimadzu UV-2600 Spectrophotometer was used to perform *UV-Vis absorption* measurements and *Photoluminscence* (PL) measurements were done using an Aligent Cary Eclipse Fluorescence Spectrophotometer for samples in solution contained in a Hellma® Quartz Glass High Performance cuvette. For substrate based samples, a Piezoconcept BIO3 3-axis nanopositioner was used for scanning and fine sample spatial control, mounted on a Nikon ECLIPSE Ti2-U inverted microscope and equipped with a Nikon x60 magnification air objective (CFI Super Plan Fluor) with a numerical aperture (NA) of 0.7. Two PicoQuant LDH series laser diodes were used; one operating at 470 nm and another at 640 nm, each controlled by a PDL 800-D driver. The laser power (CW mode) was measured using a Thorlabs PM100D digital optical power meter, equipped with a S120C photodiode sensor at the microscope input port. At the input port, when operating the 470 nm laser, a 500 nm shortpass filter (FESH0500) was used for the excitation, and emission was filtered through a 500 nm longpass filter (FELH0500) with the two beams separated with a 50% transmission/reflection 490 nm dichroic mirror (DMLP490R), contained in a microscope filter cube. With the 640 nm laser, the corresponding optical elements were a 650 nm shortpass filter (FESH0650), 650 nm longpass filter (FELH0650), and 50% transmission/reflection 650 nm dichroic mirror (DMLP640R). The optical elements described in the microscope filter cubes were all purchased from Thorlabs. PL measurements were taken using an OceanInsight QE Pro FL spectrometer where fluorescence emission is collected into a M29L01 Thorlabs optical fibre (600 μm core size, 0.39 NA and 1 m in length), and intensity maps were obtained using a Thorlabs PMT2101/M Photomultiplier Tube (PMT). The data from the PMT is fed into a National Instruments USB-6003 Data Acquision Card (DAQ) for processing of the analogue signal before being sent to the PC. *Time Correlated Single Photon Counting* (TCSPC) measurements were performed with a PicoHarp 300 TCSPC timing module and a PDM series Single Photon Avalanche Diode (SPAD) detector. Bandpass filters positioned in front of the SPAD used in this work were FBH580-10, FBH610-10, and FBH650-10 which were purchased from Thorlabs.

3.1 Laboratory Setup

In this chapter, I will discuss not only the principles of the techniques used to characterise the samples but also the set up of the equipment necessary to perform the measurements. Although many of the individual measurements may be obtained using commercial grade equipment and software as outlined in the section "List of Equipment" above, it is often more useful using a customised set up allowing for more freedom in measurement techniques inlcuding various concurrent combinations, transparency in analysis, and "future-proofing" the equipment for potentially greater versatility. A basic schematic of the in-house optical line can be seen in Fig. 3.1 in which all but the microscope was developed from the ground up. Furthermore, software was written in Python 3.6 (and beyond) to create a graphical user interface (GUI). This enabled easier control of the scanner stage and synchronise the stage's movement with the data acquisition to perform raster scanning imaging as well as fine stage control for precise positioning of the laser spot over points of interest i.e. on top of gold nanoparticles.

3.2 Steady-State Spectroscopic measurements

The techniques used in this thesis to obtain the optical and physical characteristics of samples are described in this section.

3.2.1 Absorption spectroscopy

UVVis absorption spectroscopy was employed to measure the optical characteristics of samples in solution. This technique is often used to measure the concentration of

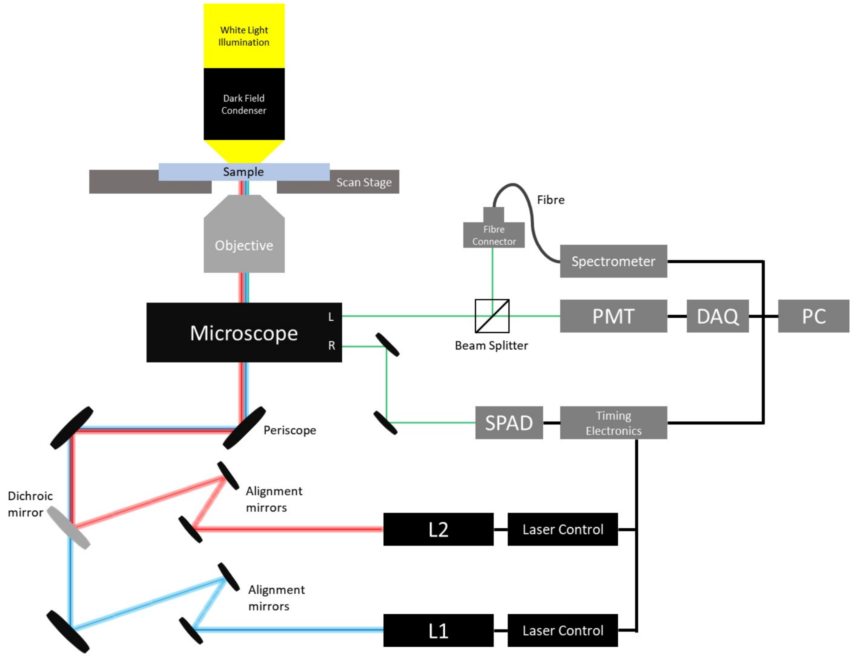

Figure 3.1: Basic schematic illustrating the optical set up. L1 and L2 are the two laser diodes operating at 470 nm and 640 nm, respectively. The microscope itself is able to output light at the left (L) and right (R) ports to the steady state detectors and time-dependent SPAD lines, respectively.

a sample given by the Beer - Lambert law

$$A(\lambda) = \varepsilon_\lambda CL, \tag{3.1}$$

where $A(\lambda)$ is the absorbance and ε_λ ($M^{-1}cm^{-1}$) is the sample extinction coefficient at wavelength λ, C (M or mol L^{-1}) is the concentration of sample, and L (cm) is the optical path length of the sample - the thickness of the film/cuvette cavity. It is also possible to extract ratios of concentrations for constituent species in a sample mixture by decomposing the observed spectrum into a weighted sum of the contributing component absorbances by a multiple linear regression model. The obtained weights for each constituent absorbance translate to the proportion of the corresponding species in the sample mixture.

3.2.2 Photoluminescence (PL) spectroscopy

Steady state PL spectroscopy offers an important tool in determining enhancement/quenching effects present in the system by monitoring the changes in emission intensity of the QDs. Often, one would look for and expect the enhancement (quenching) of the acceptor (donor), however for complicated systems that involve multiple donors and acceptors of different species, this might not necessarily be the case.

Importantly, combining PL and absorption spectroscopies allows one to measure the relative photoluminescence quantum yield (PLQY) of a sample by comparing its optical properties against a reference with a known PLQY. The unknown PLQY (Φ_i) of sample i (e.g., QD), is calculated against a reference dye with a known PLQY, by [88]

$$\Phi_{QD} = \Phi_{ref} \frac{I_{QD}}{I_{ref}} \frac{A_{ref}}{A_{QD}} \left(\frac{n_{QD}}{n_{ref}} \right)^2 , \tag{3.2a}$$

$$\Phi_{QD} = \Phi_{ref} \frac{m_{QD}}{m_{ref}} \left(\frac{n_{QD}}{n_{ref}} \right)^2 , \tag{3.2b}$$

where the subscript "ref" denotes the reference fluorescent dye (of known Φ), I is the integrated PL emission, A is the absorbance at the excitation wavelength, and n is the refractive index of the solvent containing the fluorescing substance. Given a series of dilutions of the reference and QD sample, it is possible to use the ratio of the gradients (m) instead of single PL and absorption values [89]. However, as pointed out by Demas and Crosby [90], Eq. 3.2a is only valid if the geometry and losses of the system are kept identical (i.e., reflection and scattering), the absorbances are kept low such that reabsorption and reemission effects are neglected, and the integrated PL intensity is assumed to be proportional to the absorbed light. Maintaining an identical geometry and optical losses is relatively easy by changing only the fluorescent probes, whilst using the same solvent and cuvette, which incidentally sets the refractive index ratio in Eq. 3.2a and Eq. 3.2b to unity. The assumption of proportionality between integrated PL and absorption can easily be verified by ensuring linearity in the measured gradients for the two samples. Alternatively, given a suitable detector, the method of determining PLQY can be further simplified to

$$\Phi_{QD} = \Phi_{ref} \left(\frac{D_{QD}}{D_{ref}} \right) \left(\frac{n_{QD}}{n_{ref}} \right)^2 , \tag{3.3}$$

where D_i is the detector response for sample i. Such a detector is a quantum counter in which the fluorescent probe has a near constant emission spectrum and PLQY over a relatively wide range and that the vast majority of excitation photons are absorbed over this range for suitable concentrations [91]. Historically, Rhodamine

B was used as the quantum counter material, due to it exhibiting a relatively constant fluorescence efficiency when excited between 350-600 nm, and a photomultiplier tube (PMT) to detect the emission photons. Therefore, the use of a quantum counter may be replaced by a single photon detector (e.g., a SPAD) particularly when the reference and unknown samples are evaluated at the same or similar emission wavelengths such that the detector sensitivity are approximately equal. With this method, the detector response, D, is effectively the photon counts per unit time. Alternatively, one may use a spectrometer and suitable collection optics, for example with a microscope objective. The detector response then becomes the integrated PL area with some geometrical corrections to account for the limited cone of light collected by the optics. Therefore, the effective sample PLQY can be found by measuring the difference in the integrated fluorescence intensity from a reference spectrum. This is particularly useful for changes in the fluorescence of QDs due to enhancement/quenching for point measurements on substrates. When measuring the PL of substrate based samples with a PMT or spectrometer, the CW laser power was kept low at 20 μW to minimise photo-bleaching of the fluorophores and avoid saturation of the spectrometer due to bright emissions of the QDs.

3.2.3 Dynamic Light Scattering (DLS) and Zeta Potential

Due to the distance sensitive nature of energy transfer, it is imperative to determine the sizes of nanoparticles in order to ascertain the separation between donors and acceptors and the minimal distances allowed. Furthermore, the surface charge (Zeta potential) is an important quantity that can help estimate the stability, and degree of electrostatic binding between different nanoparticle species. Both of these quantities can be easily obtained through DLS.

In brief, the working principle of DLS involves the scattering of light from a dilute nanoparticle dispersion to form a 2-D speckle pattern arising from constructive and destructive interference from this scattering. An autocorrelator at a detector then measures the intensity fluctuation with respect to time, which is related to the diffusion behaviour of the particles following Brownian motion [92]. Presuming the the nanoaparticles are monodisperse, an electric field correlation function is obtained by the autocorrelator which is an exponential function of the diffusion constant, D, for the nanoparticles. Therefore, D can be extracted from this correlation function and is subsequently related to the hydrodynamic radius, R_H, of the nanoparticle *via* the Stokes-Einstein relation [93, 94]. For a detailed theoretical treatment, I direct the reader to the useful guide provided by Stetefeld *et al.* [95]. Here, the R_H refers to a hypothetical sphere that diffuses at the same rate through the sample solution as the particle under investigation. It should be noted that the hydrodynamic radius of a particle includes the effect of surface modifications on the "core" particle and its effects on the surrounding medium; thus, DLS will almost always provide a larger value using an intensity distribution than a "dry" particle measured using SEM or similar techniques [96]. An additional, important parameter obtained from DLS is the Polydispersity Index (PDI) - a dimensionless quantity used to describe the uniformity of the size measured. A PDI of 0.0 indicates perfect homogeneity in the sample size distribution and in general a PDI < 0.1 usually indicates a monodisperse sample. Greater values of PDI typically implies that the sample is polydisperse with higher values indicating a greater degree of dispersity in the size distribution.

In Zeta potential measurements, the operating principle is somewhat similar to DLS except a potential is applied across a capillary cell containing the sample solution, with the charged particles migrating towards the oppositely charged electrode. Using a technique known as Laser Doppler Velocimetry (LDV), the rate of fluctuation of scattered light through the sample can be measured, which is proportional to the velocity (electrophoretic mobility) of particles in the sample. Finally, the Zeta potential can then be found using the Henry equation given by

$$\zeta = \frac{3U_E\eta}{2\varepsilon f(\kappa\alpha)}, \tag{3.4}$$

where ζ is the Zeta potential, U_E is the electrophoretic mobility, η is the solvent viscosity, ε is the solvent dielectric constant, and $f(\kappa\alpha)$ is Henry's function, usually approximated to be either 1.5 (Smoluchowski) or 1.0 (Huckel) [97]. The choice of either approximation is largely influenced by the relative size of the particle (given as α) to its Debye length (defined as κ^{-1} which is the distance a charged particle will affect the distribution of mobile ions in solution), and the ionic strength of the surrounding solution. In general, the Smoluchowski approximation is suitable for larger particles in high ionic strength solutions, and Huckel approximation is used for smaller particles in low ionic strength solutions. However, as only the *difference* between Zeta potential values between samples was important, the choice in Henry's function value is moot. As such, the Smoluchowski approximation was used throughout owing to the large size of the AuNP used. The samples were measured in displosable 1.5 mL polystyrene cuvettes (DLS) and DTS1070 folded capillary cells (Zeta) at 25 °C. Furthermore, samples measured here are diluted in deionized water such that their optical density (OD) is approximately 0.15 or less.

3.3 Time resolved spectroscopy

One of the gold standards of time resolved fluorescence spectroscopy, and a technique commonly used, is known as Time-Correlated Single Photon Counting (TCSPC). This is owed to the fact that TCSPC affords the user extremely high signal-to-noise ratios, independence of incident excitation intensity, and well-defined Poisson statistics to describe noise [98, 99]. As the name suggests, TCSPC works by detecting single photons emitted from a sample and measuring the time delay between an incoming laser pulse and the arrival of the detected photon. Therefore, this requires a pulsed excitation source capable of high repetition rates. This process is repeated millions of times to generate a histogram of photon arrival times, which can then be fitted with a multi-exponential decay function of the form

$$I(t) = I_0 \sum_{i}^{N} \alpha_i \cdot \exp\left(-\frac{t}{\tau_i}\right), \tag{3.5}$$

where α_i are the amplitude fractions for the i-th lifetime component, τ_i, for N components, and I_0 is the maximum of the decay curve. The sum of the amplitude fractions is also normalised such that $\sum_i^N \alpha_i = 1$. For this thesis, I consider $N \leq 2$ as this is sufficient to model real decay processes [100]. For multi-component decays, it is useful to consider an average lifetime, alongside the individual components, either as the intensity- or amplitude-average lifetime ($\langle\tau\rangle_I$ and $\langle\tau\rangle_A$, respectively) which can be expressed as

$$\langle\tau\rangle_I = \frac{\sum \alpha_i \tau_i^2}{\sum \alpha_i \tau_i}, \tag{3.6}$$

$$\langle\tau\rangle_A = \frac{\sum \alpha_i \tau_i}{\sum \alpha_i}. \tag{3.7}$$

As the sum of amplitudes are normalised, the denominator in Eq. 3.7 can be ignored. As discussed by Sillen and Engelborghs [101], the use of either average lifetimes is not always well defined in the literature and so following the logic presented by the authors, the amplitude-average lifetime will be used in this thesis. Furthermore, it is important to keep in mind that the detectors used are not be able to process an arbitrarily high number of photon events during some time period. After registration of a photon event, there is some time in which the SPAD is not able to process another event due to the recharge of the system - this is known as Dead Time (DT) [102].

If the laser intensity is set too high, it becomes more probable that each laser pulse will generate more than one photon. Under this scheme, the photon that arrives first will be recorded but the later photons will be lost if they arrive within the DT of the SPAD. This results in artefacts which skews the data towards the fast decay portion of the histogram due to the over-representation of earlier photons [103]. This artefact is called "pile-up" and can be seen in Fig. 3.2 where increasing the laser repetition rate above 1% generally causes the obtained histogram to bias fast decay processes. Therefore, in order to mitigate such an artefact, the laser intensity is modulated (either by controlling from a laser driver or with neutral density filters) such that the detection rate at the SPAD is kept to, at most 1% of the repetition rate of the laser to ensure only one fluorescence photon emitted by the sample is generated per pulse. For example, if the laser repetition rate is set to 5 MHz, the detection rate as recorded by the SPAD should ideally not exceed 50 kHz, however this is only a general guide. In this thesis, the laser intensity was modulated by directly using the laser driver to vary the output power in order to achieve the desired photon detection rate.

Finally, as the samples to be investigated involve multiple fluorescent particles of differing emission wavelengths, bandpass filters were used to discriminate the signals to avoid (or at least mitigate) the effects of spectral "bleed through" or crosstalk. These filters are outlined in the "List of Equipment" section above.

3.3.1 Lifetime Fitting

3.3.1.1 Iterative Reconvolution

A well known downside of TCSPC limiting the temporal resolution is the Instrument Response Function (IRF) and the non-triviality in separating the observed decay from this IRF. The cause of the IRF is due, mostly, to the finite width of the excitation pulse as well as temporal broadening introduced by the digital components

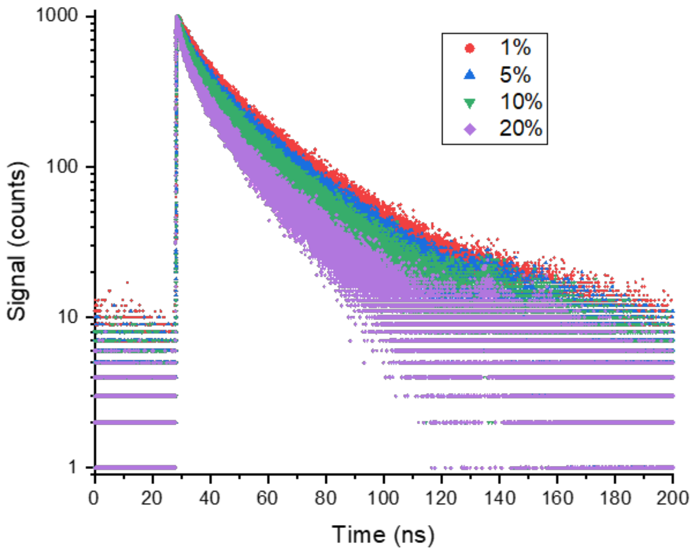

Figure 3.2: Typical lifetime decay curves of CdSe/ZnS QDs. The percentage refers to the detection rates at the SPAD relative to the laser repetition rate (5 MHz).

in the system [104] - see Fig. 3.3. Unfortunately, this presents itself as a convolution between the IRF signal and the "true" fluorescence decay ($F(t)$), producing the observed decay ($D(t)$)

$$D(t) = \int_0^t F(t')IRF(t - t')dt'. \tag{3.8}$$

Direct methods of deconvolution for fluorescence lifetime decay data has been previously shown to fail due to the ill-posed nature of the mathematics (particularly with truncation or incomplete decay curves within the measurement window) and sensitivity to noise [105]. Instead, what is typically performed is a method known as Iterative Reconvolution in which the true fluorescence decay is estimated and convolved with the measured IRF. The result is then compared against the observed data by a non-linear least squares minimization method and the fitting parameters (α_i and τ_i) are iterated until a solution converges. The reconvolution analysis

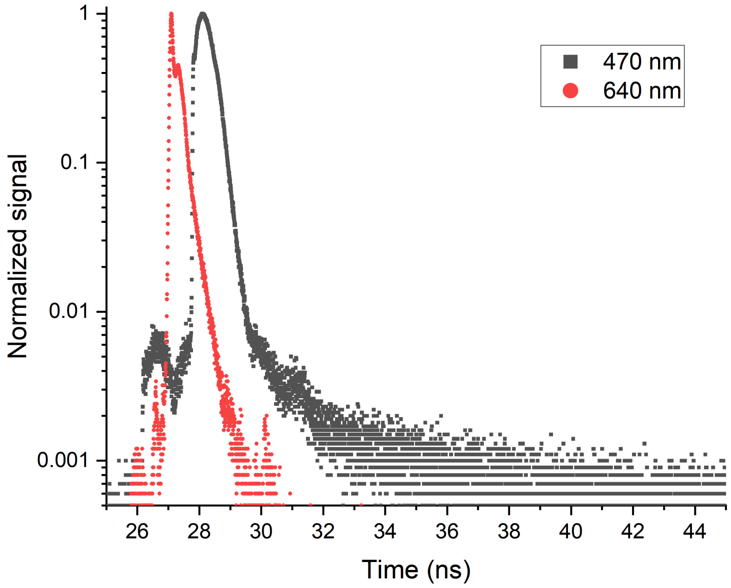

Figure 3.3: Instrument Response Function (IRF) of the optical system used for two different operating wavelengths. The FWHM is approximately 110 ps and 630 ps for 640 nm and 470 nm, respectively.

of sample lifetime data in this thesis was performed using an own code written in Python 3.

3.3.1.2 Tail Fitting

Often, the method of iterative reconvolution is cumbersome and computationally expensive, particularly for large data sets e.g. in Fluorescence Lifetime Imaging Microscopy (FLIM). A far quicker method of extracting lifetimes is to exclude the temporal region of the data set where the IRF has a significant intensity. This removes any influence on the data due to the excitation pulse or electronics. As shown in Fig. 3.3, both pulses start at approximately 26 ns with a temporal width of 8 ns and 4 ns for the 470 nm and 640 nm laser diodes, respectively. Although the fitting is less taxing after these time windows from the initial rise, one must sacrifice the initial part of the data set which is problematic for processes that have fast decay times that are comparable to the IRF width. Therefore, this technique is only suitable for species that are known, or expected, to exhibit long decay processes compared to the IRF width.

3.3.2 Scan imaging

Although TCSPC alone is incredibly powerful, the usefulness can be further increased by combining it with spatial information for fixed samples - commonly known as Fluorescence Lifetime Imaging Microscopy (FLIM). In its simplest state, FLIM involves the use of 2D spatial scanning (e.g., raster scanning as shown in Fig. 3.4) where each pixel contains the full lifetime decay curve, akin to hyperspectral imaging (HSI) in which every pixel contains spectral information about the sample. FLIM is most commonly used in biological fields of study and has recently been applied as pH sensors using tagged QDs in cells [106, 107], glucose sensors [108], and (rather appropriately) in FLIM-FRET systems [109, 110].

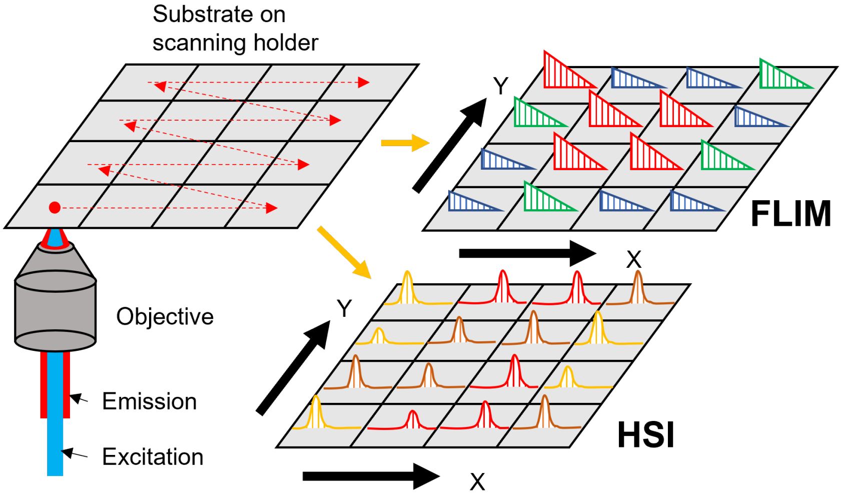

Figure 3.4: Two dimensional raster scanning across a substrate area that can provide either lifetime curves (FLIM) or hyperspectral imaging data (HSI) in each pixel.

Analysis of FLIM information is usually computationally challenging, for example performing iterative reconvolution (as discussed above) for every pixel in a large image often takes a long time to complete. Although there are many types of fitting and analysis techniques, each presents their own advantages and disadvantages [111]. In an ideal scenario, each decay curve will have a high photon count to increase the accuracy of the fitting, since the signal-to-noise ratio, SNR, is related to the photon events detected, N, as

$$SNR = \sqrt{N}\,. \tag{3.9}$$

However, in reality N is often quite low to minimise the time required to scan across an area with a high pixel count and so limits the accuracy of many fitting procedures. A simple first solution to overcome this issue of a "photon deficit" is to bin groups of spatially relevant pixels together to sum their photon events, thereby increasing N. To do so would require one to know, *a priori*, which pixels are relevant i.e. are related to Au-QD coupling and which are background. To increase one's confidence in which pixels to be considered, multiple types of images should be taken together (either simultaneously if possible or at least temporally close to each other) such as dark-field scattering and fluorescence intensity images. By correlating features across the images - such as hot spots - the pixels in the relevant regions of interests can be selected for binning.

3.4 Synthesis of Gold Nanoparticles

The fabrication of gold nanoparticles (AuNPs) were performed following a previously established protocol using a seed-mediated growth procedure [112]. This method relies on the overgrowth of small AuNPs from precursor seeds into larger polyhedrons and their subsequent, mild oxidation, to form the AuNPs with the desired dimensions and morphology (in this case, nanospheres).

Firstly, a mixture of 9.75 mL CTAB (0.1 M) and 0.25 mL $HAuCl_4$ (10 mM) was stirred together vigorously at room temperature while an ice-cold solution of 0.60 mL $NaBH_4$ (10 mM) was rapidly injected into the mixture. The vigorous stirring of the solution was allowed to continue for approximately 1 minute before reducing to a gentle stir for 2 hours. Afterwards, this "Seed-1" solution can be stored at room temperature.

Secondly, a growth solution was mixed together containing 19.5 mL CTAB (0.1 M), 380 mL H_2O, 8 mL $HAuCl_4$ (10 mM), and 30 mL Ascorbic Acid (0.1 M). To this growth solution, 0.24 mL of the previously made Seed-1 was added and the reaction mixure was gently swirled for approximately 1 minute to fully disperse the liquid. The mixture was left undisturbed overnight at room temperature and in the dark. Afterwards, this was centrifuged twice at 5000 rpm for 20 minutes, with the supernatant discarded and the pellet redispersed into 400 mL H_2O. This solution shall be referred to as "Seed-2".

To fabricate larger nanospheres, the prior Seed-2 solution must be further overgrown into nanopolyhedrons (AuNPH) before undergoing mild oxidation to obtain nanospheres with the desired diameter. This is achieved by adding a 1.6 mL of Seed-2 into a second growth solution consisting of 30 mL CTAC (25 mM), 1.5 mL $HAuCl_4$ (10 mM), and 0.75 mL Ascorbic Acid (0.1 M). The mixture is kept under gentle stirring for 3 hours at 45°C followed by centrifugation at 9000 rpm for 15 mins where the resulting pellet is dispersed in 15 mL H_2O.

Finally, the obtained AuNPH solution from above is gently stirred for 2 hours at 45°C with 0.2 mL $HAuCl_4$ (10 mM) added in order to oxidise the AuNPH to the desired spherical geometry. The volume of Seed-2 to the second growth solution may be varied depending on the desired diameter whereby adding a higher volume of Seed-2 will result in smaller AuNPs. The final AuNPs are stored at room temperature in the dark until required and have been seen to exhibit excellent physical stability, as will be discussed below.

The thickness of the CTAB surfactant bilayer has been shown previously to be 3.2 nm in Gold Nanorod suspensions [113] and will be assumed to be the case for the colloidal AuNPs in this study.

3.4.1 Characterisation of Nanoparticles

3.4.1.1 Optical

The AuNPs fabricated using the seed-mediated growth capped with CTAB displayed excellent stability when kept in storage under ambient conditions. This is shown in Fig. 3.5a with only a minimal blue shift in the LSPR peak (of only a few nanometers) between the dates measured while the overall spectral shape is maintained despite having been left for nearly 2 years under ambient conditions. The stability is attributed to the tight packing and strong binding of CTAB molecules on the Au surface making it difficult and energetically unfavourable for CTAB to dissociate

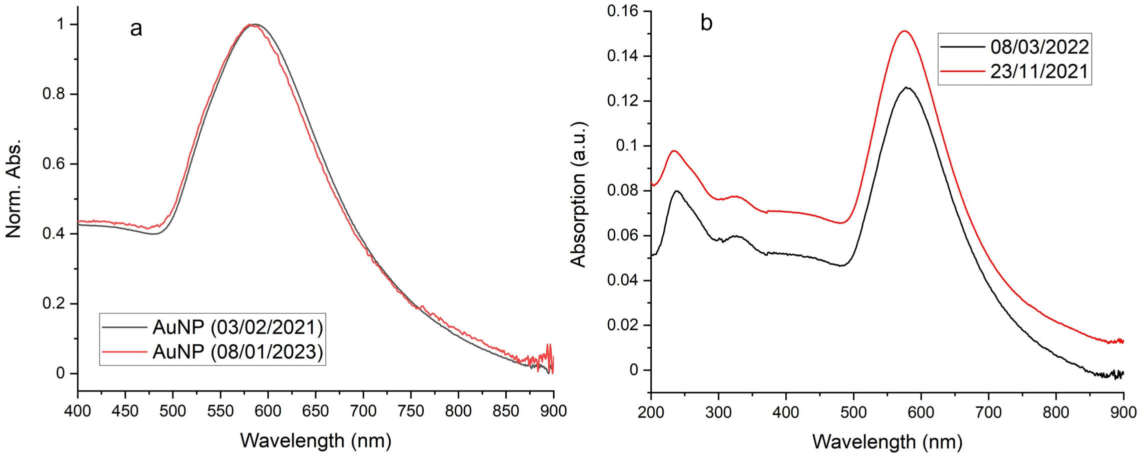

Figure 3.5: (a) Normalized UV-Vis absorption spectra of the same AuNPs batch in solution. The dates in the legend indicate when the batch was measured with the black curve being the day of fabrication. (b) UV-Vis absorption spectra of two different AuNP batches fabricated on the dates indicated on the legend. Note the absorption below 0 error for the black curve at approximately 850 nm. This was likely due to incorrect background correction which would not affect the spectral position of the LSPR peak.

from the AuNP surfaces [114]. The relatively high surface charge from CTAB also forms a strong electrostatic repulsion (typically ∼30 mV) between particles thus preventing aggregation.

Not only are the AuNPs stable in an aqueous solution, but the method is also reliable in its reproducibility of AuNPs with similar optical properties. As seen in Fig. 3.5b, the spectra of the two batches are highly similar across the entire optical spectrum, most importantly at ∼590 nm at the LSPR peak both in terms of position and peak width.

3.4.1.2 Physical

The physical properties of the AuNPs were measured using SEM and DLS and analysed using ImageJ. It was found that the average area of particles was $5962.4 \pm 644.6\ nm^2$; hence, assuming the particles are spherical (with a circularity of 0.80 ± 0.07, this assumption is valid), the average diameter is found to be $87.0 \pm 4.7\ nm$. In contrast, the hydrodynamic diameter found by DLS is found to be $136.4 \pm 0.5\ nm$

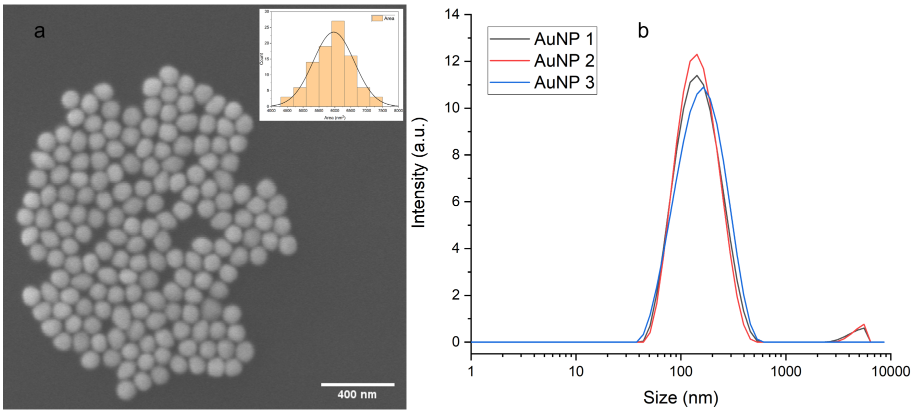

Figure 3.6: (a) SEM image of as-made AuNPs with an insert showing a histogram of particle area with an average diameter of 87.0 ± 4.7 nm. (b) Intensity-distributed DLS size graph of corresponding AuNPs. The diameter was found to be 136.4 ± 0.5 nm.

with a PDI of 0.20 ± 0.01. Although this is a significant discrepancy between the two measurements, it should be noted that intensity distributed size measurements from DLS tend to highlight larger particles in the sample due to their greater scattering. As noted by Souza et. al. in Ref. [115], it may be more appropriate to quote number distributed DLS sizes for small (relative to the incidence light wavelength), monodisperse samples due to its similarity to those obtained by electron microscopy techniques. Nevertheless, this is of little importance as the hydrodynamic radius is only an indicator of size and the change in this radius is the factor concerned.

Chapter 4

Multi-step Electron Beam Lithography

4.1 Introduction

First appearing as early as the 1960s [116], electron beam lithography (EBL) has remained one of the principal techniques utilized in the nanofabrication space owing to the sub-10 nm achievable resolution - some works attaining down to 5 nm [117]. It is a direct write approach in which a beam of highly energetic electrons are accelerated towards a resist to chemically alter its properties. The use of electrons also eliminates the diffraction problem faced by optical based techniques such as photolithography which often has a resolution limit on the order of 100 nm [118]. From the high resolution afforded by EBL, it is therefore excellent for the probing of spatially dependent light-matter interactions such as between fluorescent particles and plasmonic structures. Resists used in EBL are usually split into two categories: positive and negative tone resists. The positive tone group refers to the process in which the resist is, essentially, chemically etched and removed *via* a development step to leave behind a hole in which can be filled by deposition of a desired material such as metals or other chemical compounds to the substrate surface. Such resists include polymethyl methacrylate (PMMA), and ZEP520 [119–121]. Conversely, negative tone resists (also known as chemically amplified resists - CARs) are polymerized/cross-linked under e-beam irradiation and thus become more resistant to chemical etching during the development stage, ultimately leaving behind the patterned structure [122, 123].

Unfortunately, due to the top-down nature of EBL, it suffers from low throughput particularly for large and complex structures that span multiple write fields. As such, current EBL processes are unsuitable for scaling to larger/commercial grade production of nanodevices. Recently, efforts have been made to increase the throughput including the top-layer polymerization of negative tone resists by oxygen plasma treatment requiring only outline exposures to the e-beam to create arbitrary structures, thereby drastically reducing the write time needed [124]. It may be possible to extend this to positive resists such as PMMA from the similar reaction caused by low energy Ar ion bombardment [125].

Although the theoretical resolution is high due to the use of electrons, achieving feature sizes of 10 nm is rather difficult to attain in practice. Part of this reason is due to electron scattering in the PMMA or similar resists which significantly limits the practicably attainable resolution, rather than the characteristics of the beam itself. For positive tone resists, a high enough energy electron beam causes scissioning of the polymer chain under the electron beam's influence thus changing the solubility of the mask - known as main-chain scissions (MCS) [126, 127]. The scattering of electrons in the resists allows the effect of this MCS to permeate laterally away from the exposure point - this is called the proximity effect [128–130]. Works involving simulations have been performed to study this effect where the scattering is due to the forward scattering from the interaction with the resist, and back scattering from the substrate causing large angle deflections [131]. This is most evidently shown in

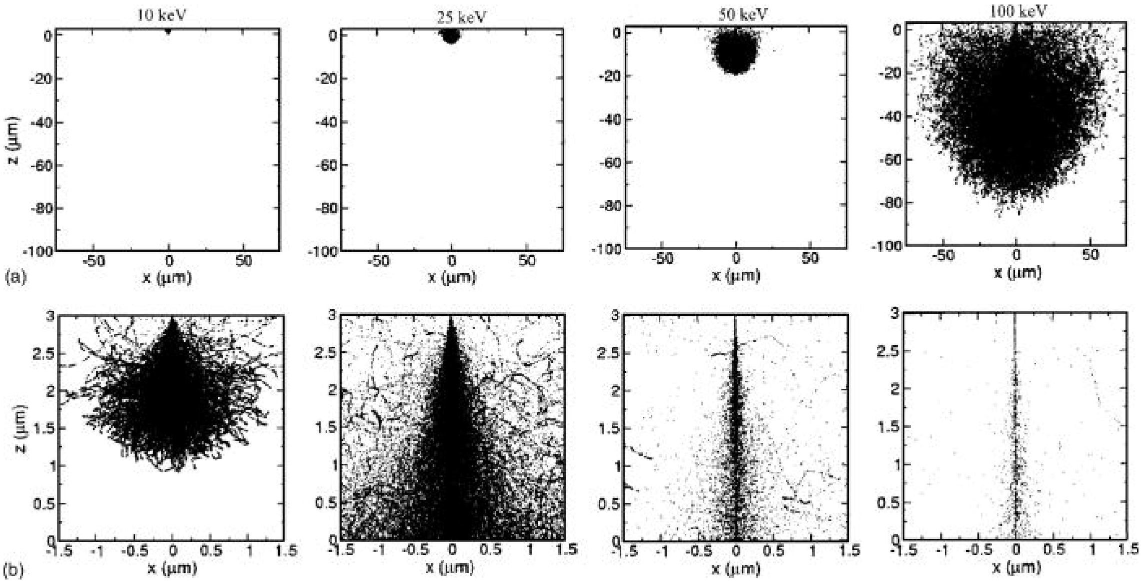

Figure 4.1: Simulated electron trajectories (a) in resist and substrate (b) within resist as a function of beam energy. Image taken from Ref. [132].

Fig. 4.1 where an increase in beam energy creates a narrower trajectory within the resist, however it also widens the scattering volume in the substrate, thus affecting a large area in the resist due to this back scattering.

The physical manifestation of this in resist can be seen in Fig. 4.2 where the pearl-shaped cavity in Fig. 4.2b is due to electron-resist scattering. Here, the sample used was a 5 μm thick PMMA layer exposed to a 20 keV electron beam of constant dosage at different points on the layer. The development time was increased from images (i) to (iv) indicating the volume surface represents contours of constant electron energy deposition in the resist. Therefore, the user must consider the resist thickness, type, incident beam dosage, and development times when fabricating nanostructures with minimal deformation due to this proximity effect from the substrate and nearby exposure sites.

Efforts to attempt to model and correct this effect that have been made include shape modification which involves maintaining the same dosage but varying the write path such that the developed image closely resembles the desired shape as compared

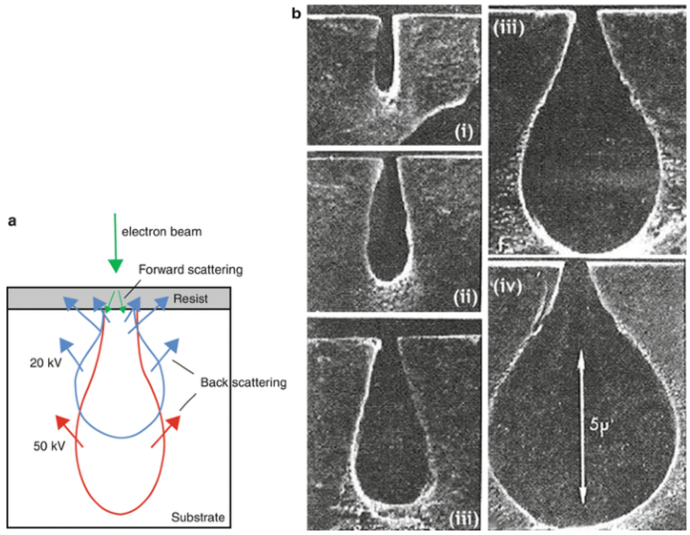

Figure 4.2: (a) Schematic of forward and back scattering volume into the resist and substrate. (b) Pearl-shaped cavity in a 5 μm thick PMMA layer produced by electron-resist scattering from an incident 20 keV electron beam at fixed dose, and increasing development time from (i) to (iv). Images taken from Ref. [135, 136].

to an uncorrected model to avoid overexposure from nearby beam sites [133]. Alternatively, the dosage (related to exposure time) is varied such that local proximity effects from nearby sites are accounted for and the correct dosage is achieved at the spot [134]. However, this is often computationally expensive especially for large circuits.

A relatively simple work around to this is to separate the structure such that geometries that are nearby (approximately 10 nm) are in different layers, where each layer represents an independent lithographic step that are aligned to some global feature. This idea was first conceptualised by Chen *et al.* in a two-step EBL process [137]. their work involved the fabrication of ultra-short T gate structures in PMMA/UNIII resists that would otherwise be extremely challenging or impossible to perform with a single step. Similarly, Koller *et al.* demonstrated the fabrication of 3 dimensional structures with a two-step EBL method using different acceleration voltages in each step for a single, SU-8 negative tone resist [138, 139]. Although in these cases, the two-steps are conducted on the same resist without development in between.

Instead of direct metallic deposition *via* sputtering or thermal evaporation, previous works have been shown to successfully transfer plasmonic materials onto substrate *via* stamping procedures in which a master was fabricated using EBL [140, 141]. The main motivation for these types of printing techniques is to increase scalability and reduce production costs of SERS based platforms that similarly rely on EBL. This is particularly true if EBL is only required once to fabricate a robust "master" template from which the SERS substrate is created from and is not sacrificed in the process like with traditional masks.

As the thesis is primarily interested in light-matter interactions between metallic nanoparticles and QDs, EBL provides an excellent platform for which the relative positions of the nanoparticles can be controlled. This enables one to accurately measure the separation distance between constituent nanoparticles, and therefore measure the energy transfer and plasmon-coupled decay rates of QDs as a function of this distance. Hence, in this chapter the method of performing multiple lithographic writes over fresh resists on a single substrate will be explored and the practicality of the method will be discussed. Printing based fabrication techniques that utilises EBL as well as advances made in the field of EBL as a whole will also be briefly discussed.

4.1.1 Surface Enhanced Raman Spectroscopy (SERS)

Raman spectrocopy (RS) is a vibrational spectroscopy method which provides users with particularly useful information about the composition of samples investigated due to the unique "chemical fingerprints" of Raman active molecules [142]. The interaction between light and molecules very often results in elastic scattering (if not absorption), meaning there is no change in incoming and outgoing photon wavelength - this is known as Rayleigh scattering. About 1 in 10^5 interactions between Raman active molecules and incident photons results in an inelastic scattering process, thus exchanging energy and manifesting as a change in the outgoing photon energy - this is Raman scattering [143]. The difference in energy between the incoming and outgoing photon is known as a Raman shift and is reported in terms of a wavenumber, $\Delta\nu$, as calculated by

$$\Delta\nu = \frac{1}{\lambda_0} - \frac{1}{\lambda}, \tag{4.1}$$

where λ_0 and λ are the wavelengths of the incident and scattered photons, respectively. The change in photon energy is due to the interaction of the incoming photon and the vibrational/rotational modes of the molecule in question, thus the specific chemical bonds and composition of the molecule will yield different spectral shifts providing a characteristic or "fingerprint" spectrum. As such, RS has seen wide applications in detection of atmospheric compounds and long distance remote monitoring for hazardous and even explosive chemicals [144, 145], as well as the analysis of paint pigments and authentication of historical paintings [146].

Since the signals from RS are extremely weak, methods employed to limit background signals include the use of red (typically 785 nm) or infrared lasers with long acquisition times to obtain a sufficient number of photons for adequate discrimination of peaks from the background while minimizing damage to the sample at higher lasing frequencies. Alternatively, plasmonics can provide a useful tool in enhancing the Raman signals by up to 8 orders of magnitude [147]. The mechanisms to explain this include the large electric field enhancement from plasmon induced field localisation around the nanoparticles and rough metallic surfaces. Additionally, plasmonics induces chemical enhancement which results from the charge transfer from the metal atoms to the Raman probe [148].

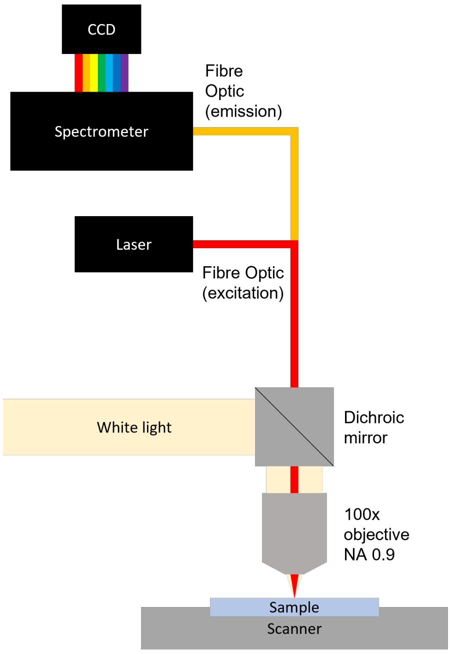

Figure 4.3: Schematic of the setup and optical path of the WITec alpha3000 R Raman microscope.

4.2 Methods

4.2.1 Equipment

Raman spectroscopy measurements were performed using an Oxford Instruments WITec alpha300 R confocal imaging microscope and the acquired Raman maps were analysed using WITec Project FOUR 4.1. The laser wavelengths used were 532 nm (WITec), and 785 nm (Toptica) with the power output controlled using a Topas iBeam smart app for the 785 nm laser. Raman signals were detected using a WITec UHTS 300 spectrometer. A schematic of the optical set-up is shown in Fig. 4.3.

4.2.2 Substrate preparation

To begin, the substrates used were quartz slides 15 x 15 x 1 mm and cleaned by sequential sonication in a bath of Acetone, Isopropanol (IPA), then water, for at least 1 minute in each solvent and dried under N_2 flow. The slides were then mounted onto the spin coater where Poly(methyl methacrylate) (PMMA) 495K A4 was applied to the quartz surface which was then spun at 3500 rpm (2000 rpm/s acceleration) for 60 s. Here, PMMA is used as the positive mask which, after the spin coating step, is baked on a hot plate set to 180°C for 3 minutes. Furthermore, EBL (and other electron based techniques including in microscopy) requires the substrate to be conductive to dissipate the charge build-up which causes bright artefacts, thus a few drops of e-spacer is added to the PMMA coated substrate and spun at 2000 rpm for 60 s before baking the substrate on a hot plate at 90°C for 1 minute. The quartz slide is now ready for EBL.

4.2.3 Mask Design and Development

The mask used in this study is illustrated in Fig. 4.4a where the two initial layers are represented by yellow for the first gold structure and blue for the second QD deposition. The dimensions of the arrays and Au bars are given in the figure and are fabricated with a thickness of 200 nm (not including the local and global marker Au pads). Furthermore, the QD holes are increased in diameter in steps of 20 nm starting with the left-most column at 20 nm and finishing at 120 nmm at the right-most column in the arrays highlighted in red and blue. The array highlighted in green has the same starting diameter and 20 nm step size but finishes at 140 nm for the right-most column. The periodicity of the holes is 2 μm in the red-highlighted array, and 1 μm in the blue array in both the vertical and horizontal directions. The cross-like features in the corners of the array in the figure serve as "local markers" to identify the boundaries of each array and is also be used as alignment markers. Larger versions of these crosses that span a significant portion of the write-field (i.e., are roughly 50 μm in width and proportionally larger than the local markers) are also used to mark the corners of a collection of such masks for example in a larger grid (Fig. 4.4b). The size of these large markers enable easier localization of the entire collection of hybrid structure arrays and aid in the alignment of subsequent steps and hence are referred to as "global markers". In order to enable subsequent layer alignment, the origin was set to a permanent feature of the substrate and all positions were set relative to this global origin point; thus the bottom left corner of the substrate was chosen and the mask arrays were positioned in the centre of the substrate accordingly. This allows one to re-centre the global origin back to the same corner when removing the substrate from the EBL in between each write and development and therefore overlay the subsequent layers accurately on top of the previous layers.

After electron beam irradiation, the substrate was removed from the EBL and submerged in a Methyl Isobutane Ketone (MIBK):Isopropanol (IPA) mixture (in a 1:3 ratio) for 45 s at room temperature to develop the mask and then into a pure IPA solution for 30 s, before drying under N_2 flow. This is to allow the dissolution of exposed PMMA to the solvent mixture while leaving the rest of the mask unaffected due to the MCS.

4.2.4 Substrate Nanostructure fabrication

After development of the PMMA mask, the substrate was placed in a FEMTO plasma asher, in this case using O_2 as the process gas, at 0.2 mBar, 40% power for a total of 12 s. This uniformly etches the PMMA across all surfaces at a reasonably low rate [149] and to activate the quartz surface to promote the formation of hydroxyl groups as well as increase the wettability [150]. The presence of hydroxyl groups

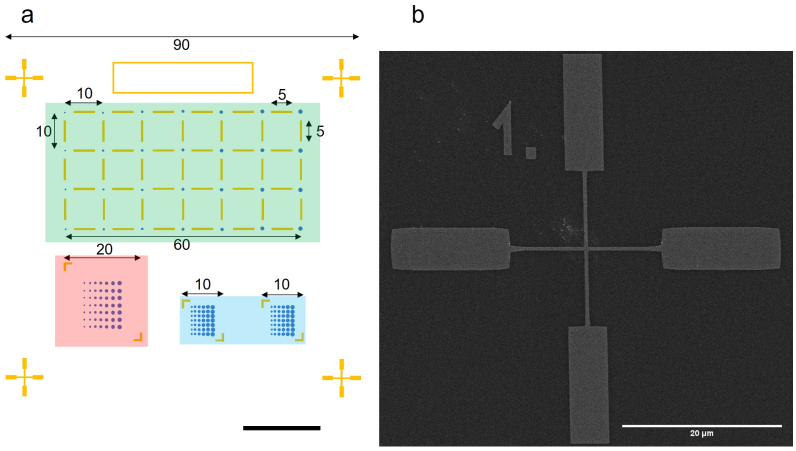

Figure 4.4: (a) Schematic of the mask design used in the AuNP-QD structure for a single write-field with dimensions given in μm. The first layer was gold and is represented by the yellow structures. The second QD layer is represented by the blue circles. Although not an identical scale match, the schematic represents closely the mask used in the study including the different sized holes in the second QD layer. The four corners of the array are bounded by local markers used to define the boundary of the write field and used in the alignment procedure between lithographic writes. The scale bar is 20 μm and the green/red/blue highlights are for visual reference only. (b) SEM image of a global marker - the four local array markers at the corner boundaries are omitted here. The total size of the write-field is 100 μm × 100 μm.

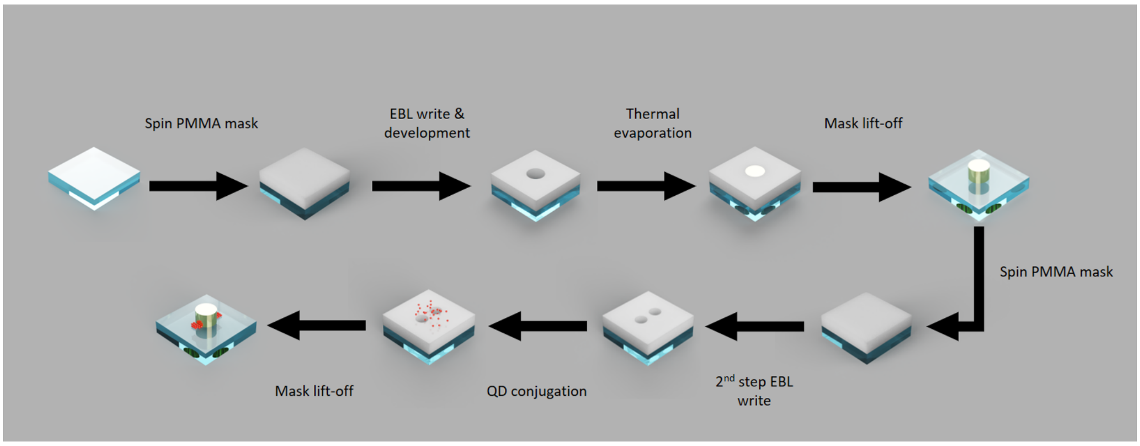

Figure 4.5: Flow diagram summarising a two-step EBL process. The bottom row may be repeated as many times as necessary for more complex structures for example with more QD types.

reacts with the silane group when the substrate is covered with APTES (2% in 95% Ethanol) forming a siloxane linkage (Si-O-Si) to create a self-assembled monolayer (SAM) [151]. After leaving for 30 s, the surface is washed with Ethanol and dried under N_2 flow.

This is then loaded into the thermal evaporator and 50 nm Au is deposited onto the SAM surface at a rate of 2 Å/s at a working pressure of $<10^{-6}$ Torr. Finally, the sample is left in an Acetone bath overnight to dissolve the PMMA and lift-off the excess Au film. Often-times the Au film remains on the surface due to incomplete dissolution of the PMMA film, in which case the sample will have been sonicated for no more than 5 s at a time to remove the excess PMMA and Au while minimising any damage potentially caused to the Au structure. The overall flow of the multistep EBL method is summarised graphically in Fig. 4.5.

4.2.5 Quantum Dot-Quartz attachment

The process of PMMA surface preparation, and lithographic write was repeated as before using the second layer design as illustrated by the blue circles in fig. 4.4. In multi-step lithography, the alignment between the gold array of the previous layer and the subsequent QD layer is critical particularly when small feature sizes are present between the layers. As discussed previously, this first involves the resetting of the global origin point back to the bottom left corner of the substrate. The coordinates used in the previous write are entered into the software to position this next QD layer on top of the gold array. However, this is typically not enough as there is often misalignment in the positioning of the physical substrate in the EBL sample holder. This misalignment is seen by driving to the coordinates of the previous write's local markers and these positions not properly superimposing onto the previously deposited gold local markers. To account for this, a "Three Point Alignment" process is performed: the stage is brought to a recognizable feature on a local marker (such as the centre of the cross - global markers may also be used), and the stage coordinates are saved. These coordinates are then correlated to the same reference point on the computer aided design (CAD) structure (e.g., centre of the local marker cross in software) - in other words the real coordinates of the gold structure are linked to the CAD software coordinates for the same reference point. This is performed for a total of 3 markers and is iteratively repeated by driving the stage to the reference points on the gold structures and adjusting the coordinates if necessary until all three reference points are adequately mapped to the CAD structure. The alignment of the markers is critical as errors introduced here will be compounded with subsequent layers, thus degrading the quality of the final array with multiple writes. As discussed by Yoon *et al.*, the two largest sources of error are the fabrication of alignment markers (i.e., their quality), and mechanical error from the stage [152]. The dimensions of the alignment markers may differ from those in the designed CAD model due to the proximity effect (as discussed previously), and thus introduces uncertainty in the alignment between fabricated and designed structures. The authors point out that simple cross geometries (such as the markers used in this thesis) are enough to minimise this proximity effect induced uncertainty if the dimensions of the intersecting bars are large enough such that the lengths are not affected by this effect. The original reference point is therefore at the intersection of the edges of the large nanobars. Secondly, the mechanical errors can be eliminated between the layer writes by aligning to the same structures for all subsequent layers. This is because the stage errors are typically constant along a direction for every layer and so aligning to the same reference point(s) eliminates the need for correction. The absolute position of a layer is not important - only their relative position. Accounting for these uncertainties, sub-20 nm alignment errors with high reproducibility are achieved by Yoon *et al.*

Immediately after the mask development and surface activation by Oxygen plasma, the surface was covered by a solution of Silane-PEG-Biotin (in ethanol) and left to react with the surface for 30 mins. This was followed by rinsing the substrate with plenty of Ethanol to remove excess Silane-PEG-Biotin and drying under N_2. Finally, enough PBS to entirely cover the surface was added and a drop of 655 nm Streptavidin conjugated QDs (QD-STV) was introduced into the PBS volume. This mixture on the substrate was left undisturbed for 30 mins before being rinsed off with of PBS. The removal of the PMMA layer was performed by submersion of the substrate upside-down in an Acetone bath overnight, held by a custom 3D printed mount made from a chemically resistant filament (e.g. PTFE aka Teflon). Finally, the substrate was removed from the bath and rinsed with copious amounts of water before being dried under N_2 flow.

4.3 Characterisation

4.3.1 Dose Testing

In order to obtain accurate structures using EBL, one must first perform dose testing of the electron beam for the system used (provided the astigmatism has previously been corrected and the beam current has been measured i.e. with a Faraday-cup). This is to ensure the development of the PMMA results in hole sizes, and subsequently the Au nanostructures, that closely resembles the desired morphologies with high reproducibility.

To achieve this, arrays of different fundamental shapes (typically lines, and disks) with varying electron dosages across multiple arrays were "written". After depositing a thin layer of Au, the arrays were then imaged using an SEM, and the resulting structures were compared against the desired dimensions on the computer aided design (CAD) software. The result of this dose testing can be seen in Fig. 4.6 where the dimensions of each structure was measured and the coverage of Au was evaluated

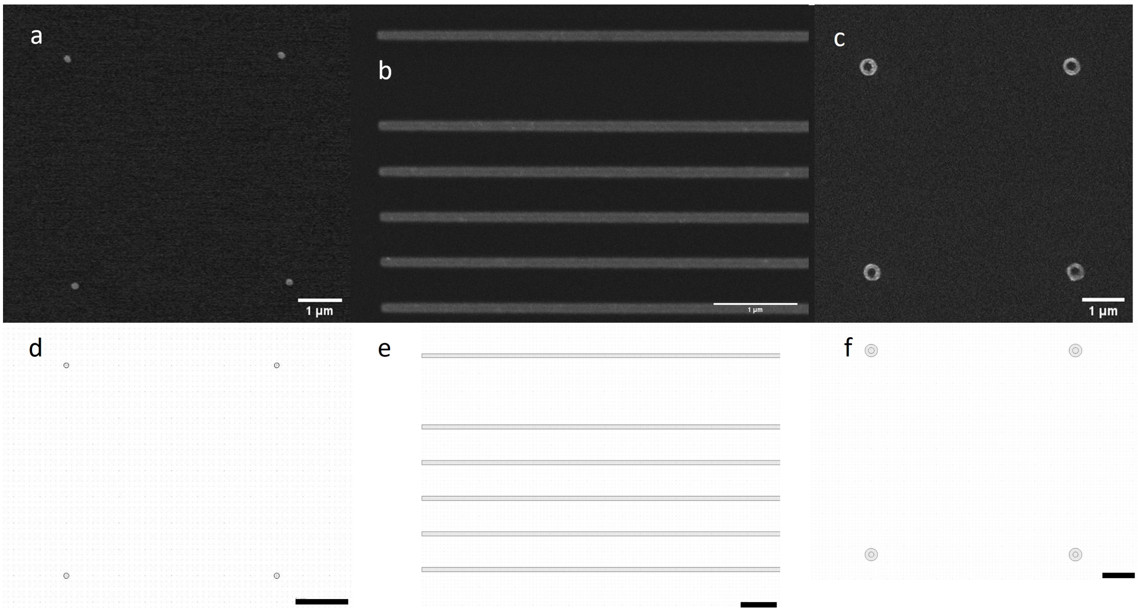

Figure 4.6: (a) Disks, (b) lines, and (c) rings produced from the E-Beam process for calibrating the required electron dosage along with their corresponding CAD images (d-f). The beam parameters are 20 keV accelerating voltage, and 10 μm aperture, with a line and area dose of 130 μC/cm and 150 μC/cm^2, respectively.

(i.e. homogeneity of the evaporated disks/lines/rings and number of successfully deposited structures in each array).

4.3.2 Substrate bound QDs

To determine the efficacy of the substrate binding, the quartz slides were imaged using an alpha300 R confocal Raman microscope. Under 532 nm CW laser illumination, a hyperspectral Raman map could be obtained within the array at the expected QD locations. These maps are shown in Fig. 4.7b and 4.7c where an example of the PL emission of the hot spots are given in Fig. 4.7. The intensity and colour of the heat map corresponds to the integrated area of the PL emission between 600 nm and 700 nm. Evidently, the hot spots correlate very well with the expected positions of the QDs in each of the scan areas, replicating the difference in spot spacing. Furthermore, the intensity of each of the hot spots corresponds to

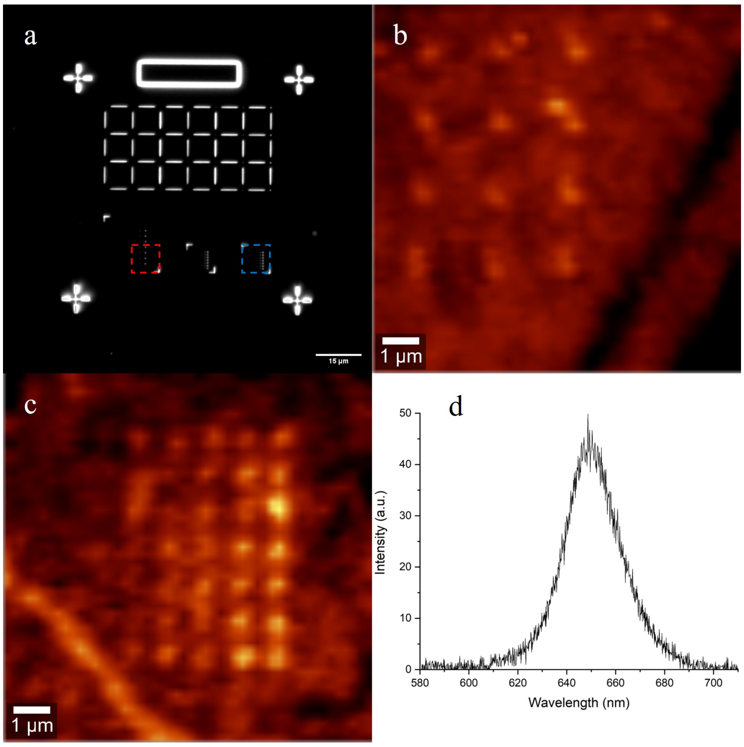

Figure 4.7: (a) Dark field image of the gold array fabricated by a two-step EBL procedure. Holes for QD deposition are located in the bottom three bounded areas and in the centres of the cross hair-like region in the upper portion of the write field with large holes seen on the right section. Confocal scanning PL maps of the areas bound by a (b) red and (c) blue box shown in (a). The intensity of the maps are determined by integrating under the curve between 600 nm and 700 nm of (c) the PL emission spectra of one of the hot spots in the (c) array. The periodicity of the holes are 2 μm and 1 μm for the red, and blue boxes, respectively.

the concentration of the QDs which is directly affected by the hole size generated by the e-beam. It can be seen that the intensity of the spots decreases from right to left in Fig. 4.7c - precisely as expected from the CAD with decreasing hole sizes in this direction. It can also be faintly seen in the dark field image in Fig. 4.7a where only the largest holes are visible in the red and blue boxes.

4.4 Stamped SERS substrate

As briefly mentioned in the introduction, previous works have involved the use of EBL to fabricate a reusable mask for stamping, also known as nanotransfer printing (nTP) or microcontact printing (μCP). In brief, the method can be summarized by fabricating the master template using the EBL workflow as described above using a Si substrate. A layer of Cr is then deposited *via* a Physical Vapor Deposition technique (such as thermal evaporation) and the mask removed to reveal a Cr template. The exposed Si is then etched by Reactive Ion Etching (RIE), and the Cr is removed leaving behind arrays of Si pillars in the shape of the desired pattern forming the base master template. This template can then be exposed to a releasing agent and coated with the patterning material such as Ag or Au - the releasing agent is used to allow the metals to easily transfer substrates such as heptadecafluoro-(1,1,2,2,tetrahydrodecyl)-trichlorosilane [141] or heptakis(6-O-tert-butyldimethylsilyl-2,3-di-O-acetyl)-β-cyclodextrin (H-β-CD) [140]. The sample substrate is then prepared, typically coating with a self-assembled monolayer (SAM) that is strongly reactive to the substrate. Finally, the template and substrate is brought in contact to each other to transfer the material, and the template peeled off leaving behind the desired structure on the sample substrate. The master template can then be reused by chemically etching the deposited metal on the Si surface. This process is summarized graphically in Fig. 4.8. Studies have shown great suc-

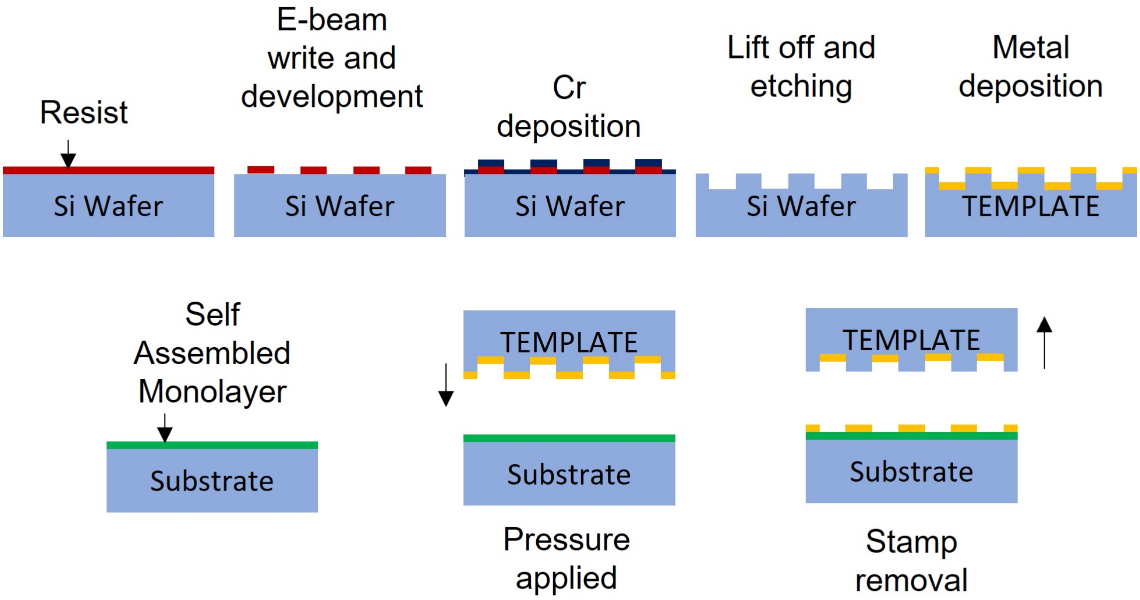

Figure 4.8: Schematic summarizing a typical nanotransfer printing process with traditional EBL and RIE of the Si wafer (top row from left to right) and nanometal transfer from the template to a functionalized substrate surface (bottom row from left to right).

cess using different types of linker molecules between substrate and transfer material for example with the use of complimentary DNA to funcationalized AuNPs for high specificity in potential biosensor applications [153]. For SERS substrates, the SAM must be Raman active (presents a change in polarizability of the molecule) or reactive to the material used e.g., are terminated with silanes for quartz substrates or amines and thiols for Au chemisorption. Examples of such molecules include mercaptobenzoic acid [154], benzenethiol [155], and cysteamine [156].

In this section, a SERS based substrate was studied in which an ordered array of 100 nm diameter AuNPs were assembled over a SAM of biphenyl-4-thiol (BPT). The samples were made by collaborators Lee *et al.* at the Korea Advanced Institute of Science and Technology, and Ludwig-Maximilians-Universität München from the published work found in [157]. This was fabricated using a template dissolution Capillary-assisted particle assembly (CAPA) method in which AuNPs in solution

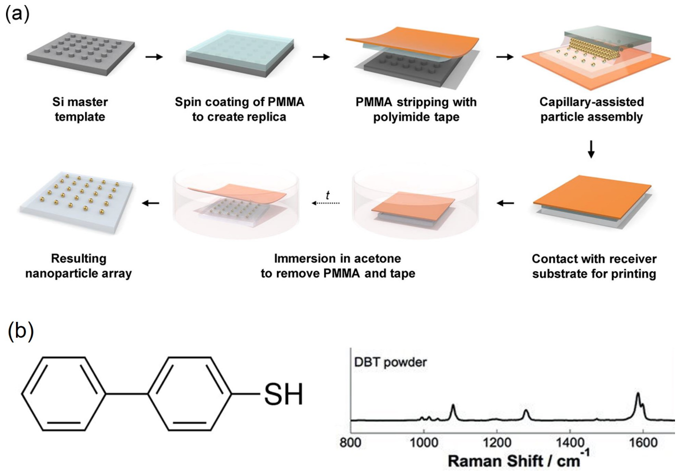

Figure 4.9: (a) Schematic summary of the CAPA protocol obtained from Ref. [157]. (b) Chemical structure of biphenyl-4-thiol along with an example Raman spectrum where the y-axis represents the signal intensity in arbitrary units obtained from Ref. [158].

are forced into recessed sections of a PMMA mask by capillary forces. These forces are generated at the meniscus formed at the edge of a glass coverslip that was pulled across a PMMA template when this solution was trapped between the two surfaces. The recesses are made by spin coating PMMA over a Si master and peeling this away with polyimide tape. As described above, the PMMA template is then stamped onto a BPT covered glass substrate and the PMMA dissolved with acetone, leaving behind the ordered AuNP arrays. This process is shown graphically in Fig. 4.9a with an example Raman spectrum of BPT (Fig. 4.9b). Using a 785 nm laser, the AuNP arrays were scanned across and a spectrum was obtained for each pixel. To represent the spatial variation, the Raman spectra were integrated between 800 cm^{-1} and 1800 cm^{-1} for each pixel. This integrated Raman map can be seen in Fig. 4.10b. The bright field (BF) image shown in Fig. 4.10a clearly indicates the ordered pattern of the AuNPs on the glass substrate and correlates with the position (and orientation) of the Raman map. It is worth noting that there is a spatial shift between the BF and Raman map, likely due to inaccuracies in the scanning stage positioning. Furthermore, the authors note that the assembly process

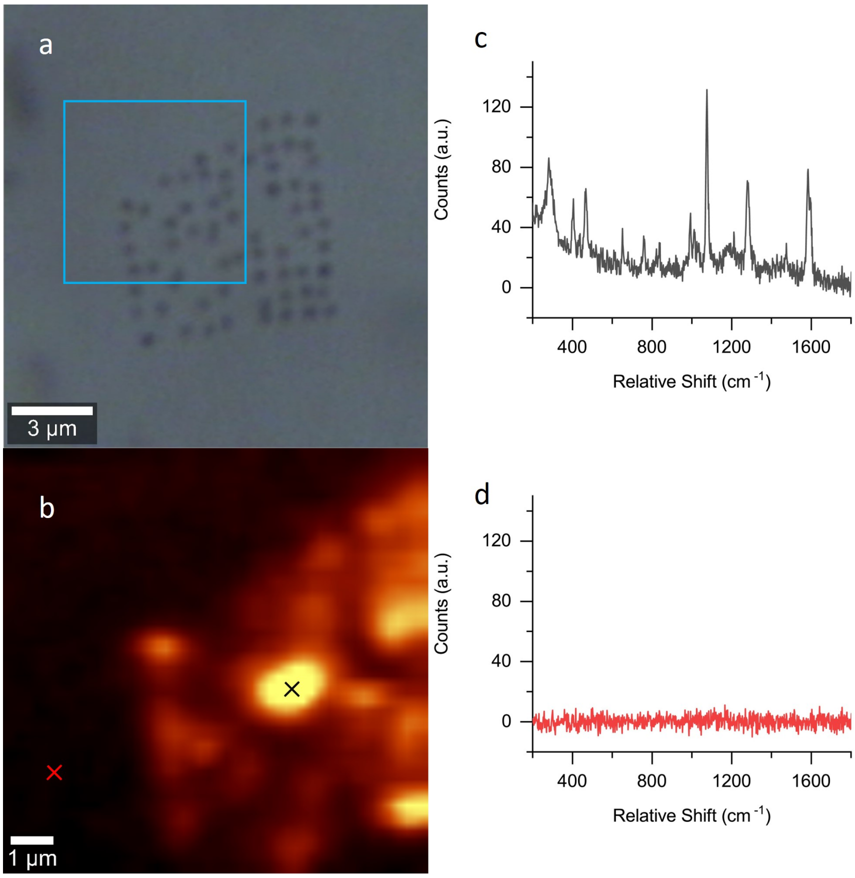

Figure 4.10: Printed AuNP arrays using the CAPA method showing the (a) bright-field image, (b) Raman map integrated between 800-1800 cm^{-1} where the scanned area corresponds approximately to the blue box in (a), and Raman spectra of the BPT linker molecule corresponding to the (c) black, and (d) red crosses on the map.

(AuNPs on the PMMA template) has a yield of approximately 70 % whereas the printing process (transfer from PMMA to substrate) has a yield of roughly 98 %, explaining the missing AuNPs in the arrays. As expected, the substrate alone does not provide any detectable Raman signals (Fig. 4.10d corresponding to the red cross in Fig. 4.10b), as in line with the extremely low probability of Raman scattering occurring. At the AuNP sites, we see a clear Raman signal with the three major peaks at approximately 1075 cm^{-1}, 1280 cm^{-1}, and 1584 cm^{-1}, matching closely with the example spectrum in Fig. 4.9b. As the AuNPs are relatively sparse in the array, with an approximate average separation of 800 nm, it is not expected for any

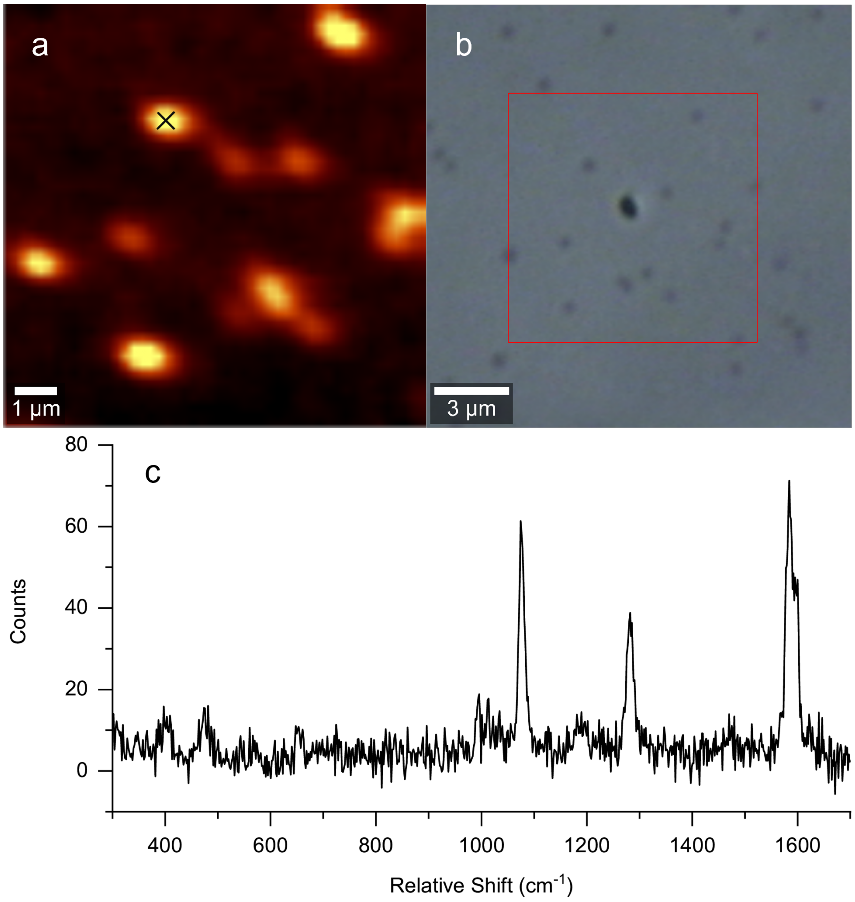

Figure 4.11: (a) Integrated Raman map of spun coated AuNPs on glass between 800-1800 cm^{-1} with (b) the corresponding bright field image. (c) Raman shift spectrum of BPT at the black cross indicated in (a).

coupling effects to be significant at normal incidence and at this excitation. This can be explored by removing the array aspect of the substrate and, instead spin coating the AuNPs over the reporter SAM. In this sample, the AuNP distances can be somewhat controlled by careful consideration of the AuNP concentration and the spin parameters. From the bright field image in Fig. 4.11b, there are large distances between the AuNP spots and therefore can be considered isolated. After scanning across the red area, an excellent spatial agreement can be seen between the AuNPs in the bright field image and the integrated (between 800 - 1800 cm^{-1}) Raman map hot spots. The Raman spectrum obtained at the black cross show clearly the same prominent peaks, indicative of the BPT reporter molecule, at the same intensity as the printed sample.

4.5 Conclusion

In this chapter, Streptavidin-conjugated QDs were immobilized onto biotin functionalized quartz substrates at specific regions within a gold marker array, achieved using a two step EBL process. It has been shown that this method can be used effectively to produce multimaterial substrate based samples with nanometric control. This control has been exploited previously where QDs are shown to couple to lithographically fabricated silver nanoparticle arrays [159] and gold nanoring cavities [160], modifying their lifetime and emission characteristics.

Given the promising initial results of successful surface functionalization and QD attachment, it is exciting to see how the two-step EBL procedure can be extended to an (*N+1*)-step process for N conjugated QDs. This would allow careful probing of the optical behaviour (fluorescence intensity and lifetime) of QDs in different environments near other QD systems and within a plasmonic structure. This is of course provided that the subsequent deposition and removal of PMMA layers do not degrade the quality of the previously deposited QDs on the surface.

In addition, EBL was successfully used to fabricate a robust and reusable template for the fabrication of CAPA substrates. Using the AuNP array made with this method, the Raman signal of the underlying BPT layer is greatly enhanced given that the regions without AuNPs produced no detectable signal. As discussed previously, EBL suffers from low throughput due to the long times necessary for large and/or complex structures, for example spanning multiple write-fields (usually 100 x 100 μm) requiring precise stitching (or alignment). An initial solution to this issue is to remove the need for EBL at the beginning of every fabrication process using new substrates. With the template dissolution method as outlined in Fig. 4.9a, EBL is only required once to create the Si master template from which PMMA is used to create replicas in the subsequent printing process. Since the time required for spin coating and dissolution of PMMA is less (minutes/hours) compared with EBL (hours/days depending on size and complexity of the master template), the throughput is greatly improved. The main disadvantage with this method is the complete lack of flexibility of nanostructure configuration once a template is made. This method has been recently applied to using different polymer transfer materials such as polydimethylsiloxane (PDMS) and OrmoComp [161]. Piolo *et al.* further performed a sequential CAPA fabrication process within a microfluidic channel to allow customized placement of different nanoparticles on the same template replica depending on deposition order and meniscus direction of travel [162].

Unfortunately, the project was ceased early due to the COVID-19 pandemic. If given enough time, the proposed nanostructure that would be fabricated using EBL is illustrated by Fig. 4.12 with the largest QDs in the inner ring and smaller QDs in the outer rings as the distance from the Au increases. The relative positions (and thus the separation distances) of the nanoparticles could be precisely controlled allowing for distance dependent fluorescence/plasmon decay-, and energy transfer-rates to be measured using a variety of different combinations of QDs. From these decay rates, it would be possible to observe a directed transfer of excitonic energy from the outer to the inner ring of QDs. Additionally, the intensity of the QD fluorescence could be measured depending on the distance to the Au and/or the nearby QD rings.

The pandemic highlights the disadvantage of using EBL despite affording the user exquisite control of the nanostructure. For one, the machinery required is costly and so limits the availability of the equipment to only a few places that can afford to purchase and maintain such a device. This causes issues in usage for ex-

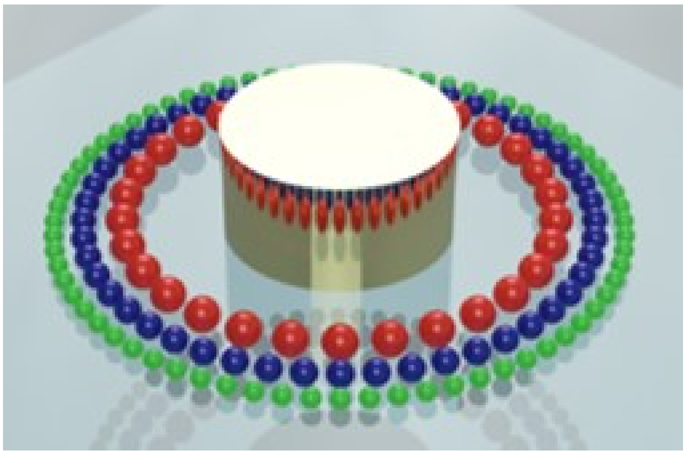

Figure 4.12: The proposed structure to be fabricated using the multi-step EBL process with the evaporation of gold for the central nanodisk, and the subsequent deposition of the differently sized QDs starting with the central ring of red QDs and ending with the outer most green QDs. Note that this schematic is not to scale and the colour representation of the nanoparticles are only used for illustrative purposes.

ternal users to the facility in which the EBL is housed in. Along with the cost and complexity of the equipment, this demands specialist knowledge and expertise in being able to effectively operate the EBL. Although a lower resolution is achieved, modern laser based lithography techniques have been shown to produce large area writes with 1000s of sub-wavelength features at speeds far exceeding the capabilities of EBL [163]. The authors of the study report that they are able to fabricate a large (10x10 mm^2) area write in 5 minutes. Although this feat is impressive, such a solution still does not meet industry requirements of high throughputs that match other similar techniques such as photolithography (although the optical resolution of photolithography is still a limiting factor for high precision applications). Nevertheless, it is still interesting and exciting to see what the next generation of high throughput, nanometric control fabrication techniques will be that use lithographic methods.

Chapter 5

Plasmon Coupled QD Films

5.1 Introduction

As mentioned in chapter 2, the use of QDs in film-based technologies has seen considerable interest in the last few decades in various applications. Of particular interest in this study is their exhibition of Förster/Fluorescence Resonance Energy Transfer (FRET) in which the optical energy of an excited QD is transferred non-radiatively to a nearby QD. Due to their size-dependent tuneable bandgaps, a chain or stack of QDs near each other of increasing or decreasing size may exhibit uni-directional Cascaded Energy Transfer (CET) from the higher energy emitting QDs to the lower energy QDs [164]. Previous works from Mamedov *et al.* [165] and Franzl *et al.* [166] showed that layer-by-layer (LbL) assembly methods are particularly suitable for fabricating multi-layered structures consisting of differently sized QD nanocrystal films. In fact, the work by Franzl et al. was the first to demonstrate this CET where the spatial variation of bandgaps produces a funnel-like structure allowing efficient transfer of excitons towards lower energy QDs. Graded bandgap QD energy transfer systems has also been realised in other works based on film and nanotube based structures for up to 3 distinct QD layers [167–169]. Thin film based QD structures has also been shown to be effective biosensing platforms. Seker *et al.* showed that QD thin films separated by polyelectrolyte peptides could be used to monitor enzyme activity of proteases by monitoring the changes in the FRET lifetime of the donor QD films as the peptide separators where cleaved [170]. The versatility of film-based QD technologies is further highlighted by their demonstration as light emitting devices [171, 172], and as full colour photodetectors [173–175].

The benefit of fabricating film based QD structures is the relative ease in which QDs can be arranged on the 2D plane *via* methods including Langmuir-Blodgett films [176, 177], jet spraying [178], spin coating [171, 179], and simply drop casting [180]. These methods also has the benefit of scalability in which much larger surface areas/substrates can be quickly covered with nanoparticles - an advantage over the inherent issue that currently plagues e-beam based nanolithographic techniques.

For LSP-coupled FRET systems, the surface plasmon of the metallic nanoparticle couples to the QD dipole which introduces an extra decay pathway for the exciton – an energy transfer to the LSP. This treatment of an additional pathway essentially leaves the original, intrinsic decay of the QD unmodified which greatly simplifies the calculation of the decay rates [181]. Although the change in local density of states from the plasmonic nanoparticle influences both the radiative and nonradiative decay rates of the QDs as well as the energy transfer (ET) rates between donor and acceptor QDs [182, 183], this plasmonic influence can still be separated from the intrinsic decay [184]. Some works have been able to calculate the theoretical LSP-coupled FRET rate involving dyadic Green's tensors of the AuNP coupled Donor-Acceptor system [185, 186]. However, these calculations are more cumbersome and still are considered separately from the other decay rate terms. The use of plasmonic nanoparticles has been shown to enhance the PL intensity of QDs and energy transfer rate between donor and acceptor QD species in thin film structures. Su *et al.* utilised silver nanoparticles on a mixed layer of donor and acceptor QDs and demonstrated a PL enhancement of up to 47 times for the acceptor QD and a plasmon enhanced decay rate of 1.22 times for the donor QDs [187]. The relationship between the amount of enhancement of the energy transfer decay rate is intimately tied with the distance between the QD films and plasmonic nanoparticle. In the literature the LSP-coupled 2-layer and non-LSP coupled 3-layer QD structures have been extensively studied, however there is little work conducted on an LSP-coupled 3 (or more) layer QD structure.

In this chapter, the time-resolved emissive behaviour of multiple QD species in a 2D film geometry fabricated using common Layer-by-Layer (LbL) techniques will be explored. The behaviour of these QDs in the presence and absence of a plasmonic particle will be compared, and attempt to elucidate the complex nature of multiple emitters and decay pathways in a LSP-coupled multi-layer QD system.

5.2 Methods

5.2.1 Layer-by-Layer (LbL) Assembly

The substrates used were Corning 20.0 x 20.0 x 0.7 mm glass slides. Firstly, these glass slides were cleaned sequentially in Acetone, Isopropanol (IPA), and water in an ultrasonicating bath for at least 5 mins in each solution and dried under N_2 flow. For a deeper clean (for example with sustained organic contamination after the initial clean), the substrates were left in 0.5% Hellmanex III (Hellma Analytics) overnight or sonicated for 30 mins, which were then rinsed with a copious amount of water. Finally, the substrates were plasma treated for approximately 30 s at 100% power, using ambient air as the process gas. This both removes any leftover organic contaminants and increases the surface hydophilicity ensuring total coverage of the polyelectrolytes (PE) [188]. The substrates were then submerged in a solution of polyDADMAC (2 wt. % in H_2O) which was left for 5 mins before being subsequently

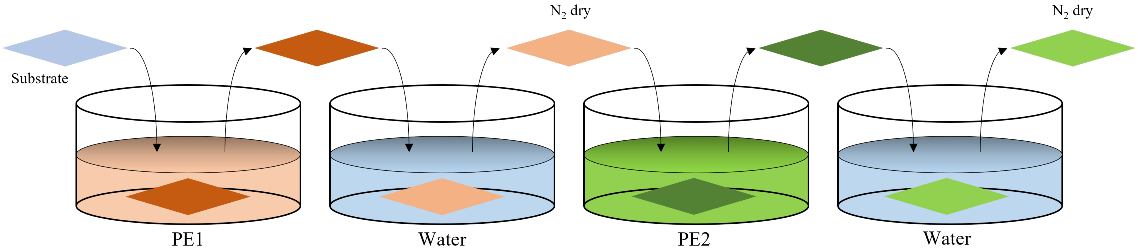

Figure 5.1: A simple schematic illustrating the general LbL assembly with two polyelectrolyte layers (PE1 and PE2) including the the washing and drying steps in between.

submerged in H_2O for approximately 30s and dried under N_2. A solution of as-made AuNPs was diluted by a factor of 2 (reaching an optical density, OD, of approximately 1.0), and 200 μL was used to spin coat over the functionalized glass surface at 1500 rpm for 60 s with 2000 rpm/s acceleration.

Following this, the substrate was then submerged sequentially in alternating baths of polyDADMAC and PSS (2 mg/mL, in H_2O), with rinsing in water and drying as before in between each PE layer. These PE coating steps were repeated as many times as needed, always starting and ending with a polyDADMAC layer before the next nanoparticle layer was added. For the work conducted in this chapter only 3 PE separation layers were used (polyDADMAC/PSS/polyDADMAC). A graphical representation of the LbL assembly is shown in Fig. 5.1 summarising the alternating PE submersion.

Once sufficient PE layers have been deposited, a dilute solution of QDs (approximately 3.2 nM) was drop cast onto the surface using 200 μL - enough to cover the entire slide and was left to dry on a hotplate at 45 °C. The procedure mentioned above was then repeated to add more PE layers - again, 3 PE layers was used - before the subsequent QD layer was deposited. Although contrary to various studies that rely on spin coating QDs onto substrate surfaces [189], it was decided to drop cast dilute solutions of QDs due to the extremely high losses incurred during the spin coating process [178]. Additionally, the dilute concentrations help to minimise

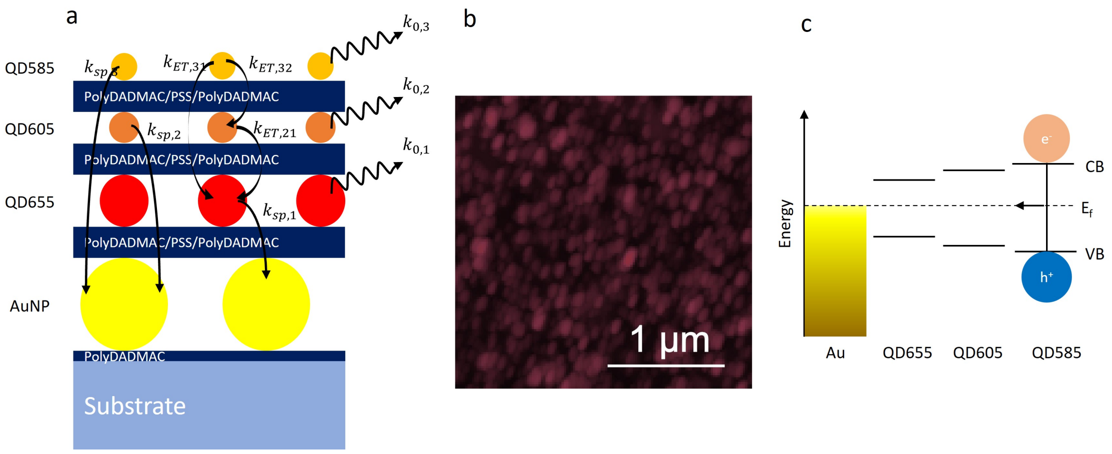

Figure 5.2: (a) Diagram of the AuNP@QD multilayered structure illustrating the possible excitonic decay pathways and the associated decay rates. The wavy arrows represent the radiative decay pathways, $k_{0,i}$, where i denotes the QD layer. The curved arrows are the different non-radiative pathways including the surface plasmon decay, $k_{sp,i}$, and energy transfer, $k_{ET,ij}$, where i and j represent the donor and acceptor layers, respectively. (b) AFM image of a 2 QD layer sample of QD655 and QD605 showing the distribution of QDs. (c) Sketch of the locations of the conduction band (CB) and valence band (VB) for the QDs along with the Fermi level (E_f) of the AuNP for the sample structure illustrated in (a). The cascaded band gaps are visualised by their CB and VB offset which enables the directed energy transfer of excitons.

the potential effects of quenching due to aggregation although it is believed that this is mainly due to electronic coupling rather than excitonic energy transfer [190]. As seen from the AFM map given in Fig. 5.2b, the drop cast method is able to produce homogeneously distributed multilayered QD samples. Furthermore, drop casting solutions onto substrates causes a region of high concentration on the outer edge of the droplet's area - known as a "coffee-ring". To avoid this, the entire substrate was covered (as previously mentioned) so that the coffee-ring was limited to the extreme outer edge of the substrate and all physical and optical measurements were conducted in the central region of the sample.

5.3 The photophysical model

From the fabrication method above, the proposed structure of the full graded-bandgap tri-QD layer on AuNPs is illustrated by Fig. 5.2a with the associated de-excitation pathways of excitons supported by each QD layer. Specifically, excitons in each QD i^{th} layer can de-excite *via* their own intrinsic decay pathway, $k_{0,i}$, but also *via* FRET to QDs in a different layer ($k_{ET,ij}, i > j$ from layer i to layer j), and *via* energy transfer due to exciton-plasmon coupling to the AuNP layer underneath ($k_{sp,i}$). It should be noted that the requirement for the acceptor's energy bandgap to be smaller than the donor's restricts the FRET decay pathway to be unidirectional from the top most QD layer (QD585, $i = 3$ in Fig. 5.2) to the bottom most QD layer (QD655, $i = 1$). Following the kinetics models presented in previous works for multi-layer QD containing layers [53, 191], and extending the photophysical kinetic models within to include multiple QD layers as well as the plasmonic nanoparticles sub-layer, a series of coupled differential equations can then be formulated to describe the exciton density evolution of the system using the above-defined rates of de-excitation pathways applicable to each QD layer:

$$\frac{dn_1}{dt} = -k_{0,1}n_1 - k_{sp,1}n_1 + k_{ET,21}n_2 + k_{ET,31}n_3\,, \tag{5.1a}$$

$$\frac{dn_2}{dt} = -k_{0,2}n_2 - k_{sp,2}n_2 - k_{ET,21}n_2 + k_{ET,32}n_3\,, \tag{5.1b}$$

$$\frac{dn_3}{dt} = -k_{0,3}n_3 - k_{sp,3}n_3 - k_{ET,31}n_3 - k_{ET,32}n_3\,, \tag{5.1c}$$

where n_i refers to the exciton density of the i^{th} pure QD layer at time t after the initial excitation of the layer, which can be thought of as the number of excitons per unit area. Note that, in the model, the effects of charge transfer between the layers are discounted since the presence of the PE layers has been shown to degrade the conditions necessary for charge transfer [192]. The effect of re-absorption or inner

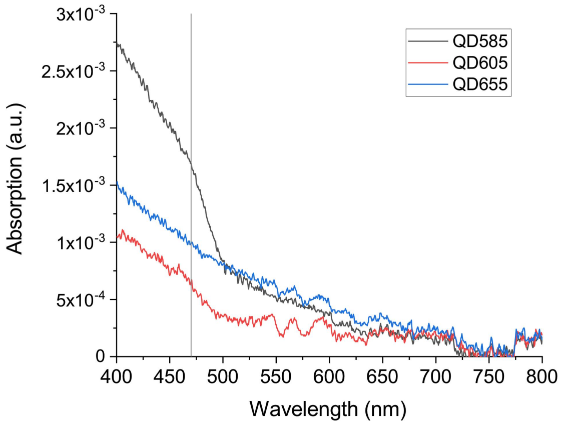

Figure 5.3: UVVis absorbance measurements of QD films on glass substrates. The vertical line corresponds to a wavelength of 470 nm where the absorbance values are used to determine the exciton density.

filtering is also not considered since the thicknesses of all layers are extremely small and the in-layer processes are accounted for in the intrinsic decay rates. Furthermore, and due to the reasons outlined here, we further assume the total absorption of the 3 layers is a sum of the absorption of the individual layers 5.3. From this the initial exciton density for each layer was set to be in proportion of the total summed absorption of the 3QD-layer system at 470 nm. The absorption of the films were measured using UVVis with a substrate holder and can be seen in Fig. 5.3 where the values taken at 470 nm are 1.69×10^{-3}, 6.6×10^{-4}, and 9.9×10^{-4}, for QD585, QD605, and QD655, respectively. Thus, the corresponding exciton densities used in the model for the each of the QD layers are 50.6, 19.8, and 29.6 for the non-LSP coupled system.

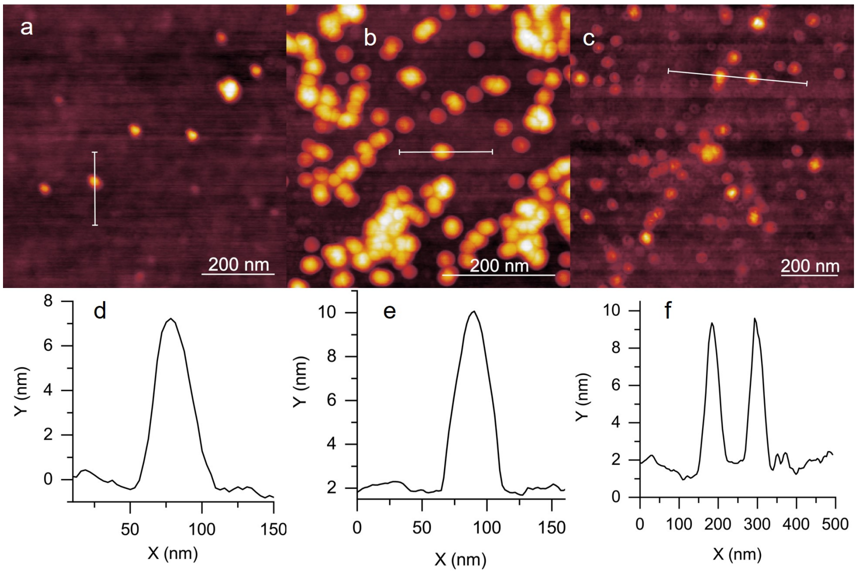

Figure 5.4: Atomic Force Microscopy images of (a) QD655, (b) QD605, and (c) QD585. (d-f) The corresponding line profiles for each image.

5.4 Results

5.4.1 Physical properties

The characteristic diameter of the QDs were measured using Atomic Force Microscopy (AFM) - the images of which can be seen in Fig. 5.4. Using the open source software Gwyddion to analyse the images, the characteristic diameters were found to be 8.05 ± 1.02 nm, 7.74 ± 1.18 nm, and 7.19 ± 1.29 nm for QD655, QD605, and QD585, respectively.

5.4.2 Optical properties

In order to calculate various optical parameters of the QD multilayer system such as the spectral overlap and Förster radius (Eq. 2.4 and Eq. 2.5, respectively), the PL emission and UVVis absorption spectra were measured. These, along with the AuNP absorption are illustrated in Fig. 5.5a, which shows the distinct absorption

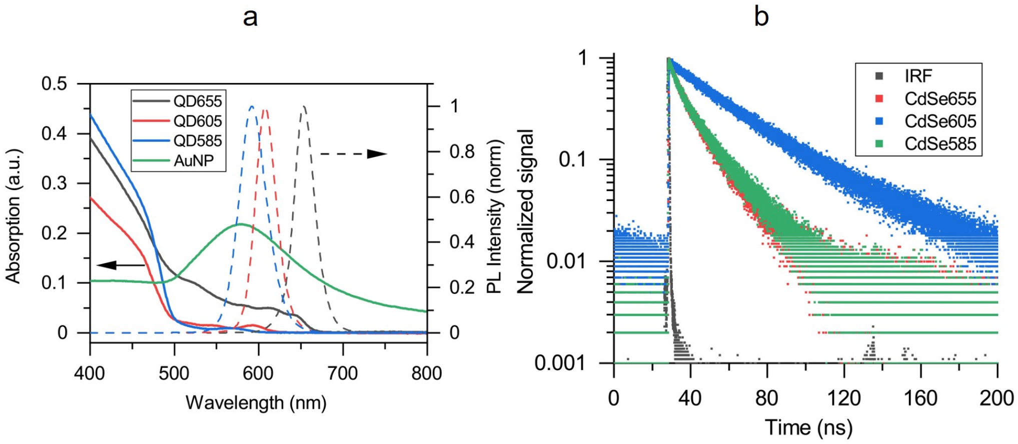

Figure 5.5: (a) UVVis absorption curves of bare AuNP and QDs (solid lines - left axis) and normalised PL emission spectra of QDs (dashed lines - right axis). The concentrations of the QDs used for these absorption spectra were found to be 48.5 nM, 47.1 nM, and 169.3 nM, for QD655, QD605, and QD585, respectively. (b) Lifetime decay curves of pure QD films on substrate.

profile of QDs with an increased absorption strength with decreasing wavelength. Following the Beer-Lambert law (Eq. 3.1), the concentration of the solutions used in the drop casting procedure was calculated given an extinction coefficient of 2,900,000 $M^{-1}cm^{-1}$ (QD655), 1,100,000 $M^{-1}cm^{-1}$ (QD605), and 530,000 $M^{-1}cm^{-1}$ (QD585) all at 488 nm, which were all obtained from the manufacturer. The concentrations were found to be approximately 3.8 nM, 12.2 nM, and 20 nM for QD655, QD605, and QD585, respectively.

Another important quantity required is the photoluminescence quantum yield (PLQY) of the QDs. These were found according to Eq. 3.2b using the reference dyes (with their known, corresponding PLQY) ATTO655 (0.3), Alexa Fluor 594 (0.66), and Alexa Fluor 568 (0.69) to compare against QD655, QD605, and QD585, respectively. To minimise non-linear absorption effects of the reference dyes (such as reabsorption [193]), the solution absorbances were kept low such that, at the excitation wavelength, it was well below 0.1 using a 10 mm quartz cuvette. Three different concentrations of each of the dyes and QDs were prepared, and for each concentration the absorption UVVis was measured. A corresponding PL spectrum

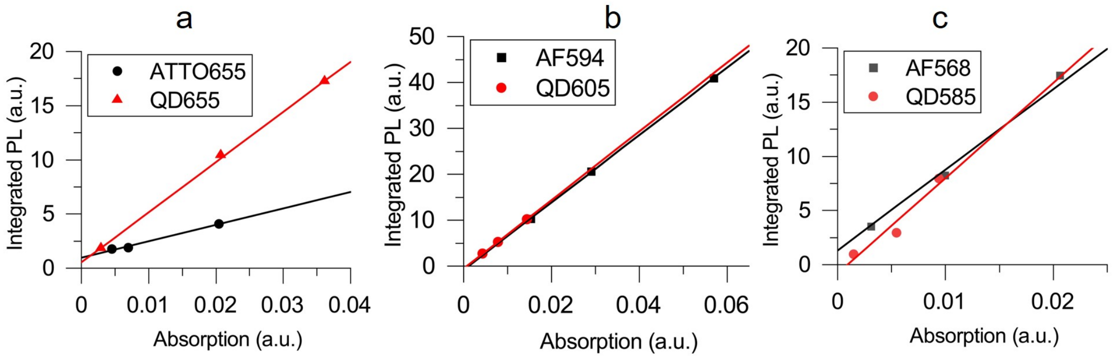

Figure 5.6: Photoluminescence quantum yield emission vs absorption graphs for (a) QD655, (b) QD605, and (c) QD585 measured against their corresponding reference dyes. The red and black lines are their corresponding fits.

was obtained for every concentration with an excitation wavelength of 620 nm for QD655, 590 nm for QD605, and 565 nm for QD585 (and their corresponding reference dyes). The PL spectra was integrated across the wavelength range measured and a graph of integrated PL vs absorbances were plotted for each sample. The wavelength range used to measure the PL was between 640 - 900 nm for QD655, 600 - 900 nm for QD605, and 575 - 900 nm for QD585. As mentioned in the previous chapter, these plots can also be used to ensure linearity between PL and absorbance within the concentration ranges used to verify the validity of the equations used. The PL vs absorption graphs for each of the three samples can be seen in Fig. 5.6 where in all cases, a linear relationship is indeed identified. Fitting a linear model to the graphs and extracting the gradients yielded $(4.63 \pm 0.10) \times 10^5$, $(7.47 \pm 0.05) \times 10^5$, and $(8.80 \pm 2.11) \times 10^5$ for QD655, QD605, and QD585, respectively. Their corresponding reference dye gradients were $(1.51 \pm 0.13) \times 10^5$, $(7.33 \pm 0.07) \times 10^5$, and $(7.44 \pm 0.21) \times 10^5$. Thus, from these gradient values the QD quantum yields were found to be 0.92 ± 0.08 (QD655), 0.80 ± 0.20 (QD605), and 0.67 ± 0.01 (QD585). Next, the lifetime decay of the QDs, as seen in Fig. 5.5b, were extracted by an iterative reconvolution fit with 2 components (wherever possible) which are summarized in Table 5.1.

Sample	(α_1) τ_1 ns	(α_2) τ_2 ns	$\langle\tau\rangle$ ns
QD655	(0.64) 6.57 ± 1.65	(0.36) 19.37 ± 2.61	11.13 ± 1.99
QD605	(-) -	(1.00) 30.35 ± 1.56	30.35 ± 1.56
QD585	(0.63) 7.62 ± 0.81	(0.37) 20.68 ± 1.01	12.44 ± 1.57

Table 5.1: Lifetime of single species QD layers on substrates with the fast (τ_1) and slow (τ_2) decay components. Note that QD605 had only 1 lifetime component and so τ_1 is omitted.

5.4.2.1 Crosstalk

Since the fluorescence lifetime behaviour is used to study the exciton kinetics in each QD layer in a stratified structure, it is important to distinguish between the detected signal from the desired QD channel from other QD signals. This is because the QDs possess a broadband absorption spectrum (see Fig. 5.5a for their absorption behaviour) which leads to the simultaneous excitation of all QD species in the layered samples with a high energy laser source. As briefly discussed in chapter 3, bandpass filters were used to discriminate photons originating from each layer detected at the SPAD. However, as the emission profiles of the QDs are spectrally close to each other, one cannot fully separate the signals using spectrally narrow filters alone. There will be a degree of overlap between other QD emission peaks and the desired wavelength channel set by the bandpass filter window - this is known as spectral bleed-through or crosstalk. This can pose an issue particularly as it can be confused with energy transfer effects. Therefore, one must determine whether crosstalk has any significant effect on the measured lifetime for each QD channel. This was done by measuring the PL of the 3QD layered system (without and AuNP layer) and decomposing the spectrum into its constituent peaks at the 3 QD emission wavelengths by linear unmixing, as shown in Fig. 5.7a. The three peaks were then integrated within each of the optical filter limits (between 575-585 nm for the 580-10 filter, 605-615 nm for the 610-10 filter, and 645-655 nm for the 650-10 filter) to obtain an area which represents the total contribution of each of the QD layers in each of the filter windows, or a

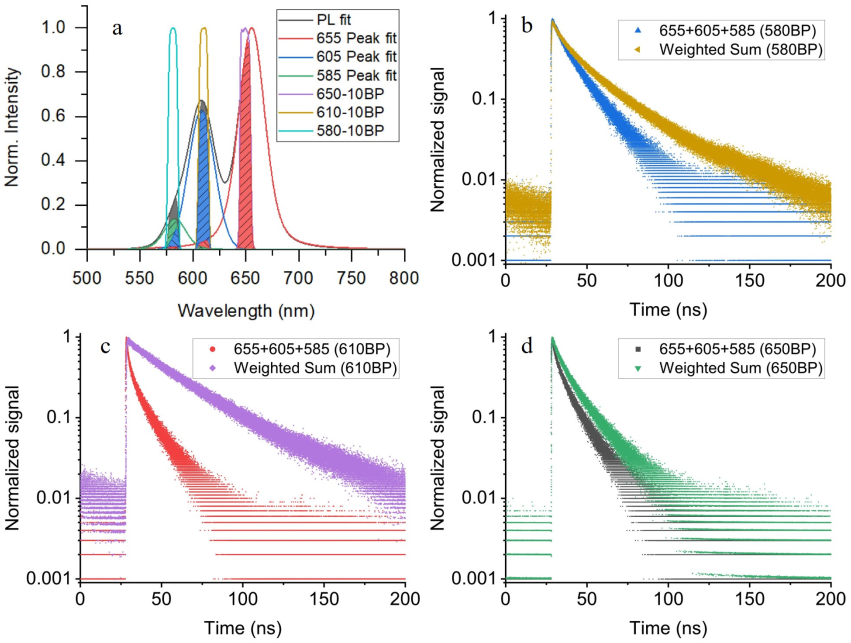

Figure 5.7: Calculation of crosstalk taking the area within each spectral bandpass window in the (a) PL emission spectra of the trilayer and its decomposed peak fits at the QD emission wavelength. The red, blue, and green areas correspond to the QD655, QD605, and QD585 contributions in each window, respectively. (b-d) Comparison in the lifetime decay curves between the measured and calculated by weighted sum for the trilayer

"weight". These contributions are shown as coloured areas in Fig. 5.7a, with each colour corresponding to a QD layer. These weights were then multiplied by the pure QD film lifetime histogram and summed together to obtain a "Weighted Sum" and compared against the experimentally measured lifetime decay of the 3QD layer structure for each detection channel. The weighted sum curve represents a decay of an ensemble of non-interacting QDs, and any deviation from it would indicate some interaction, such as energy transfer. A simple inspection of the comparison between this non-interacting lifetime and the measured lifetime (Fig. 5.7b-d) shows an obvious discrepancy between the two for each channel. Therefore, it was found that the effect of crosstalk had a minimal effect on the measured lifetime using the filters and could be disregarded.

5.4.3 Surface coverage

The surface density (or number of QDs per unit area), σ_{QD}, can be obtained using the Beer-Lambert equation (Eq. 3.1) where the UVVis absorbance is measured through the glass slide so that the optical path length is the thickness of the QD film (i.e., the diameter of the QDs as obtained by AFM measurements). The background corrected absorbance values from each QD film spectra, as shown in Fig. 5.3, at 488 nm were found to be 7.3×10^{-4}, 2.8×10^{-4}, and 9.9×10^{-4} for QD655, QD605, and QD585, respectively. Using the dimensions of the QDs obtained via AFM and extinction coefficients from the previous sections, the volumetric concentration, c, can be found (recall that the Beer-Lambert equation is $A = \varepsilon c l$ where l in this case is the QD film thickness).

Finally, this volumetric concentration can be converted to a surface density via $\sigma_{QD} = cN_A l$, with Avogadro's constant (N_A). Thus, the surface coverage (in units of QDs per square metre) was calculated to be $(1.5 \pm 0.2) \times 10^{15}$ m^{-2}, $(1.5 \pm 0.3) \times 10^{15}$ m^{-2}, and $(11.2 \pm 1.7) \times 10^{15}$ m^{-2}, for QD655, QD605, and QD585, respectively. These values are comparable to the densities found from previous works that also utilise LbL techniques with self assembly linker molecules [194], but lower than those with similar PE spacer layers likely due to the low concentrations used in this chapter [195].

5.4.3.1 Polyelectrolyte thickness

As the FRET efficiency is sensitive to the centre-to-centre separation of the constituent QDs, as well as the plasmon quenching, it is important to characterise, not only the QD sizes but also the polyelectrolyte (PE) thickness. The thicknesses of PE layers vary in the literature with some reporting 1-2 nm for polyDADMAC/PSS bilayers [196] and about 3.3 nm for polyDADMAC/PSS/polyDADMAC trilayers [197]. This variation is likely due to a number of factors that may affect the conformation of the polymer such as pH, molecular weight, and concentration. Firstly, the thickness may be obtained experimentally by scratching the surface of a QD585+605+655 layered sample with a sharp razor and measuring the height difference between the substrate surface and the top of the QD trilayer stack. An example of a scratch and line profile is illustrated in Fig. 5.8. The average height of the 3 QD layer peaks were then subtracted by the average sizes of the QDs to get the total thickness from the 2 PE spacer layers. Through this, it was found that the average polyDADMAC/PSS/polyDADMAC thickness between each QD was 2.7 ± 0.7 nm which is in good agreement with the previous works. Furthermore, as no additional salts were used in the PE baths (acting as counter ions) it is assumed that the adsorption of the PE layers on substrate would produce a relatively flat and uniform layer around the QDs [198].

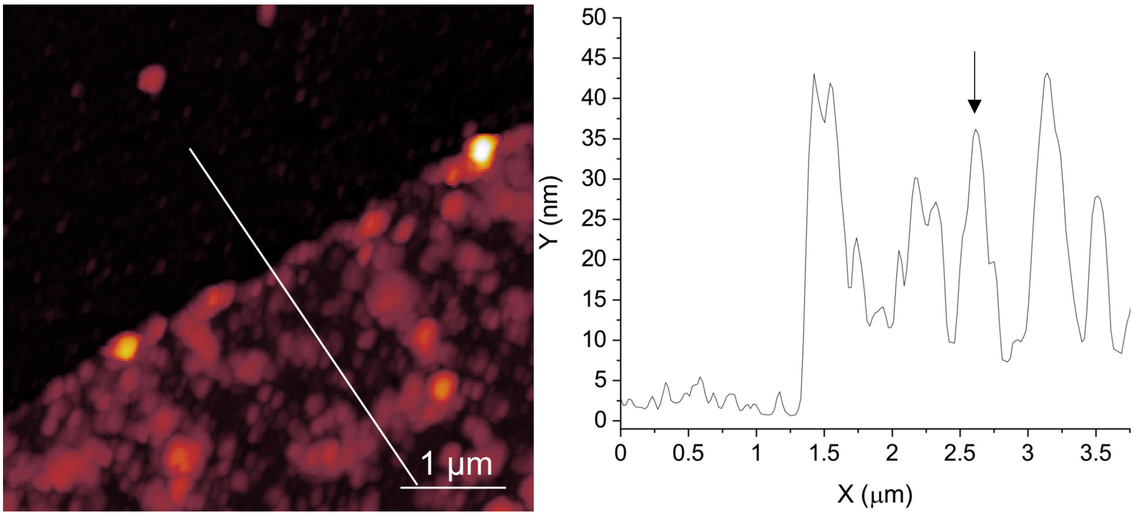

Figure 5.8: An AFM image of a trilayer QD sample with a razor slice to measure the average PE layer thickness. The white line on the AFM image corresponds to the line profile shown on the right side. The arrow indicates the location of an exemplar peak containing the stack of 3 QDs.

5.4.4 Two layer QD films

As discussed in the previous section, it is imperative to find the distances between nanoparticles to fully study their optical behaviour in the context of energy transfer. Another important quantity that is related to this distance dependency is the FRET radius, or R_0. Furthmore, R_0 is unique for each fluorescent donor-acceptor pair and sensitive to their optical profiles, and must be calculated using the experimentally obtained spectra. Firstly, let us recall from Eq. 2.4 that R_0 is proportional to the spectral overlap, $J(\lambda)^{1/6}$. Then, for each QD donor-acceptor pair, the acceptor absorption spectra and donor normalized emission spectra from Fig. 5.5a, an environment refractive index of 1.375 (polyDADMAC), and the orientation factor $\kappa^2 = 2/3$, are taken to calculate the values of J and R_0. Note, that the environment refractive index of the polyDADMAC was taken as the PE films are flexible and the QD films are sparse (discussed later), thus it is assumed that the PE fully encapsulates the QDs such that the local refractive index is wholly due to the polyDADMAC. These are summarized in Table 5.2 for each QD combination.

QD pair (Donor+Acceptor)	Φ_D	J ($nm^4M^{-1}cm^{-1}$)	R_0 (nm)
QD605+655	0.80 ± 0.20	1.45×10^{17}	11.1 ± 0.5
QD585+605	0.67 ± 0.01	1.39×10^{17}	10.73 ± 0.03
QD585+655	0.67 ± 0.01	1.42×10^{17}	10.77 ± 0.03

Table 5.2: The quantum yield of the donor QD, Φ_D, spectral overlap, J, and theoretically calculated Förster radii, R_0, of the 3 different combinations of the QDs used. Here, Eq. 2.4 was used to calculate R_0 using the spectral overlap values.

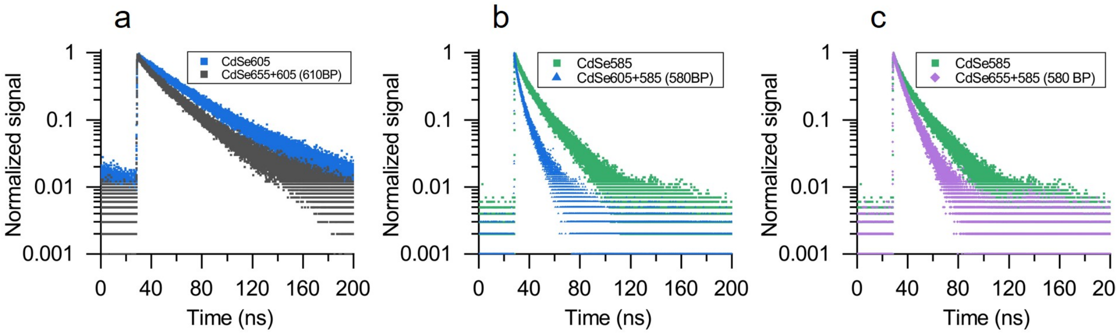

Figure 5.9: Lifetime decay histograms comparing the donor only QD film and the 2-layer donor-acceptor structure measured at the donor wavelength for (a) QD655+605, (b) QD605+585, and (c) QD655+585.

Alternatively, the value R_0 can also be obtained via experimentally obtained parameters with Eq. 2.7. To find the energy transfer rates, the lifetimes of the decay curves for the control QD bilayers are extracted at the donor QD wavelengths and the amplitude average lifetime was calculated. These lifetime decay curves, comparing the donor only and the 2QD-layer structure at the donor wavelength, can be seen in Fig. 5.9.

Using the lifetimes obtained in table 5.3 and Eq. 2.8 (recalling that $k_{ET} = (\tau_{DA})^{-1} - (\tau_D)^{-1}$), leads to an ET rate of $0.009 \pm 0.003\, ns^{-1}$, $0.103 \pm 0.023\, ns^{-1}$, and $0.025 \pm 0.015\, ns^{-1}$, for the QD605+655 (from QD605 to QD655), QD585+605 (from QD585 to QD605), and QD585+655 (from QD585 to QD655) pairs, respectively. Interestingly, the ET rate for the donor in QD605+655, is considerably lower than between QD585+605 despite a comparable spectral overlap and acceptor/donor surface density. This could be due to the larger amplitude associated with the slow

	QD585	QD605	QD655
QD585	16.17 ± 1.44 ns	-	-
QD605	5.44 ± 0.60 ns	30.35 ± 1.56 ns	-
QD655	9.51 ± 1.02 ns	23.60 ± 1.49 ns	11.13 ± 1.99 ns
AuNP	9.34 ± 0.33 ns	14.50 ± 2.05 ns	8.83 ± 0.84

Table 5.3: Experimental lifetimes for single- and double-layer structures. The column header indicates the top layer (donor) of the double-layer structure, while the row header denotes the bottom layer (acceptor). All entries represent the donor lifetime for the specified combination of nanoparticles, except for the same QD entry (shaded) which corresponds to a single QD film. In all double-layer structures, the layers were separated by a single PE spacer thickness of 2.7 nm.

decay component in the 2QD-layer structure. It was found that the fast and slow lifetime (amplitude) components for QD605+655 measured at 610 nm were 27.40 ns (0.73) and 13.52 ns (0.27). The appearance of the fast component from QD605 in the 2QD-layer system clearly indicates the presence of an ET mechanism, however due to the multiexponential decay, calculations involving the average lifetime, $\langle\tau\rangle$, is still preferable.

Finally, with the QD densities obtained previously, the energy transfer rates, the donor QD only lifetimes, and the PE spacer thickness, the experimental value of R_0 for each of the QD pairs can be found. Thus, for the QD pairs QD585+605, QD585+655, and QD605+655, the calculations yields a value of 14.4 ± 1.3 nm, 12.2 ±1.1 nm, and 10.7 ± 1.0 nm, respectively. There is a clear discrepancy between the two values of R_0 (although there is agreement for the QD605+655 sample) which is possibly due to the assumption of the refractive index and the orientation factor values which may not be valid. The orientation factor is only assumed to have a value of $^2/_3$ if the transition dipoles are allowed to orient randomly which, for the film samples used here is not the case as the QDs are fixed and the laser illumination is fixed at normal incidence. Hence, to avoid further assumptions in the calculations, the experimentally calculated values for R_0 will be used.

5.4.5 Plasmon-coupled to one QD film

To identify the effects of plasmonic enhancement on the QD ET system, one must first understand the effect of coupling AuNPs to individual layers of QDs. Firstly, the average nearest neighbour separation distance between the AuNP on substrate was found by measuring the distances between scattering points on a Dark Field image of a spin coated AuNP sample - this was found to be 2.1 ± 0.7 μm from analysis of 60 pairs of nearest neighbours. As such, the particles are considered isolated as plasmonic effects are confined to the nanometre range and the laser spot size is not large enough to excite QDs near more than 1 AuNP (about 820 nm in diameter for a laser wavelength of 470 nm).

Next, the effect of plasmonic coupling of QD layers to the Au NP layer underneath was determined, allowing one to isolate decay rates due to relaxation into the LSP (k_{sp}). The steady-state and time-resolved PL emission spectra of the QD layers with and without plasmonic coupling are shown in Fig. 5.10. This shows a significant increase in the PL for QD585 (5.27 times peak enhancement), and QD605 (2.25 times enhancement), whereas quenching is seen for QD655 (0.05 times of control). Furthermore, the emission of QD585 shows a blue-shift to 575 nm from 585 nm in the control case but a red-shift is observed for QD605 to 613 nm from 606 nm. No spectral shift was observed for QD655. However, the steady-state emission is dependent on local concentrations of QDs at the laser spot whereas the lifetimes are not expected to vary and so changes in the lifetime are more indicative of plasmonic coupling (or other electronic/excitonic changes). Therefore, the bulk of the analysis will concentrate on the lifetime changes of the QDs, though it is still noteworthy to point out the change in PL behaviour.

The plasmon coupled excitonic decay is often reported as an extra decay pathway, similar to FRET, which manifests as a fast decay component in a measured lifetime

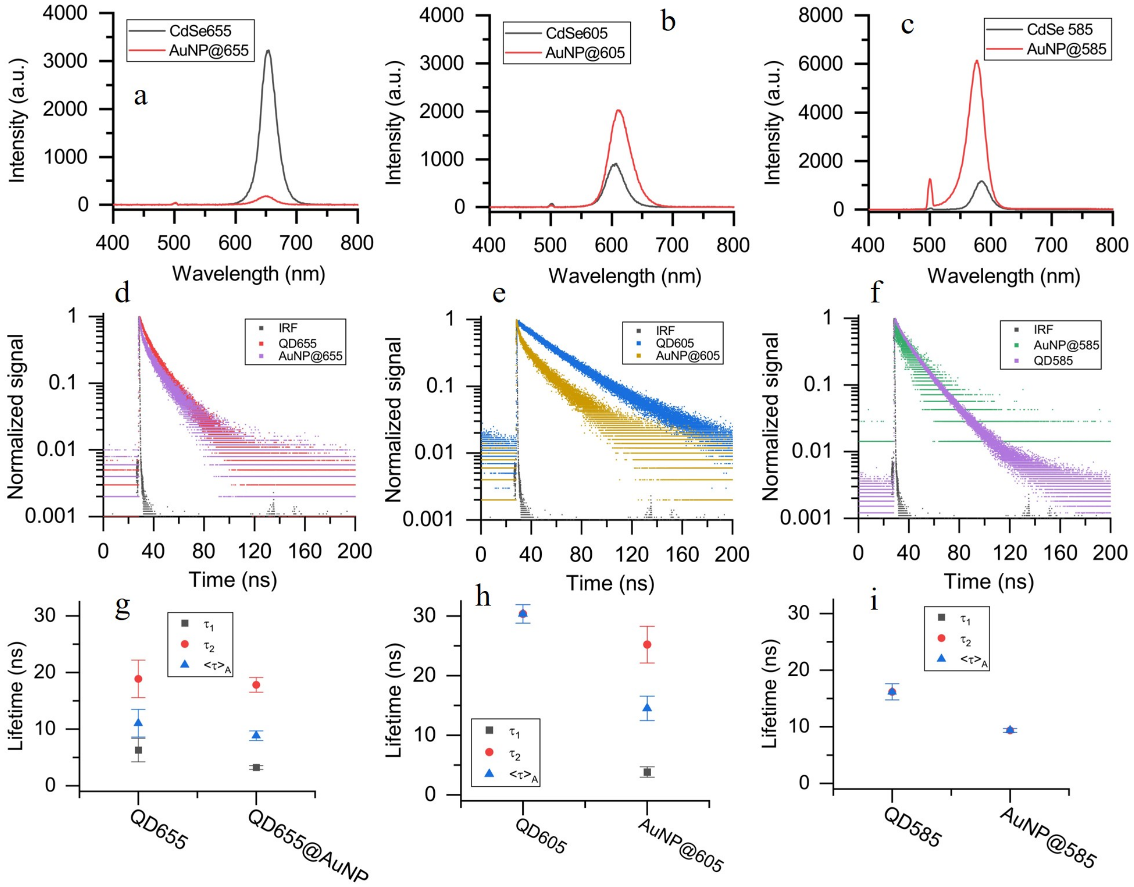

Figure 5.10: (a-c) PL emission spectra of QD and AuNP coupled QD films at each emission wavelength. (d-f) Time-resolved emission spectra of the corresponding QD and AuNP@QD films with the (g-i) extracted, corresponding lifetimes.

[26, 52, 53, 199–201]. It is denoted here as $k_{sp}(d) = k_{sp,rad} + k_{sp,nr}$ to reflect the distance dependency between the nanoparticles and the extra radiative, $k_{sp,rad}$, and non-radiative, $k_{sp,nr}$, decay rates introduced by the metal - which is inserted into Eq. 2.2 as

$$\tau_{Au-QD} = \frac{1}{k_{rad} + k_{nr} + k_{sp}(d)}\,, \tag{5.2a}$$

$$k_{sp}(d) = \frac{k^0_{sp}}{1 + (d/R_{0,LSP})^6}\,. \tag{5.2b}$$

Here, $R_{0,LSP}$ is analogous to the FRET R_0 but between the AuNP and QD, and k^0_{sp} is the maximum quenching rate due to surface plasmons (SP) as though the QD is in direct contact with the AuNP (not including charge transfer effects). It is worth noting that Eq. 5.2b follows a FRET-like $1/d^6$ distance-dependency relationship for the QD-plasmon decay rate. This is due to the AuNP being large enough to support a LSP resonance dipole mode which can interact with the QD dipole [202, 203].

Using Eq. 5.2a, the decay rate due to relaxation into the LSP is calculated by $1/\tau_{Au-QD} - 1/\tau_{QD}$. With the lifetimes in Table 5.3 for the AuNP coupled QDs, and the pure QD films yields a k_{sp} of 0.045 ± 0.007 ns^{-1}, 0.036 ± 0.010 ns^{-1}, and 0.023 ± 0.019 ns^{-1} for AuNP coupled to QD585, QD605 and QD655, respectively. These values are of the same order as similar, previously calculated AuNP-QD systems [26, 53]. Given the emission of the higher energy QD matching more closely to the LSPR peak of the AuNP compared to the lower energy QD, it is unsurprising to see increase k_{sp} with increasing QD emission energy. Alternative treatments for the AuNP coupled QDs include the modification of the radiative rates due to the plasmonic field enhancement and change in the local density of optical states - a phenomenon known as the Purcell effect (as discussed in a Chapter 2) [38]. As the PLQY of the QDs are high (in the QD655 case it is close to unity), it is not expected for the radiative rate to increase considerably compared to the non-radiative transfer to the metal nanoparticle. Hence, the additional plasmonic rate can be considered separately.

5.4.5.1 Au-QD FLIM

The spatial dependency on the lifetime of QDs around AuNPs were briefly studied for QD655 to demonstrate the variance in the decay curve profiles. As expected from Fig. 5.11, the QDs on and near the AuNP display a fast (5.49 ± 0.53 ns, red circles) and slow (22.06 ± 0.76 ns, black squares) decay component due to the plasmonic coupling of the exciton which averages to 11.25 ± 1.03 ns. Once the excitation is far enough away (approximately 2 μm away in X and 3 μm in Y), the lifetime reverts back to a single exponential decay and increases to 18.83 ± 1.86 ns, indicating a plasmonic decay rate (k_{sp}) of approximately 0.036 ns^{-1} (as obtained in the previous section). Interestingly, the distance away from the AuNP at which the lifetime becomes mono-exponential is farther than expected at around 2-3 μm. Possible explanations include the fact that the calculated spot size is an idealized one and so, realistically, the laser spot may be larger due to imperfect focusing on the AuNP. In an ideal case, the spot size (Airy disk) would only be around 820 nm in diameter using the 470 nm laser with a 0.7 NA objective. However, this assumes the alignment is perfectly focused and the rear of the objective is uniformly illuminated - both of which may not be the case given the beam profile is Gaussian. Therefore, this results in a larger spot size than predicted by common Airy disk diameter calculations (1.22λ/Numerical Aperture). The centre of the beam spot may also not be precisely on the AuNP due to the difficulty in determining the beam centre location when obscured by the QD fluorescence as seen on a camera. There also exists a relatively large region around the central AuNP with reduced lifetime and enhanced PL. It is not immediately clear as to the origin of this dark strip as it was ensured that only one AuNP was present in the scan area (due to

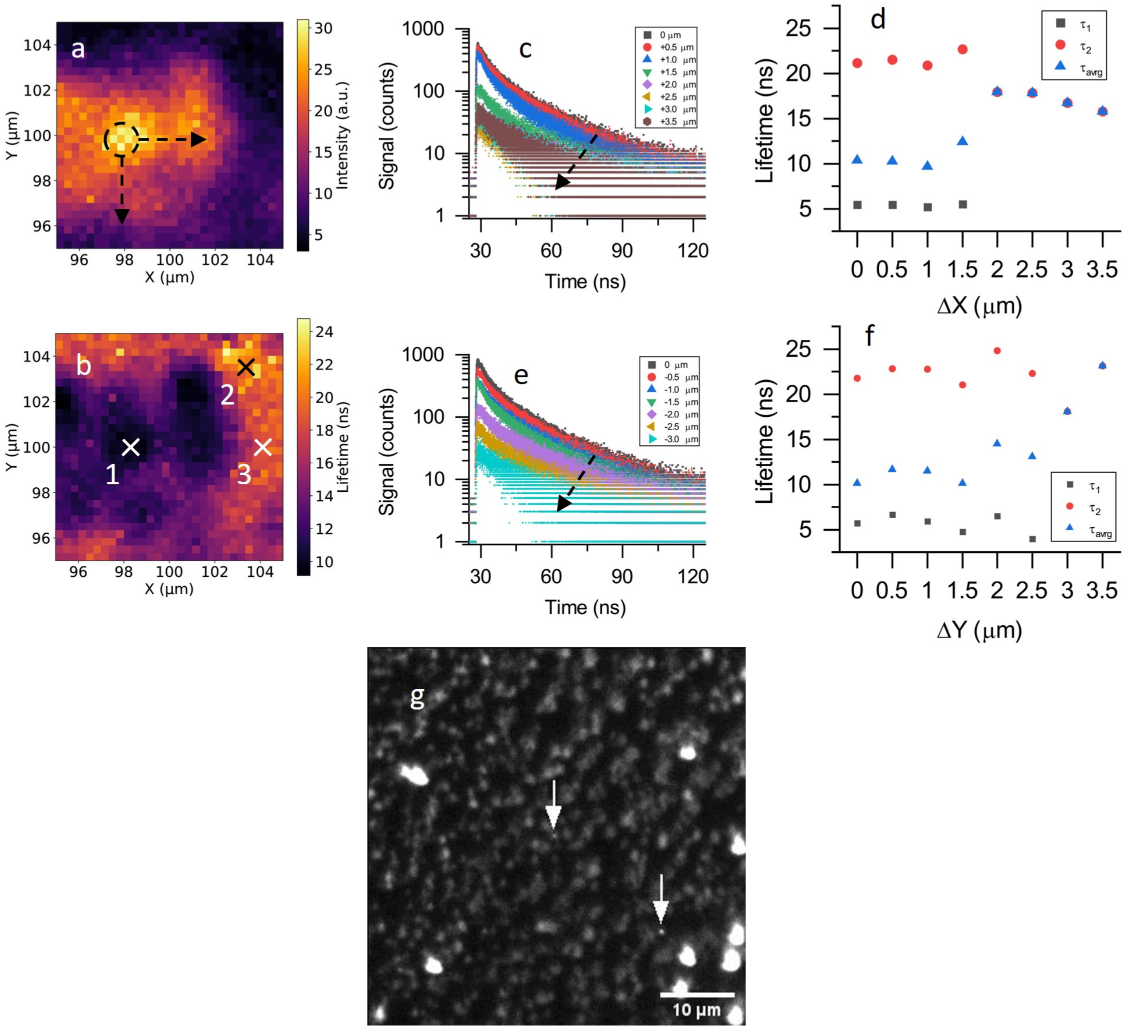

Figure 5.11: (a) 30x30 scan FLIM intensity image (from the lifetime histogram amplitude taken at each pixel) of an AuNP (approximately at the dashed circle) covered by a film of QD655, and integrated at 1000 ms per pixel. (b) Corresponding lifetime fit image of (a) where the numbered crosses indicate the regions in which the binned pixel lifetimes are evaluated. (c) Lifetime decay curves for a distance (indicated by the legends) away from the AuNP in X with (d) the extracted lifetimes. (e, f) Lifetime curves and extracted values for Y direction. Each curve corresponds to a point evaluated for a constant 1000 ms and the dashed lines show the direction of travel for the corresponding axes. (g) Representative dark-field optical image of the AuNP@QD655 sample where the arrows indicate the position of AuNPs in the field of view.

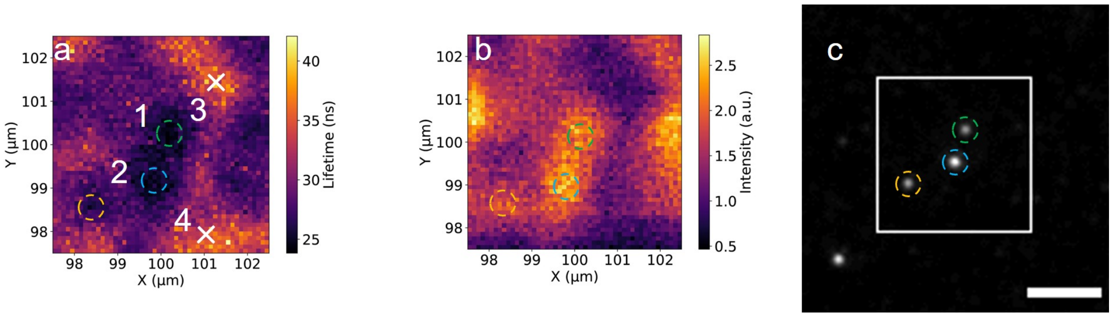

Figure 5.12: (a) Lifetime, and (b) fluorescence intensity map of a QD605 film over dispersed AuNPs (50 x 50 pixels in size), and integrated for 250 ms per pixel. (c) Dark field image of the AuNPs where the white box indicates the approximate scanned area. The coloured circles indicate the approximate locations of the corresponding AuNPs across the three images. The scale bar is 10 μm and numbered circles/crosses indicate the location at which the binned pixel lifetimes are evaluated.

the sparsity of the sample region seen in Fig. 5.11g). It is possible that the local distribution of QDs is not as homogeneous, nor the AuNP as sparse (particularly if obscured by a thicker than usual layer of QDs viewed on camera and through an eye piece), as initially assumed. Then, there may be other AuNPs hidden from view under a higher than expected concentration of QDs in the dark spots around position 1 in Fig. 5.11b causing the reduction in lifetime and enhancement in PL much further away from position 1 than expected. Nevertheless, this demonstrates rather well the lifetime modification of QDs when near and far from AuNPs. This spatial effect is demonstrated by Fig. 5.11c and Fig. 5.11e in the increase in the average lifetime at a certain distance away.

Similar behaviours can be seen in the lifetime and FLIM amplitude maps for QD605 (Fig. 5.12) and QD585 (Fig. 5.13). In either case, quite a good agreement can be seen between the location of the lifetime dark spots (shorter lifetimes), amplitude hot spots (higher fluorescence intensity), and AuNP scattering spots in the Dark Field. A slightly different approach to analyse the samples was also taken for these two lifetime maps. The decay curves of the corresponding pixels were used in the fitting procedure instead of remeasuring over the same spots at longer inte-

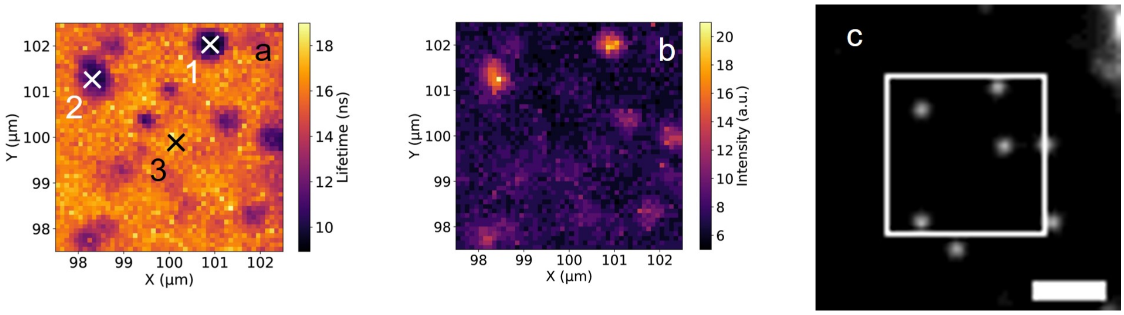

Figure 5.13: (a) Lifetime, and (b) fluorescence intensity map of QD5855 over AuNPs (50 x 50 pixels in size), integrated for 250 ms per pixel. (c) Corresponding dark field image where the white box represents the approximate scan area. The scale bar is 5 μm and numbered crosses indicate the location at which the binned piel lifetime are evaluated.

gration times. As the conventional non-linear least-squares method requires high photon counts for reliable analyses, pixels around a region of interest (ROI) were binned and the photon histograms were summed together to increase the total photon budget available. Typically, the bin size was 3x3 (unless otherwise stated) with the central pixel taken as the ROI allowing for a more accurate determination of the regional lifetime. To verify this, the lifetimes of each pixel was extracted and the average obtained in order to compare against the binned lifetime.

For AuNP@QD655, 3 ROIs were evaluated: at the AuNP location (position 1), and two relatively far away from the AuNP without AuNP (positions 2, and 3). The fitting procedure for the lifetime decay curves are as before and the output values are summarized in Table 5.4. Similarly for AuNP@605, 4 ROIs were investigated: positions 1 and 2 correspond to AuNP locations, whereas positions 3 and 4 do not. Finally, in the case of AuNP@585, the 3 ROIs evaluated are positions 1 and 2 which are at AuNP locations, and position 3 is far away from an AuNP. The sample lifetimes are also summarized in Table 5.5 and Table 5.6, respectively.

From these tables and figures, it is apparent that the lifetime of the QDs are reduced at the AuNP locations. Although they are different to the lifetimes presented in the previous section, these QDs have considerably lower photon counts

Region of Interest	Binned lifetime (ns)	Averaged lifetime (ns)
1	9.55	9.85 ± 0.34
2	18.27	20.29 ± 1.99
3	15.47	16.91 ± 1.32

Table 5.4: AuNP@655 FLIM image lifetime values at each Region of Interest (ROI) of the binned and pixel sum averages.

Region of Interest	Binned lifetime (ns)	Averaged lifetime (ns)
1	24.33	24.64 ± 0.48
2	24.60	25.09 ± 0.61
3	35.88	35.93 ± 2.15
4	35.88	35.92 ± 0.70

Table 5.5: Summary of AuNP@605 FLIM image lifetime values are each ROI of the binned and pixel sum averages.

(on the order of 1×10^5) than before (over 1×10^6 photon events). Note that the AuNP@585 lifetimes obtained here are used in the plasmon decay lifetime calculations in the previous section as the QD batch were the same. Interestingly, although the image in Fig. 5.12a clearly shows a darker spot in the circled region labelled 2, the extracted lifetime is not significantly different compared to the expected QD only regions in position 3 and 4. This is opposite to position 1 suggesting a higher efficiency coupling between the QDs and LSP which isn't necessarily the case in all QD-AuNP pairs (possibly due to a thicker PE spacer). Again, assuming the lifetime of the LSP-coupled QD film takes the lifetime of the form 5.2a, the energy transfer rate to the surface plasmons was found to be approximately, 0.052 ns^{-1}, 0.005 ns^{-1}, and 0.045 $^{-1}$, for AuNP@655, AuNP@605, and AuNP@585, respectively. These values match closely with those found in the previous section, with the exception of QD605. As seen in the fluorescence intensity map given in Fig. 5.12b, the maximum intensities measured around the AuNP are an order of magnitude smaller than for the other two QD maps. The local concentration of QD605 at these locations could be lower than for the other two resulting in fewer photon emissions which would directly impact the quality of the fitting algorithm due to the smaller photon budget

Region of Interest	Binned lifetime (ns)	Averaged lifetime (ns)
1	8.93	9.34 ± 0.33
2	9.91	10.42 ± 0.28
3	15.48	16.17 ± 1.44

Table 5.6: Summary of AuNP@585 FLIM image lifetime values at each Region of Interest (ROI) of the binned and pixel sum averages.

available from Eq. 3.9.

In all cases, alongside a reduction in lifetime, an increase in the fluorescence can also be observed around the AuNP (as seen in Fig. 5.11a (AuNP@655), Fig. 5.12b (AuNP@605), and Fig. 5.13b (AuNP@585)). As the PLQYs of the pure QDs are known, as well as the lifetimes, the change in the radiative decay rates of the QD layer in the presence of a plasmonic AuNP can be found and thus, the Purcell factor as described by the expression given in Eq. 2.20, noting that it is assumed the plasmonic particle does not affect the intrinsic decay rate of the QD. Following the calculation yields 1.28 ± 0.24, 2.15 ± 0.43, and 2.09 ± 0.19, for AuNP@655, AuNP@605, and AuNP@585, respectively.

Alternatively, the change in the fluorescence intensity using the lifetime decay curve maxima ($I(t = 0)$) from the bare QD film to the LSP-coupled QD emission can be used with Eq. 2.21. This allows one to calculate the change in the radiative rate of QDs, and therefore inform us of the Purcell factor by the enhancement in the radiative rate. In this case, the pixels corresponding to the AuNP positions are chosen if the lifetime amplitude are above a certain threshold (which is set to be about 0.6-0.8 of the global maximum amplitude value), and amplitudes less than this threshold are taken as the QD layer background. The average intensity values for these categorized pixels are averaged and the ratio of the two are taken as the enhancement factor (and thus the Pucell factor) of the decay rates. Thus, the average FLIM intensity values for the LSP-coupled QDs, QD background, and subsequent Purcell enhancement factor is reported in Table 5.7. Comparing the F_P values calculated previously using the decay rates with those calculated by the change in fluorescence lifetime intensity shows good agreement between the two methods. This also supports the equivalency between the mathematical treatments of having k_{sp} as a separate de-excitation pathway that does not affect the intrinsic radiative rates of the QDs (decay rate calculations), with the metallic nanoparticle directly influencing the excitation and emission rates of the QDs (fluorescence intensity calculations).

Sample	AuNP@QD	Background	F_P
QD655	15.53 ± 1.67	7.61 ± 2.30	2.04 ± 0.65
QD605	9.22 ± 0.41	4.84 ± 0.37	1.90 ± 0.17
QD585	16.28 ± 1.63	6.88 ± 0.78	2.36 ± 0.36

Table 5.7: Fluorescence lifetime decay intensity maxima ($I(t = 0)$) extracted from the FLIM maps of the QD layer at the AuNP position (AuNP@QD column) and for the QD background. The ratio of the AuNP@QD and background values give the Purcell enhancement factor, F_P.

Furthermore, the PLQY of the LSP-coupled QDs can be calculated with Eq. 2.19 leading to values of 0.937 ± 0.065 for AuNP@655, 0.896 ± 0.106 for AuNP@605, and 0.809 ± 0.019 for AuNP@585. From these, there is a slight increase in the corresponding PLQY of the LSP-coupled QDs with an enhancement of 1.02, 1.12, and 1.21 times from the control (non-LSP coupled film) values (recall they were 0.92, 0.80, and 0.67, respectively). As mentioned before, this slight increase is expected given the already high PLQY values for the control QDs. There is also the trend where the amount of enhancement increases as the difference between QD emission and AuNP LSP resonance peaks decreases (i.e., the higher energy emission QDs matches more closely with the LSP peak) which follows with the LSP-coupled decay rates calculated in the previous section.

5.4.6 AuNP Coupled to two-layered QD films

Not only is the decay rate of individual QDs enhanced, manifesting in a shortening of the average lifetime, but the ET between coupled QDs can also be enhanced [186, 204, 205] at distances close to the surface of the metal. However, studies of AuNP weakly coupled to FRET pairs demonstrate a minimal effect on the FRET rate at distances of up to 10 nm for AuNPs of up to 20 nm in diameter [206] - AuNPs of these sizes are known to exhibit LSP resonances and so may behave in a similar way to the AuNPs used in this study [207].

Although less preferable to formulate conclusions using the steady-state PL spectra due to the local concentration dependence, the graphs shown in Fig. 5.14c, and Fig. 5.14i demonstrate an enhancement in the acceptor peak (with a corresponding quenching in the donor peak) whereas Fig. 5.14f shows relative quenching for both QDs. To more easily compare the lifetimes, the extracted values are plotted in Fig. 5.15.

To begin with, let us consider the lifetime of the QD655 acceptor in the QD655+605 pair where the addition of a donor QD605 appears to increase the average lifetime (14.04 ± 2.39 ns), although not significantly within the margin of error from the control lifetime of 11.13 ± 1.99 ns (Fig. 5.15a). An increase in lifetime of the acceptor would be characteristic for ET as shown by Ozel *et al.* in a similar LbL fabricated AuNP-coupled QD films [200]. This increase in acceptor lifetime is much more pronounced with the addition of AuNP to 15.75 ± 0.66 ns (AuNP@655+605). The same can be said for the QD655 acceptor in the QD655+585 pair where the average lifetime is increased considerably to 19.72 ± 2.25 ns. Conversely, for QD605+585, the lifetime of the QD605 acceptor decreases to 16.68 ± 2.08 ns. Similarly, in the prescence of AuNP, we see a reduction to 4.43 ± 0.65 ns (AuNP@605+585). It is possible to explain this behaviour by considering the different decay pathways as competitive in nature. The model provided in Eqns. 5.1a - 5.1c, the energy transfer term $k_{ET,ij}$ will be positive for an acceptor QD layer (for a 2QD-layer system, this will be layer j), which suggests the exciton density increases by this rate. If this energy rate is dominant (particularly with plasmonic enhancement) then excitons are excited in the layer faster than they can de-excite leading to an increase in the detected fluorescence lifetime. Conversely, if it is not a dominant process, the measured lifetime may decrease.

Further evidence of this LSP-coupled FRET is provided by the consistently decreased average lifetimes of the donor's emission in the AuNP@2QD systems. This is the case for all three QD pairs as can be seen in Fig. 5.15d-f. This reduction in lifetime is not significantly present in the QD655+585 case where the lifetime of QD585 layer was measured to be 8.01 ± 2.02 ns in the presence of AuNP (i.e., AuNP@QD655+585), indicating no decrease in the average lifetime within the margin of error. For the AuNP@QD655+585 case, a reduction in the fast and slow lifetime components can be seen from Fig. 5.15f, indicating that there is indeed some influence on the decay characteristics of the QD585 layer due to coupling to LSP. In this case, the lack of variation in the measured average lifetime is due to changes in the component amplitudes (α_i), of the extracted fast and slow lifetimes.

Given the donor lifetimes, the LSP-coupled FRET rates is calculated by modification of Eq. 2.3 to

$$k_{LSP-FRET} = \frac{1}{\tau_{AuNP@AD}} - k_{sp}(d')\,, \tag{5.3}$$

where the subscript AuNP@AD indicate the AuNP coupled to the acceptor+donor system, and $k_{sp}(d')$ corresponds to the calculated plasmon decay rate of a donor QD at an extended distance, d', away from the AuNP (using Eq. 5.2b). It should be noted that with the addition of an acceptor QD layer, the separation distance between the donor QD layer and AuNP will naturally be different than in the AuNP-donor only case considered earlier. With this in mind, the energy transfer rate for AuNP@QD605+585 (from QD585 layer to QD605) increases to 0.297 ± 0.007 ns^{-1}

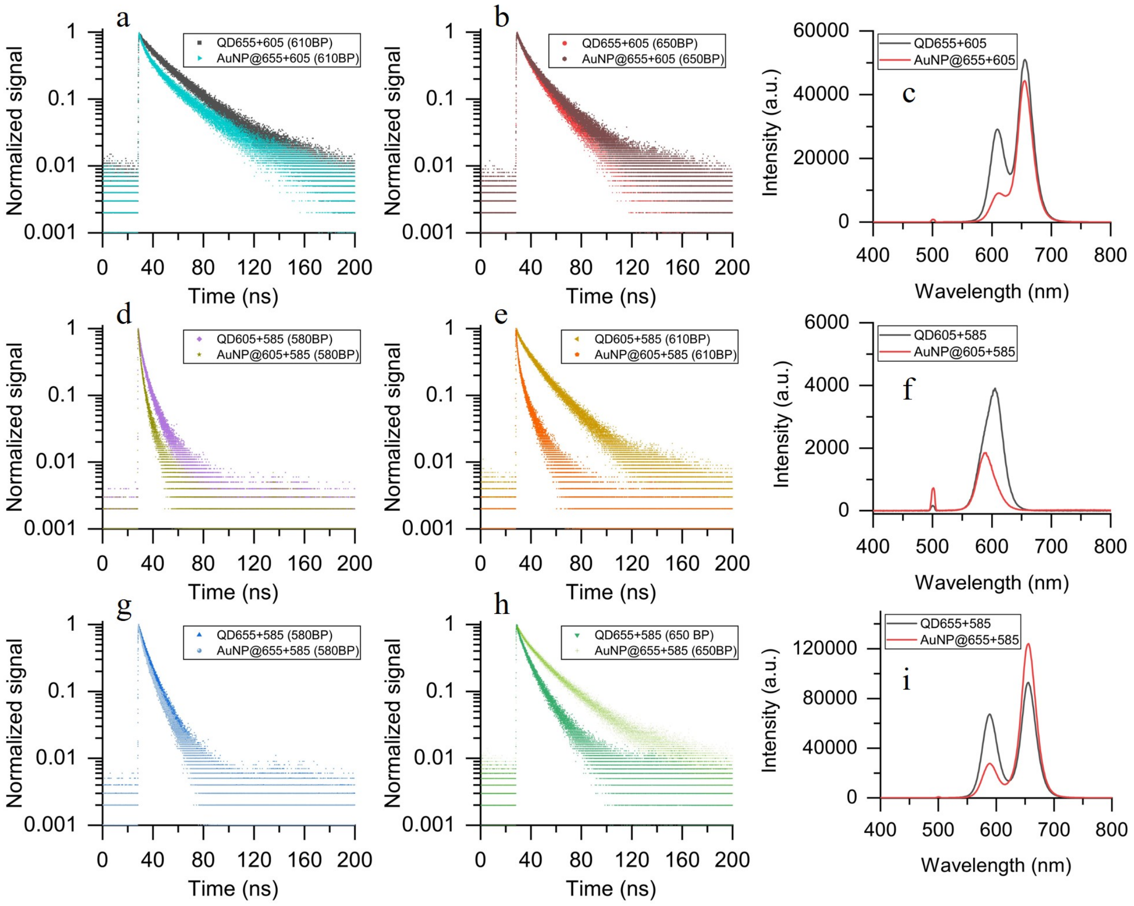

Figure 5.14: (a) Lifetime decay curves of QD655+605 with and without AuNP coupling measured at QD605, and (b) QD655 wavelengths with (c) the corresponding PL emission spectrum. (d) Lifetime decay curve comparison for QD605+585 at QD585 emission, (e) QD605 emission, and (f) PL spectra. (g) Lifetime curve comparison of QD655+585 measured at QD585, (h) QD655, and (i) PL spectra of the corresponding QD bilayer.

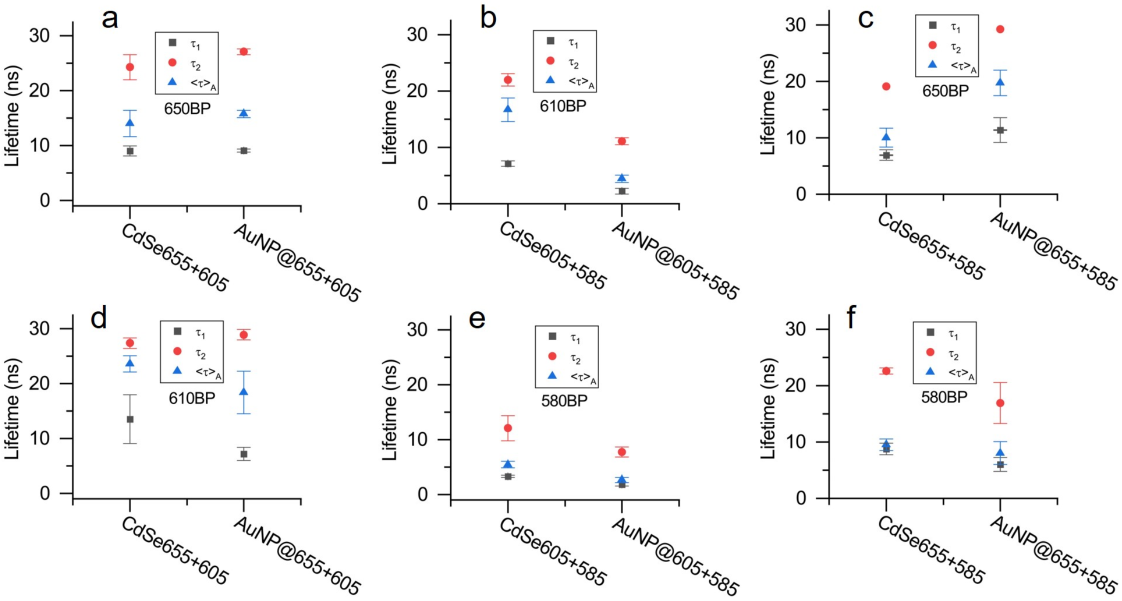

Figure 5.15: (a-c) Extracted acceptor lifetimes of QD bilayers for QD655+605, QD605+585, and QD655+585, respectively, with and without LSP-coupling. (d-f) Extracted donor lifetimes for the corresponding QD bilayers.

with plasmonic coupling, translating to an enhancement of 2.4 from the control case (0.122 ns^{-1}). Conversely, no significant change is observed for AuNP@QD655+605 which yields a calculated transfer rate of 0.007 ± 0.013 ns^{-1} from QD605 to QD655 layer (compared with a control energy transfer rate of 0.009 ns^{-1}). Similarly, the transfer rate for AuNP@655+585 (from QD585 to QD655) was found to be 0.044 ± 0.034 ns^{-1} (in comparison to a control energy transfer rate of 0.043 ns^{-1}). This indicates that the presence of a plasmonic body can increase the rate at which excitons are transferred between donor and acceptor QDs but is unexpected for the QD655+605 and QD655+585 system. In either case, the LSP-FRET rate either is unaffected or is adversely affected which is indicative of weak plasmonic coupling to the donor QD, as suggested by Bohlen *et al.* [206]. Despite this, there is clearly a reduction in the average and/or component lifetimes for the donors. On the other hand, a large enhancement in the ET rate is seen for AuNP@QD605+585

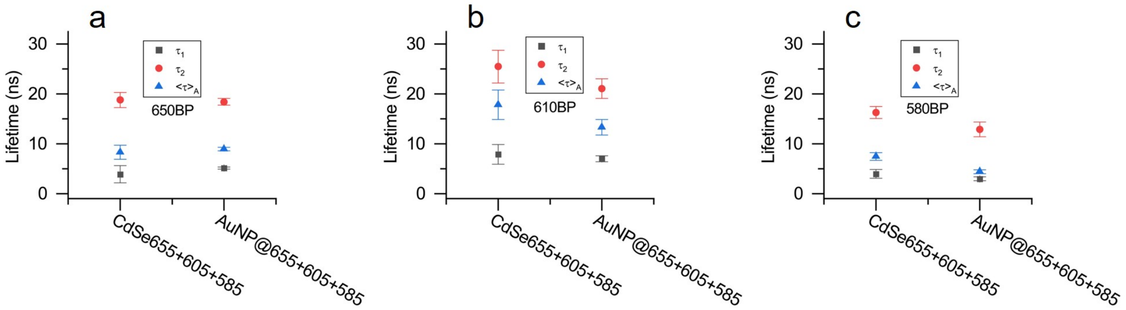

Figure 5.16: Extracted lifetimes of the QD trilayer (with and without plasmonic AuNP) where the decays were obtained at wavelengths corresponding to (a) QD655, (b) QD605, and (c) QD585.

which evidently suggests there is strong plasmonic enhancement in the LSP-coupled QD605+585 layered sample.

5.4.7 Plasmon coupled QD trilayer

Before delving into the beast that is the LSP-coupled QD trilayer, let us first re-examine the QD655+585 case as it will be necessary to compare the expected results against the effect of adding an intermediate QD layer. Along the same analytical path as in the previous section, we first determine the ET rate from the QD585 layer to the QD655 layer at a separation distance that includes the average diameter of QD605 for the control case using Eq. 2.7. This yields a value of $(1.1 \pm 0.4) \times 10^{-3}$ ns^{-1} which, in comparison to the intrinsic decay rates, is virtually negligible at these distances.

Now to examine the control trilayer system (QD655+605+585 in the absence of AuNPs) - due to the presence of multiple acceptors of a similar species, the term "energy transfer" rate becomes ambiguous for the donor QD585. A more appropriate term would be to consider the energy extraction rate instead. Although the calculation is virtually identical and conceptually there is little difference, it is worth pointing out for the sake of clarity. Although it was found above that the energy transfer from QD585 to QD655 at an extended distance is negligible, this may not be the case in an LSP-coupled system. Like before, let us examine the case for the purely donating QD585 in the control 3QD layer system - the lifetime of which was found to be 7.44 ± 0.76 ns, equating to a decay rate of 0.134 ± 0.014 ns^{-1}. Therefore, it is simple to calculate the energy extraction rate of the trilayer by subtracting the intrinsic decay rate of the pure QD film, obtaining a rate of 0.073 ± 0.015 ns^{-1}. This is somewhat surprising as this is a marked decrease in the extraction rate compared with the QD605+585 (which was 0.122 ns^{-1}) suggesting the addition of QD655 decreases the extraction efficiency of the outer most layer.

In the AuNP@QD655+605+585 full layered structure, the lifetime in the QD585 layer was measured to be 4.41 ± 0.40 ns. Taking into account the expected k'_{sp} as before (with a separation distance between the AuNP and QD585 layer of 71.0 ± 3.7 nm, a k_{sp} of 0.009 ± 0.004 ns^{-1} is obtained), one obtains an energy extraction rate of 0.156 ± 0.022 ns^{-1} - an enhancement of 2.1 from the control case above. Upon initial inspection, it appears that this rate is lower than that of the AuNP@605+585 system, however the QD585 donor and QD605 acceptor layers are further from the AuNP surface due to the presence of the purely accepting QD655 layer. This decrease in the extraction rate may be attributed to this larger separation thereby decreasing the influence of the electric field enhancement, subsequently decreasing the non-radiative transfer rates [208]. As a result of this change in environment and 3rd QD influence, it is difficult to draw direct comparisons between the plasmon coupled 2QD- and 3QD-layer systems. Evidently, the addition of the intermediate QD605 layer has a profound effect on the extraction rate from the QD585 given the large difference in the calculated energy transfer/extraction rates between the bilayer and trilayer systems and the virtually negligible calculated transfer rate between QD585 and QD655.

Considering the QD605 layer in the AuNP@3QD system, there is a clear reduction in the measured lifetime from the control to the LSP-coupled case in Fig.

5.16b. The measured lifetime was 17.81 ± 2.95 ns without AuNP and 13.33 ± 1.57 ns with AuNP coupling. Taking the pure QD605 lifetime as a reference, this leads to a measured energy transfer (extraction) rate of 0.023 ± 0.009 ns^{-1} and 0.028 ± 0.011 ns^{-1}, respectively. Again, this considers the expected plasmon decay rate for the respective QD at the same distance from the AuNP centre. This shows that the lifetime of the QD605 in the 3QD-layer system increases compared to QD605+585 (here the QD acts as an acceptor) from 16.68 ns but decreases in lifetime from 23.60 ns compared to QD655+605 (donor). A similar behaviour is also observed in the LSP-coupled 3QD-layer case where the lifetime is shorter in comparison to the purely donor case (AuNP@QD655+605) suggesting the presence of an extra donor accelerates the exciton relaxation. This is an interesting result as, from the calculations, the presence of AuNP does not seem to affect the energy transfer rate of QD605 to QD655 in the trilayer system despite clearly decreasing in the average lifetime.

Finally, in the case of the QD655 acceptor in the trilayer system, the average lifetime does not change significantly in the presence of AuNP. This could be explained as before by the competitive nature of the decay pathways between quenching due to AuNP and exciton donation mainly from QD605 as the local environment does not change significantly after the addition of QD585.

5.4.8 Photophysical dynamics

Let us now investigate and compare the exciton dynamics for each of the QD layer in the 2QD- and 3QD-layer structure. Due to the Purcell effect in the LSP-coupled system, the rate of excitation of the QD layer in the vicinity of a AuNP must be accounted for which is described in the previous chapter by Eq. 2.17. Since the modified PLQY of the QDs in the Au-QD complex and emission rate ratio were found from the experimental values in the previous section, the enhancement factor

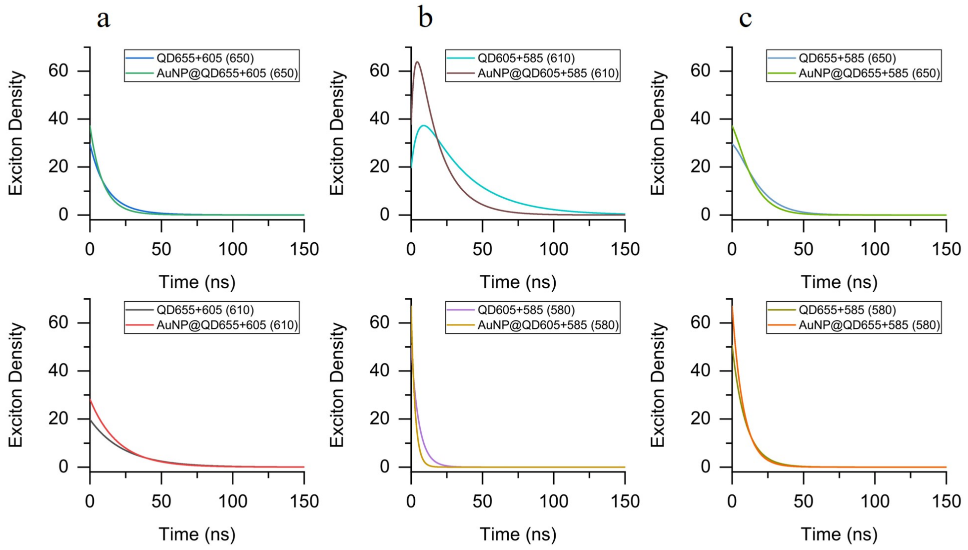

Figure 5.17: Exciton density decay dynamics for a 2-layer QD system comparing with and without plasmonic coupling for (a) QD655+605, (b) QD605+585, and (c) QD655+585. The top row graphs correspond to the exciton density dynamics for the acceptor layer and bottom row for the donor layer.

of the excitation rate ($^{k_{exc}}/_{k^0_{exc}}$ from Eq. 2.17) can be calculated. For a single QD layer separated by a PE spacer from an AuNP, the enhancement of the excitation rates were calculated to be 1.26 ± 0.27, 1.92 ± 0.66, and 1.83 ± 0.14 for QD655, QD605, and QD585, respectively. As k_{sp} is a distance dependent value used in the determination of the modified PLQY and emission rates, these excitation rate enhancements will also vary with increasing separation distances between the AuNP and QDs in the multilayered system. Then, with these values the increase in the initial exciton density, n_i', for each QD layer, i, as a function of particle separation distance from the AuNP surface in the AuNP-QD complex is calculated from the following expression:

$$n_i' = n_i \frac{k_{exc,i}}{k^0_{exc,i}}\,, \tag{5.4}$$

where the 0 superscript refers to the non-LSP coupled QD layer.

From Fig. 5.17, it is evident that in all cases the coupling with a plasmonic

AuNP causes a faster decrease in the exciton density for donors and acceptors alike. This is the expected result given the introduction of the plasmon decay pathway for QDs as well as the modification to the ET rate. Perhaps the more profound difference in the exciton dynamics is in Fig. 5.17b monitoring the exciton density of the acceptor QD605 in the QD605+585 2-layer system. In the control case (without plasmonic coupling), the density reaches a maximum of 37.3 (the units here are arbitrary but can be thought of as the number of excitons per unit area) at roughly 8.8 ns, an increase in density of 88 % from 19.8 at t=0. In the AuNP coupled case, this maximum increased to 63.9 at 4.3 ns leading to an increase in density of 69 % from the same initial density. This is expected given that the ET transfer rate is the dominant process, hence the increase in density after the initial pulsed excitation (at t=0) as well as the steeper rise in the plasmonically coupled system. A somewhat similar (but not as pronounced) behaviour can be seen for the QD655 layer in the QD655+585 system (Fig. 5.17f. In this case, the density does not decrease immediately as is the case for the other QDs.

In the 3-layer case, the exciton density dynamics is shown in Fig. 5.18. If we examine the intermediate QD605 layer, we see that the maximum density reached is 35.2 (a 78 % increase from a density of 19.8 initially) at roughly 7.8 ns, without LSP-coupling. With LSP-coupling this maximum density is increased to 54.7 (94 % increase from the initial density) and reached at 5.0 ns. Although the percentage increase from the initial density to the calculated maximum for the AuNP coupled to the 3QD layer case clearly rises compared to the AuNP coupled to 2QD layer case, the maximum reached decreases. This is attributed to the greater separation between the AuNP surface and the donor QD585 which decreases the influence of the plasmonically enhanced energy transfer rate, as well as the excitation rate of the QDs involved. Briefly examining the QD655 layer, we can see in Fig. 5.19a, the addition of each donating QD layer decreases the curvature of the decay (or

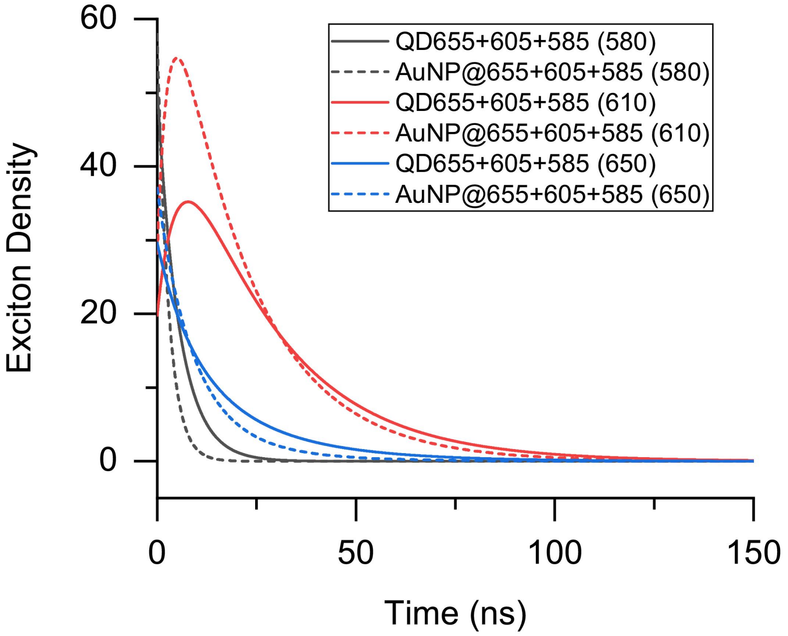

Figure 5.18: Calculated exciton density decay curves for the control QD655+605+585 (solid lines) and AuNP@QD655+605+585 (dashed lines) samples evaluated at the spectral windows indicated in the legend.

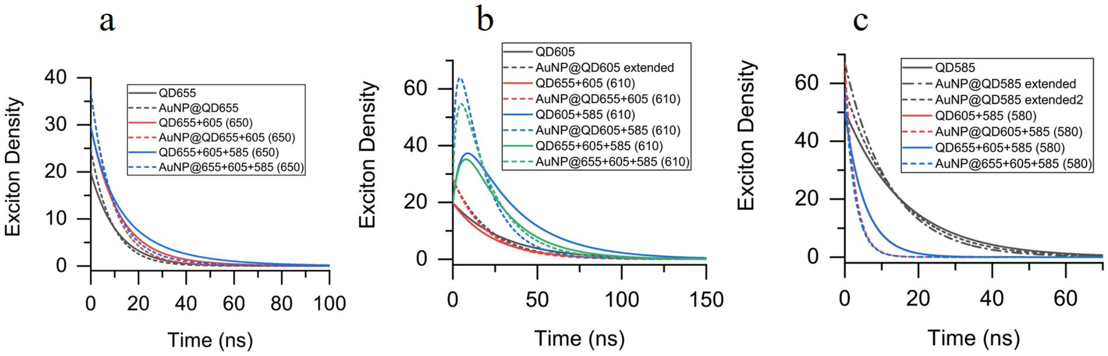

Figure 5.19: Calculated normalized exciton density decay curves for three different QD layer samples for pure QD films (solid lines) and AuNP coupled QD films (short dash lines). The curves are calculated for the density in the (a) QD655, (b) QD605, and (c) QD585 layer. Note that the AuNP@QD605 extended curve in (b) indicates the density dynamics was calculated for an average AuNP-QD605 centre-to-centre distance equal to the average AuNP@QD655+605 centre-to-centre distance. The curves in (c) representing QD655+605+585 and AuNP@QD655+605+585 are, respectively, virtually identical to QD605+585 and AuNP@QD605+585, hence are obscured. The samples denoted as "*AuNP@QD585 extended*" and "*AuNP@QD585 extended 2*" are calculated for an Au-QD separation accounting for a QD605, and QD655 and QD605 in between with any additional PE spacer layers, respectively.

a reduction in the slope is observed) which is characteristic of an excitonic ET. Surprisingly, the change in gradient between QD655 and QD655+605 is smaller than between QD655+605 and QD655+605+585 suggesting a greater ET rate for the latter. This behaviour is copied in the AuNP-coupled density curves although the differences in the slopes are visibly smaller. This similarity may also be explained by the competition between plasmon-coupled ET from the donating layers and the plasmon enhanced decay of QD655. As we have seen previously, the ET rate between QD585 and QD655 is low for extended distances. Therefore, it is possible that the addition of QD585 increases the exciton density in the QD605 layer which, in turn, allows for a greater number of excitons to transfer to the QD655 layer. Furthermore, considering Fig. 5.19c, it is of little surprise that the exciton density profile for QD605+585 and QD655+605+585 are virtually identical and so the ET is mostly due to QD605 - again, suggesting a directed transfer of excitons across the layers. What is interesting to note, however, is the steepening of the decay profile for the QD585 exciton density, with the addition of AuNP, by the same amount for the 2QD- and 3QD-layer system. In the section above, it was suggested that the plasmonic coupling with QD605 at >5 nm separation away from the AuNP surface is weak and so we do not expect a significant plasmonic effect on the energy extraction rate of QD585 due to QD605 at these greater distances. Coupled with the fact that the ET between non-adjacent QD585 and QD655 layers is low, and an increase in the lifetime decay from AuNP@QD605+585 to AuNP@QD655+605+585, it is likely that the QD585 layer is not affected significantly by the addition of the AuNP or QD655 layer.

This is akin to a multi-stage chemical reaction in which the speed of the whole reaction is as fast as the rate limiting step. In this multilayer system, the "rate limiting" step for the transfer of excitons is between the QD605 and QD655 layers. This is evidenced by the large increase in initial exciton density in the QD605 layer but a comparatively minimal change in QD655. As the different decay pathways are competitive, not all excitons will be transferred to the QD655 layer and instead will decay via other pathways e.g. coupling to the far field or non-radiatively dissipating to the environment.

5.4.9 AuNP energy absorption

Given the model prescribed in Eq. 5.1a-5.1c, it is possible to estimate the total number of excitons received by the AuNP, n_{sp}, due to the plasmon coupled decay rates over one excition period (i.e., one pulse). This is found by the following integral,

$$n_{sp} = \sum_i \int_0^\infty n_i k_{sp,i} dt \, , \tag{5.5}$$

where n_i is as before - the exciton density of the i^{th} QD layer. Since the decay pathways are independent, they can be treated separately and used as weights to find the expected density of excitons arriving at the AuNP. Furthermore, one can use Eq. 5.5 to calculate the total energy received by the AuNP *via* the surface plasmon decay route. As these excitons have an energy approximately equal to the emission bandgap of the QDs (ΔE_i), one may calculate the energy contribution to the AuNP from the i-th layer by simply multiplying this bandgap with the number of excitons. Summing the energy contributions for every layer will then yield the total energy absorbed by the AuNP via plasmonic decay, E_{sp}. The bandgap energies were calculated by taking the wavelength of the first absorption peak in Fig. 5.5a and converted to eV, which were 1.94 eV, 2.09 eV, and 2.19 eV for QD655, QD605, and QD585, respectively. Note that the total exciton number is given as a number density, and hence E_{sp} is also, conceptually, an energy density. As expected, with an increasing number of QD layers, the total number of excitons and energy transferred increases due to the extra plasmonic and energy transfer decay pathways

Sample	n_{sp}	E_{sp} (eV)
AuNP@QD655	5.02	9.74
AuNP@QD655+605	15.71	31.64
AuNP@QD655+605+585	30.67	62.93

Table 5.8: Calculated exciton number density, n_{sp}, and total plasmon decay energy, E_{sp}, transferred to the AuNP by the exciton-plasmon coupling decay using the surface plasmon decay rates, k_{sp} obtained experimentally. The values of the QD bandgap energies used were 1.94 eV, 2.09 eV, and 2.19 eV for QD655, QD605, and QD585, respectively.

contributing to the increase in excitons in the acceptor QD layers. There appears to be a tripling of the number of excitons transferred to the AuNP from 1 to 2 QD layers, and a doubling from 2 to 3 QD layers – a relationship also reflected by the total energy. For this structure, it is not expected for excitons to be quenched via recombination before reaching the AuNPs or the next QD layer. As the exciton diffusion length is of the order of 10-20 nm in length within a layer, it may be possible to increase the QD density and layer thickness before one begins to observe a degradation in the exciton multiplication with subsequent additions of QD layers [209]. This is, of course, if the plasmon decy rate remains sufficiently faster than other decay pathways to ensure the transfer is dominant. Furthermore, this behaviour is only expected to be possible with a structured formation of QDs such that the excitons energy is spatially funnelled towards the AuNP (or some other centre). For a randomly distributed set of QDs, the energy transfer no longer becomes directed, and hence a lower density of excitons will be concentrated at QD layers close to the AuNP surface, which limits its effectiveness as an energy harvester.

5.5 Conclusion

It has been shown through time-resolved PL spectroscopy the energy transfer dynamics of excitons across a plasmon coupled multi-layered QD films fabricated by a LbL approach. The lifetime of the purely accepting QD655 layer in direct proximity to the AuNP presents insignificant changes due to the competition between excitonic relaxation from the LSP-exciton coupling and energy transfer from the immediate donating layer. It can also be seen that the ET contributions from non-adjacent QDs fall to negligible levels compared to the ET rate of adjacent layers owing to the rapid decrease in the FRET-life coupling strength. As the QD585 is far away from the AuNP in the 3-layer system, the plasmonic coupling no longer becomes significant and so an increase in the lifetime is seen as compared to the 2-layer system. Furthermore, the presence of this donor appears to accelerate the excitonic relaxation of the intermediate QD605 in the 3-layer system through the photophysical calculations after an initial excitation.

Despite a reduction in lifetimes, the calculations show that the LSP-coupled FRET rate does not change significantly compared to the non-plasmonic system other than between QD605+585 if they remain near the surface of the gold. It has been suggested that the transfer of excitons between the layers is similar in concept to a rate limiting step for chemical reactions. High ET rates between the QD585 and QD605 will inevitably cause an increase in the exciton density for the acceptor layer. However, if the ET rate to the QD655 layer remains low, compared to the intrinsic or plasmon decay rates, minimal changes in the exciton density will be observed and excitons will instead decay via other pathways. Therefore, not only should the energy bands of the QDs be considered when constructing multi-species, multi-layered QDs, the decay rates must also be accounted for to optimize the probability for excitons to be transferred across the layers. The use of plasmonic coupling must also be thoughtful to ensure enhancement of any energy transfer/extraction pathways that can be considered "rate limiting" in the overall system i.e., enhancing the slowest energy transfer processes.

Finally, the total energy transferred to the AuNP was estimated by using the model provided in the section above (Eq. 5.5) where it was found that the energy

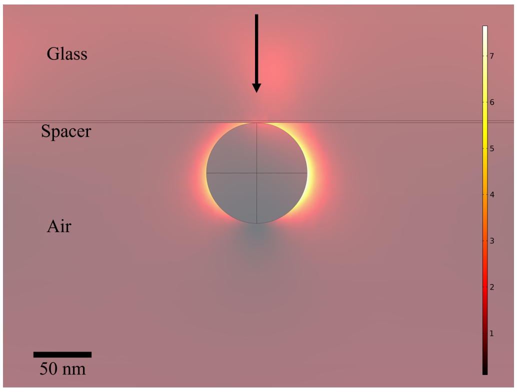

Figure 5.20: COMSOL Multiphysics simulation (using the Radio Frequency module) of the electric field enhancement ($|E/E_0|$) around a AuNP of diameter 87 nm on a 1 nm thick spacer layer and glass substrate. The arrow indicates the direction and angle of illumination by a 470 nm plane wave source at normal incidence.

received over a decay period is enhanced by a factor of 6, from 1 to 3 QD layers. Thus, this structure serves as an energy harvester in which the energy transferred to a plasmonic system can be increased due to the enhancement of energy transfer rates and spatially directed transfer of excitons - effectively increasing the absorption cross section of the AuNP. Such a conclusion is echoed by Carretero-Palacios *et al.* in which the authors demonstrated an increase in absorption of noble metal nanoparticle doped perovskite films for the purposes of solar harvesting [210]. This clearly has implications for energy harvesting devices which may exploit such properties of directed energy transfer for uses that include solar cells and purification systems.

Although the coupling between QDs and plasmons are observed experimentally, it is likely a layered structure is not particularly optimal to exploit the field enhancement of AuNPs. As seen in Fig. 5.20, most of the field enhancement is localized to the lateral regions of the AuNP and at the space between the AuNP and substrate surface. It is surmised that the QDs reside mostly on the top half around the AuNP (furthest side from the substrate surface) and so do not experience as strong of a field enhancement. Therefore, it is logical to explore alternative arrangements between

AuNPs and QDs that allow QDs to exploit these intense field enhancements.

Chapter 6

Colloidal Nanoparticle Encapsulation

6.1 Introduction

In the previous chapter, the excitonic energy transfer processes were investigated for AuNP-coupled QD films on glass substrates. As the QDs and AuNPs were fixed on a substrate, it was shown to be unlikely that the electric field enhancements were in regions where the QDs could reach and that the dipole moments relative orientation for the two nanoparticles were likely fixed. To overcome this, the use of strong binding ligands (such as Biotin-Streptavidin) and electrostatic attraction forces can be used to surround a central AuNP with QDs such that the relative placement and dipole orientations are random. This increases the likelihood that QDs reside in a region of electric field enhancement, thus imporving the energy transfer rates between NPs.

The binding of Biotin (BTN) and Streptavidin (STV) is well-known for its high affinity and specificity, and has been utilised previously as a ligand for surface functionalization of Gold and Silver nanoparticles [211, 212]. Therefore, Biotin that is thiolated (with a sulfur end group of the form -SH) is often used due to the high affinity of sulfur groups to noble metals [213] and is exploited to fabricate Biotin functionalized AuNPs. An advantage to this method is the relative ease in which fluorescent probes (such as dyes or QDs) can also be functionalized with either the Streptavidin protein or Biotin. This allows one to construct concentric multilayers of QDs around a central AuNP using alternating Streptavidin/Biotin ligands. A disadvantage to this method, however, is the lack of flexibility in the separation distances between the AuNP and the concentric layers. This distance is usually limited to the length of a polymer that is terminated by a thiol group and Biotin on either end, such as polyethylene glycol (PEG).

An alternative method to conjugate QDs explored in this chapter is to use the fact that CTAB capped AuNP are positively charged and can be further encapsulated by PE layers, in a similar way to the films constructed in chapter 5. The use of alternating positively and negatively charged PEs on AuNPs allows one to customize the separation distances between nanoparticles by varying the number of layers used. However, although simple in practice, high yield samples are often difficult to achieve for a greater number of PE layers due to the washing steps required in between the layers which may incur considerable losses per wash and in total. The increased thickness also means a decrease in plasmonic sensitivity and effectiveness of the increase in electric field enhancement due to the larger separation from the metal surface [214].

Either method aims to overcome the issue of scalability inherent in typical top-down approaches (such as Electron Beam Lithography, as discussed in chapter 4). To fabricate large scale, 2-D structures require long write and development times, on top of various other post-processing requirements to fully functionalise a surface. Therefore, it becomes impractical for large scale production of such samples required for manufacturing using these traditional lithographic techniques. With chemical based methods, one solves the issue of limited scalability by essentially converting linear writing (i.e., EBL) into a parallel self-assembly process. In doing so, one trades nanometric control of structured assembly with throughput. In this chapter, the viability and performance of such liquid based samples will be explored by investigating the fluorescence energy transfer rates of QDs that are coupled to plasmonic gold nanoparticles.

6.2 Methods

The AuNP used here were the in-house made nanoparticles described in chapter 3. Three methods to conjugate QDs to the surface of AuNP in solution were attempted and are referred to as ethanolic, reduction, and electrostatic - the first two involving the Biotinylation of the AuNP.

In this study, SH-PEG-Biotin (M_w =1000 g mol^{-1}) was used for the ligand exchange process for AuNP Biotinylation. Dyes used here for comparison were Alexa Fluor 633 Carboxylic Acid (AF633) and Streptavidin Alexa Fluor 633 conjugate (AF633STV), both purchased from Thermo Fisher Scientific. Furthermore, the QDs used were QDot 655 Streptavidin conjugate (QD655STV), QDot 605 Biotin conjugate (QD605BTN), and QDot 585 Streptavidin conjugate (QD585STV) obtained from Thermo Fisher Scientific.

6.2.1 Ethanolic Displacement

Firstly, the method of ethanolic displacement is based off of the work conducted by Kinnear et. al. [215]. Here, ethanol is added with the biotinylated linker molecule to the as-made AuNP solution and left for a long period of time to slowly displace the CTAB bilayer. The as-made AuNP solution was centrifuged at 6000 rpm for 15 mins where the supernatant was discarded and the pellet was dispersed into a 90% ethanol solution. During this centrifugation, a stock solution of SH-PEG-Biotin was diluted to 1 mg/mL (90% ethanol). Subsequently, 200 μL of diluted SH-PEG-Biotin was added to the ethanolic AuNP solution and left to stir on the orbital shaker at 100 rpm for 24 h. After this period, the solution was centrifuged at 6000 rpm for 15 mins, the supernatant was discarded and the pellet dispersed in water.

6.2.2 Reduction Replacement

An alternative method for the removal of CTAB and subsequent replacement with SH-PEG-Biotin molecules is to use Sodium Borohydride ($NaBH_4$). It is a strong reducing agent that is often used in chemical reactions [216] such as in the fabrication process of AuNPs here. An attractive property of using $NaBH_4$ is its effectiveness of removing CTAB from the Au surface compared with various other complex methods [217] and stability of AuNP during the CTAB removal process [218, 219].

Since $NaBH_4$ is a strong reducing agent (as it decomposes to form a hydride ion which eventually forms H_2 when left in water for too long), a solution must be freshly made every time it is required. To 1 mL of as-made, CTAB-capped AuNP, 200 μL of 50 mM $NaBH_4$ was added and vigorously stirred for approximately 1 min. As the CTAB is removed, it is free in solution and has the potential for readsorption onto the Au surface. Therefore, 200 μL (1 mg/mL in 90% ethanol) SH-PEG-Biotin was added to quickly bind competitively to the Au surface to prevent CTAB binding again. This solution was left undisturbed for 24 h which was centrifuged at 6000 rpm for 15 mins with the pellet dispersed in water to remove the excess SH-PEG-Biotin and CTAB.

6.2.3 Dye and QD conjugation

As an initial test, Streptavidin conjugated dyes were used to attach to the Biotinylated AuNP (AuNP@BTN) as they are smaller than QDs, they are more likely to remain attached to the surface during centrifugation and can act as a reference. First, the dyes were prepared by dispersing a small amount of powder into deionized

(DI) H_2O and diluting these solutions to 1 μM concentration each. The initial concentration was determined by UVVis spectroscopy and using Eq. 3.1 with the molar extinction coefficient (ε_λ) at the absorption peak supplied by the manufacturer. The molar extinction coefficients (absorption peak wavelength) are 168000 $M^{-1}cm^{-1}$ (620 nm) and 138000 $M^{-1}cm^{-1}$ (636 nm) for AF633 and AF633STV, respectively. Second, 200 μL dye solution (1 μM) was added to 400 μL AuNP@BTN and left to incubate for 45 mins. Afterwards, the mixture was centrifuged at 6000 rpm for 15 mins and the pellet was subsequently dispersed in 400 μL H_2O.

6.2.4 Colloidal LbL

Instead of CTAB removal, this method aims to entirely passivate the CTAB surface by encapsulation with oppositely charged PE layers. This method is similar in principle to that described in chapter 5 and has proved successful, especially in biomedical applications, utilising LbL assembly of PE films on colloidal NPs [220–222]. We exploit the fact that CTAB-capped AuNPs are positively charged, thus anionic polymers are electrostatically bound to the AuNP surface, reversing the Zeta potential. This may be repeated multiple times to achieve varying thicknesses as required and with the desired charge, illustrated by Fig. 6.1.

To 1 mL of as-made AuNP@CTAB, 200 μL of PSS (2 mg/mL H_2O) was added and vigorously stirred for a few seconds before being left undisturbed for 5 mins. The mixture was then centrifuged at 6000 rpm for 10 mins once, with the supernatant discarded and pellet resuspended in water. The procedure was then repeated with PolyDADMAC (2 wt. % H_2O) to which this PSS-PolyDADMAC layer will be referred to as a bilayer (BL).

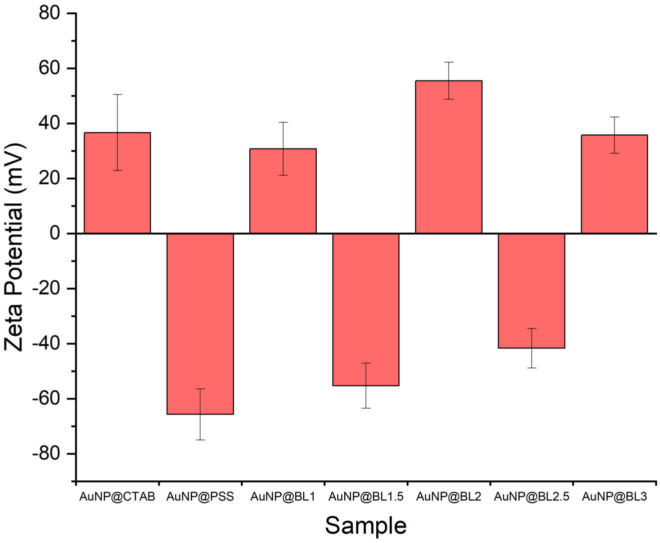

Figure 6.1: Zeta potential of AuNP in solution with successive coatings of alternating PE layers up to 3 bilayers (BL) of PSS and polyDADMAC. The samples denoted with integer BL values have a final coating with polyDADMAC and half-integer values are finished with a PSS layer.

6.2.5 Electrostatic QD attachment

The carboxylated QDs have been measured to have a Zeta potential of -26.9 ± 4.2 mV, -15.7 ± 2.0 mV, and -36.1 ± 2.7 mV for QD585, QD605, and QD655, respectively, at neutral pH. Therefore, these QDs are susceptible to electrostatic attraction to positively charged AuNPs capped with an outer layer of polyDADMAC. Here, a bilayer (BL) of PSS/polyDADMAC is used to encapsulate the AuNPs (AuNP@BL) before QD attachment both to minimize losses during the centrifugation procedures and to simulate closely the conditions of the QD films as discussed in chapter 5.

To perform the attachment, 200 μL of QDs diluted to approximately 3.2 nM was added to 1 mL of AuNP@BL and left for 1 h after which the mixture was centrifuged at 6000 rpm for 10 mins. The supernatant was discarded and the pellet dispersed back in 1 mL water before immediately adding 200 μL polyDADMAC for 5 mins to encapsulate the QDs. Centrifugation was repeated as before and the pellet suspended in 1 mL H_2O. To add extra layers of QDs, the polyDADMAC covered colloidal heterostructures were first capped with an extra layer of PSS and subsequently polyDADMAC in an identical way as before with 200 μL, left for 5 mins, and centrifuged out creating a triple PE layer. The following QD solution was then added as before.

6.3 Results and discussion

6.3.1 AuNP Biotinylation

To evaluate the degree of success of Biotinylation of AuNP (AuNP@BTN), the use of UVVis, DLS and Zeta potential measurements have been employed to measure the changes in the optical and physical morphology of the AuNP. As discussed in chapter 2.2, plasmonic systems are sensitive to changes in the near field, therefore one would expect differences in the UVVis spectra between AuNPs capped with either CTAB or PEGylated Biotin. Indeed, we observe this difference as shown in Fig.6.2a where the absorption peak of the AuNP appears to split with one peak redshifting likely due to slight aggregation. In addition, the measured DLS of the sample in Fig.6.2 has no indication of any significant aggregation of the NPs, and reports a Z-average diameter of 150.6 ± 4.4 nm with an average PDI of 0.23 ± 0.03 and 151.3 ± 3.1 nm with a PDI of 0.24 ± 0.01 for AuNP@BTNs fabricated by EtOH and $NaBH_4$, respectively (up from 128.6 ± 2.5 nm with a PDI of 0.05 ± 0.01 for this particular AuNP batch). Therefore, this equates to a PEG capping thickness of 11.2 ± 1.6 nm suggesting that the PEG molecule at the molecular weight exhibits a random coiling conformation [223].

Finally, by measuring the Zeta potential it was found that the surface charge of the AuNP@BTN was -16.7 ± 4.6 mV - a significant decrease from +36.6 ± 13.8

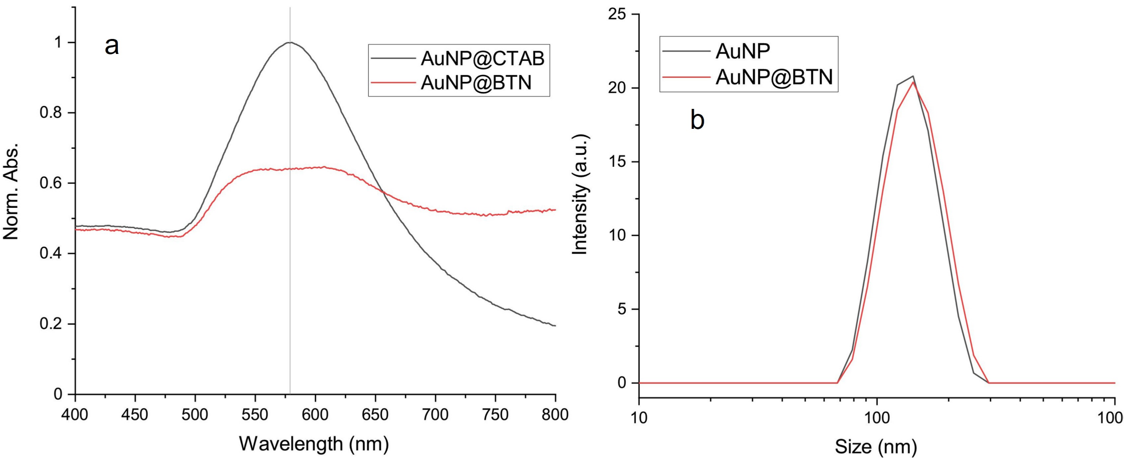

Figure 6.2: (a) Comparison of UVVis absorption spectra of as-made AuNP capped with CTAB and Biotinylated AuNP by $NaBH_4$ reduction. The vertical reference line denotes the AuNP@CTAB LSPR peak at 580 nm. (b) DLS size measurements of the two AuNP samples.

mV in the as-made AuNP solution. In light of this information, it is clear that the surface chemistry of the AuNPs have changed, with little aggregation, most likely due to the addition of PEGylated Biotin molecules.

6.3.2 Fluorescent dye conjugation

The Biotinylated AuNPs were, first, loaded with fluorescent dyes conjugated with the complimentary Streptavidin molecule to evaluate the efficacy of dye loading onto the AuNP surface without damage to the surface ligands from centrifugation. Once the method had been established, the AuNPs were then reacted with multilayers of conjugated QDs. The dyes were used first due to their low weight which, after centrifugation, is less likely to cause significant damage to the AuNP surface ligands. In order to determine the binding of dye molecules onto the surface of gold nanoparticles the absorption, time-resolved, and steady-state PL emission spectra were obtained and any changes were identified.

These measurements are illustrated in Fig. 6.3. Although the UVVis (Fig. 6.3b and 6.3e) spectra do not immediately indicate the presence of dyes in the system, the

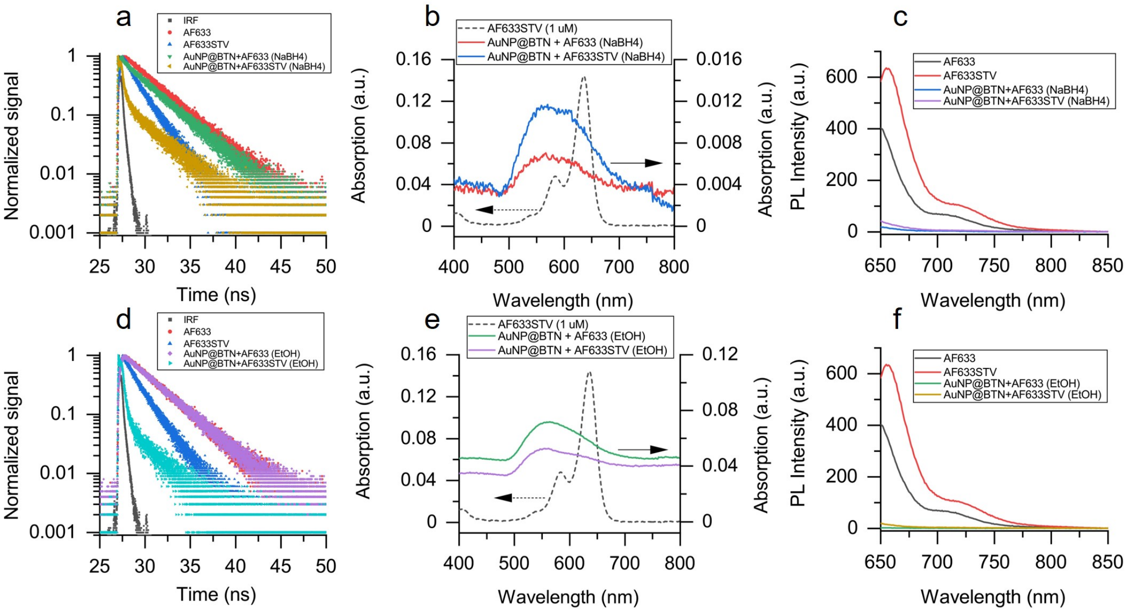

Figure 6.3: (a) Lifetime decay curves, (b) UVVis and (c) PL emission spectra of AuNP@BTN fabricated by $NaBH_4$ reduction. (d-f) Corresponding graphs of AuNP@BTN fabricated by ethanolic displacement. Both left and right axes of the UVVis spectra are shifted relative to each other for clarity.

emission signature is clearly seen in the steady-state PL emission spectra (Fig. 6.3c and 6.3f) and lifetime decay curves (Fig. 6.3a and 6.3d). Comparing the PL spectra clearly shows the significant decrease in emission peak from the pure AF dyes to the conjugated system. As centrifugation separates constituent components of a fluid based on differences in mass, it is expected that the majority of unbound dyes would be removed during the washing and recovery of AuNPs. Hence, it is unsurprising that the emission profile of the control AF633 dye decreases significantly (which virtually disappears in the EtOH sample) and in both samples there exists a small emission signature. However, one cannot completely attribute this reduction in peak amplitude to plasmonic quenching alone due to the possibility of contributions from dye molecules that have not been totally removed from the solution. This could also be explained in part by the reduction in dye concentration after centrifugation. A control nanoparticle similar in size and morphology, functionalized with Biotin, and does not present any plasmonic behaviour (e.g., Polystyrene beads) would be needed for a more confident conclusion of dye attachment by observing the changes in PL alone. Therefore, changes in the lifetime of the conjugated system would be a better indication of any chemical or electronic change in the dyes as opposed to steady-state PL.

Firstly, the lifetimes of the dyes were found to be 3.27 ± 0.01 ns and 1.78 ± 0.05 ns for the AF633 and AF633STV probes, respectively. The lifetime obtained for AF633 matches very closely to those obtained in previous works and in reference tables validating the use of the fitting methods described in the previous chapters [224, 225]. As shown in Fig. 6.3a and 6.3d, the lifetimes of the control samples (unmodified AuNPs) remain unchanged indicating that the dyes which are present in the solution are unbound to the AuNP. Conversely, there is a noticeable change in lifetime for the Streptavidin-Biotin conjugated system yielding an amplitude averaged lifetime of approximately 0.64 ns and 0.37 ns for the $NaBH_4$ and EtOH samples, respectively. This average was obtained from the extracted lifetimes (amplitudes): 0.20 ns (0.86) and 3.48 ns (0.14) for $NaBH_4$, and 0.19 ns (0.92) and 3.60 ns (0.08) for EtOH. Clearly, the presence of a small emission signature in the PL spectra alongside the drastic reduction in the average and short component lifetimes indicate the successful binding of AF dyes onto the surface of AuNPs when compared to the lack of lifetime changes in the control sample. This further suggests that the reduction in PL peak can also be partly explained by plasmonic quenching of the dyes.

6.3.3 QD conjugation

To begin with, we follow a similar analytical path as in the previous chapter whereby we first identify the relevant energy transfer parameters (such as R_0 and the transfer rates) then compare these values against the LSP-coupled system. As before, to find the FRET radii of the different pairs of QDs one must first measure the

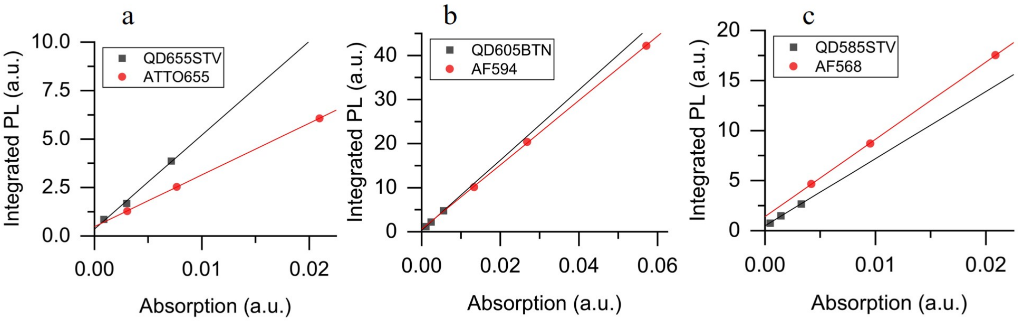

Figure 6.4: Absorption vs integrated PL QY graphs of bioconjugated QDs compared against their reference dyes for (a) QD655STV, (b) QD605BTN, and (c) QD585STV.

PLQYs of the QDs. These were found to be 0.54 ± 0.04, 0.72 ± 0.01, and 0.60 ± 0.03 for QD655STV, QD605BTN, and QD585STV, respectively. The absorption vs integrated PL graphs used in the determination of the PLQY are shown in Fig. 6.4.

As the nanoparticles are functionalized by relatively small biological molecules/proteins that have been found to have very similar refractive indices as water [226], and are suspended in water, the medium refractive index is taken to be 1.33. The orientation factor is also taken to be $\kappa^2 = 2/3$ like before as in solution the QD transition dipoles are expected to be randomly oriented relative to each other. With these parameters, the FRET radii can be found for each QD pair and are summarized in Table 6.1. Without the intermediate QD605BTN, it is not expected for the other two STV conjugated QDs to bind to each other, but the FRET radii will nevertheless be useful in determining the QD distances in a shelled structure using the energy transfer efficiency. First, the lifetimes of the control solution were measured, which can be seen in Fig. 6.5. Fitting a decay model to these curves and extracting the

QD pair (Donor+Acceptor)	Φ_D	J $(nm^4M^{-1}cm^{-1})$	R_0 (nm)
QD605BTN+QD655STV	0.72 ± 0.01	1.31×10^{17}	10.99 ± 0.02
QD585STV+QD605BTN	0.60 ± 0.03	3.08×10^{16}	8.37 ± 0.07
QD585STV+QD655STV	0.60 ± 0.03	1.27×10^{17}	10.60 ± 0.09

Table 6.1: Summary of the FRET parameters for the 3 QD pairs with the donor quantum yield, Φ_D, spectral overlap, J, and Förster radii, R_0, as obtained using Eq. 2.4.

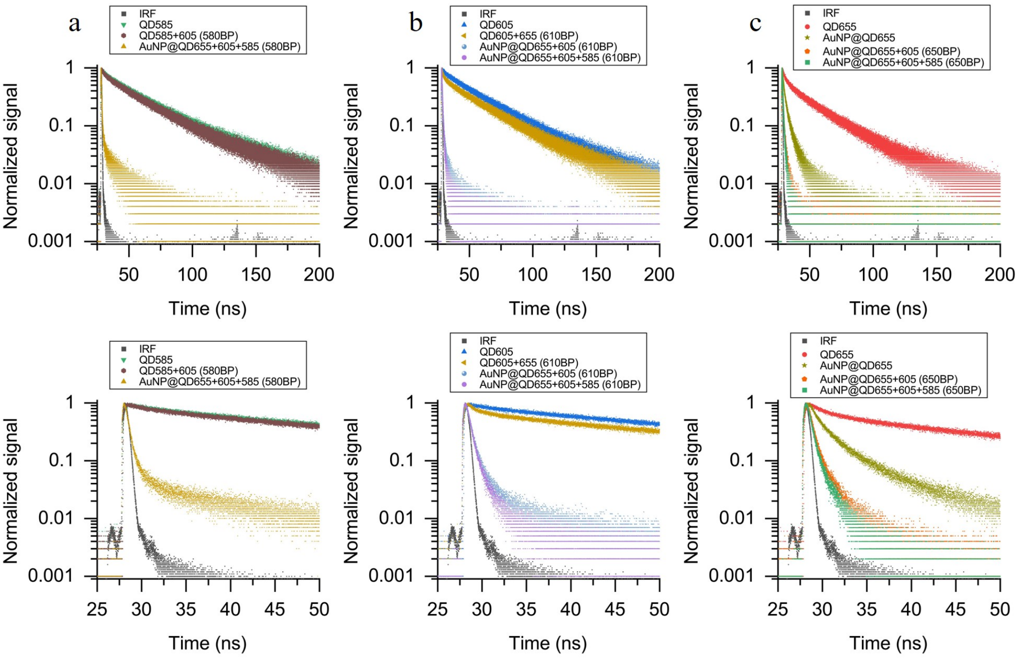

Figure 6.5: Lifetime decay curves of the AuNP@QD mixture in solution measured at (a) 585 nm, (b) 605 nm, and (c) 655 nm. The bottom row corresponds to a zoomed section between 25 - 50 ns of the top row.

lifetime, one obtains, for QD655STV, QD605BTN, and QD585STV, 19.09 ± 0.44 ns, 30.44 ± 0.07 ns, and 30.21 ± 0.35 ns, respectively. Then, pairs of the QDs were mixed together in solution (e.g., QD605BTN and QD655STV) and the fluorescence lifetime measured at the donor wavelength. The average lifetimes obtained for the pairs were 22.74 ± 0.29 ns for QD605+605, and 28.26 ± 0.07 ns for QD585+605. Here in the naming convention, the conjugated molecules are implied and hence omitted. Thus, taking these lifetime values, the energy transfer efficiency can be calculated using $E = 1 - {}^{\tau_{DA}}/_{\tau_D}$, recalling from Eq. 2.10b. For QD605+655, the FRET efficiency was calculated to be 0.253 ± 0.003, and for QD585+605 this was 0.065 ± 0.001. Finally, with the transfer efficiency and R_0 obtained, the centre-to-centre distance, d, can be calculated by Eq. 2.9. For QD605+655, d was 13.2 ± 0.1 nm, and with QD585+605 this was 13.1 ± 0.1 nm, which given the QD sizes is expected. As a quick check, the size of the Streptavidin molecule can be calculated for the two pairs and an average found between them to verify the validity of the model, much like in the previous chapter. Assuming the core/shell radii of the QDs are the same sizes as in the previous chapter, the average Streptavidin molecule size calculated was 5.4 ± 0.6 nm. This agrees well with the literature in which previous studies have quoted a size of roughly 5 nm [227, 228].

Given the calculated size of the Streptavidin, the expected centre-to-centre distance between QD655STV and QD585STV as if separated by QD605BTN can be calculated. Then, using the diameters given above, this extended distance was found to be 26.2 ± 2.1 nm. As the FRET radius for the QD585-655 pair was found above with a reasonable level of uncertainty, the extended distance can be used to find the theoretical energy transfer efficiency. Using Eq. 2.9, the efficiency at this distance was only 0.004 ± 0.002 - an order magnitude smaller than for the QD585-605 pair. Therefore, the energy transfer rate between QD585 and QD655 is virtually negligible similar to the film structure.

6.3.3.1 AuNP to single QD

Turning our attention now to the conjugated AuNP case, it can already be seen by simple inspection of Fig. 6.5 that the lifetime of a single layer of QD655 changes dramatically. The amplitude average lifetime obtained after fitting was 2.22 ± 0.29 ns which yields an LSP-coupled decay rate, k_{sp}, of 0.399 ± 0.059 ns^{-1}. This value is far greater than what is achieved in the film based structure by a factor of 17.3. A possible explanation for this is the fact that in the film based structure, the local field enhancement is not uniform around the AuNP. In the previous configuration, the nanoparticles are fixed in space and illuminated at approximately normal incidence. Therefore, the majority of the field enhancement will be localised to the lateral regions of the AuNP that are unlikely to affect the QDs due to being impeded by the polymer spacer. However, in a suspension, the attachment of QDs on the AuNP

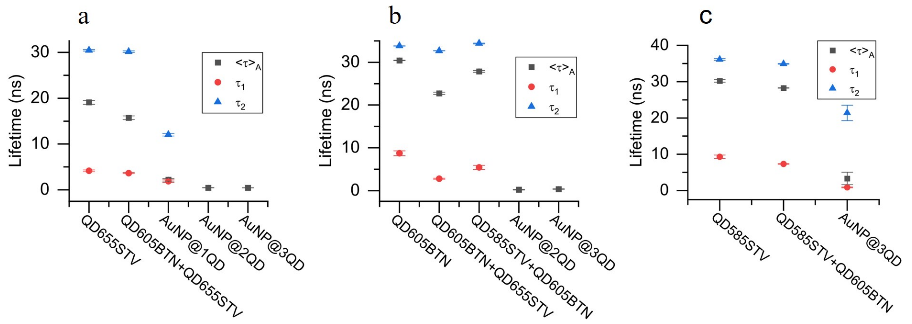

Figure 6.6: Lifetime decay components of the AuNP@QD multishell structure measured at the wavelengths (a) 655 nm, (b) 605 nm, and (c) 585 nm. The label AuNP@nQD indicates the number of QD shells, n, around the central AuNP, starting with QD655, and then subsequently with QD605, and QD585.

surface and orientation of the dipole moments are random and thus, it is far more likely for a QD to be in a region of enhancement from the AuNP. This also means that the dipole orientation factor, $\kappa^2 = 2/3$ is a more valid assumption under this QD encapsulation configuration.

It is also worth noting that large AuNPs can be approximated as a plane metal surface for QDs close to the AuNP (relative to the AuNP size, D, i.e. distance $\ll$ D) [229]. The treatment for QDs coupled to surface plasmons from Au film is the same as what has been presented in this thesis. In fact, Okamoto *et al.* has shown a Purcell enhancement of 2 for CdSe QDs coupled to Au films relative to QDs on quartz substrates [230]. Taking a similar approach, the Purcell factor, F_P, of LSP-coupled QD samples were calculated to be 8.62 ± 1.14, using Eq. 2.20.

6.3.3.2 Multi-shell QD structure

With the addition of subsequent QD donor layers, the lifetimes components of the decay were extracted. These values are plotted in Fig. 6.6 for each constituent wavelength. Briefly beginning with QD655, the conjugation of subsequent QD donors reduces the measured lifetime to 0.44 ± 0.02 ns with both QD605 alone and QD605+585. Furthermore, the lifetime reduces to a single component for these structures although, it is quite clear that fast plasmonic decay is dominant in this process. This is evidenced by the fact that the fast decay amplitude is much larger at 0.97 (1.88 ± 0.28 ns) compared with 0.03 (12.03 ± 0.29 ns) for the slow component for the AuNP@655 structure. Therefore, even large plasmonic enhancements of the energy transfer rate to QD655 is not expected to exceed the plasmonic decay rate.

Sample	k_{ET} ns^{-1}
QD605+655 (610)	0.011 ± 0.001
QD585+605 (580)	0.0023 ± 0.0004
QD605+655@AuNP (610)	4.816 ± 1.550
QD585+605+655@AuNP (610)	2.779 ± 0.538
QD585+605+655@AuNP (580)	0.268 ± 0.156

Table 6.2: Energy transfer rates for the 2 and 3 QD conjugated structures comparing the control and LSP-coupled samples. The lifetimes used to calcualte the rates are measured at either 580 nm or 610 nm, as indicated in the parentheses. Note that for the LSP-coupled samples, the calculated rates include the surface plasmon decay rate, k_{sp}.

Considering now the intermediate QD605, due to its spatial and spectral position, it can act both as a donor and acceptor. As a donor in the presence of AuNP (the sample denoted as AuNP@QD655+605), the lifetime suddenly reduces dramatically to a single component of 0.21 ± 0.07 ns. This is to be expected as the presence of the AuNP not only quenches the QD but enhances the LSP-coupled FRET rate. It was found that the combined FRET and surface plasmon decay rate increases to 4.816 ± 1.550 ns^{-1} (see Table 6.2 for a summary of the calculated ET rates). In comparison to the control system, without LSP-coupling, this equates to an enhancement of around 438 times! This obtained energy transfer rate, however, incorporates the plasmon decay rate of the QD605 layer which one cannot completely ignore. Much like with QD655, it is likely that QD605 is within the electric field enhancement region and strongly couples with the plasmon mode. This therefore complicates the calculations and would require careful construction of QDs around plasmonic nanoparticles with known distances to separate plasmon and FRET decay effects. In spite of this, if one were to assume k_{sp} for QD605 is of the same magnitude as in the QD655 case (at the same distance to the AuNP), the ET rate will still be an order of magnitude greater. This is especially true when accounting for an extended distance between the AuNP surface and QD605. With three QD shells around a central AuNP, there appears to be a slight increase in the lifetime of QD605 to 0.36 ± 0.07 ns. Taking the calculated k_{ET} of 2.779 ± 0.538 ns^{-1}, this amounts to a reduction in enhancement down to 253 times. This seems to be in line with what was detected in the film case where the presence of a donating layer increases the exciton density of the QD605 layer, thus increasing the apparent lifetime and subsequently appearing to reduce the energy transfer efficiency.

Finally, analysing the decay of QD585 we must naturally consider the AuNP shelled with 3 layers of QDs. Much like in the previous chapter, let's first consider the theoretical energy transfer efficiency between QD585 and QD655. Assuming the same core/shell radii as in the previous chapter, the theoretical distance between the STV conjugated QDs was 26.24 ± 2.13 nm, accounting for an intermediate QD605 joined by STV. Using this distance and the FRET radius from Table 6.1, the theoretical transfer efficiency for the two QDs was calculated to be 0.004 ± 0.002. This is very similar to the efficiency of the film based structure between the two QDs at this extended distance. Therefore, the energy transfer between non-adjacent QDs can, again, be discounted in the calculations as it is virtually negligible.

As discussed earlier, the lifetime of the QD585 layer changes only slightly in the control case considering only the energy transfer to QD605 (Fig. 6.6c). This is in comparison to the addition of AuNP where the average lifetime is reduced to 3.32 ± 1.71 ns. From these lifetimes, the energy extraction rate for the QD585 layer (Table 6.2) for the QD585+605+655@AuNP sample (0.286 ± 0.156 ns^{-1}) compared to the QD585+605 control sample (0.0023 ± 0.0004 ns^{-1}) was found to be enhanced by 116 times! Similar to the QD605 layer, the plasmonic decay rate of the QD585 layer is

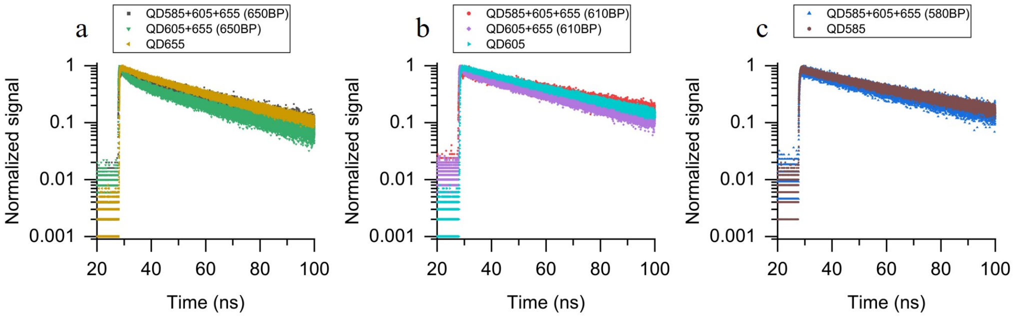

Figure 6.7: Lifetime decay curves of different mixtures of QDs in solution measured at (a) 655 nm, (b) 605 nm, and (c) 585 nm.

still incorporated into the obtained extraction rate for the LSP-coupled system. It remains a challenge to disentangle the two rates to obtain a pure energy transfer rate to the QD605 layer (assuming it is negligible to the QD655 layer).

6.3.4 Electrostatic attachment

Although the conjugated system is simple in terms of fabrication procedure from the strong affinity of Streptavidin to Biotin, it fails to be readily customizable. Unless linker molecules with known lengths, conformations, and are doubly terminated with either Biotin or Streptavidin, it is difficult to vary the centre-to-centre distances between nanoparticles. A work around is to forego the use of the Streptavidin and Biotin and instead revert back to the carboxyl QDs. As seen in the previous sections, the QDs are bound to AuNPs via electrostatic attraction with the centre-to-centre distance varied by the number of PE layers used. Unfortunately, this process was limited to using 3 PE layers between each constituent layer (polyDADMAC/PSS/polyDADMAC). This was due to the losses incurred during each washing stage. As centrifugation was necessary between each addition of PE and QD layer, the number of washes were numerous and therefore losses were high overall. The lifetimes of the control mixtures (no AuNP present) were first measured as a baseline without the use of PE layers. From Fig. 6.7, the unbound QD

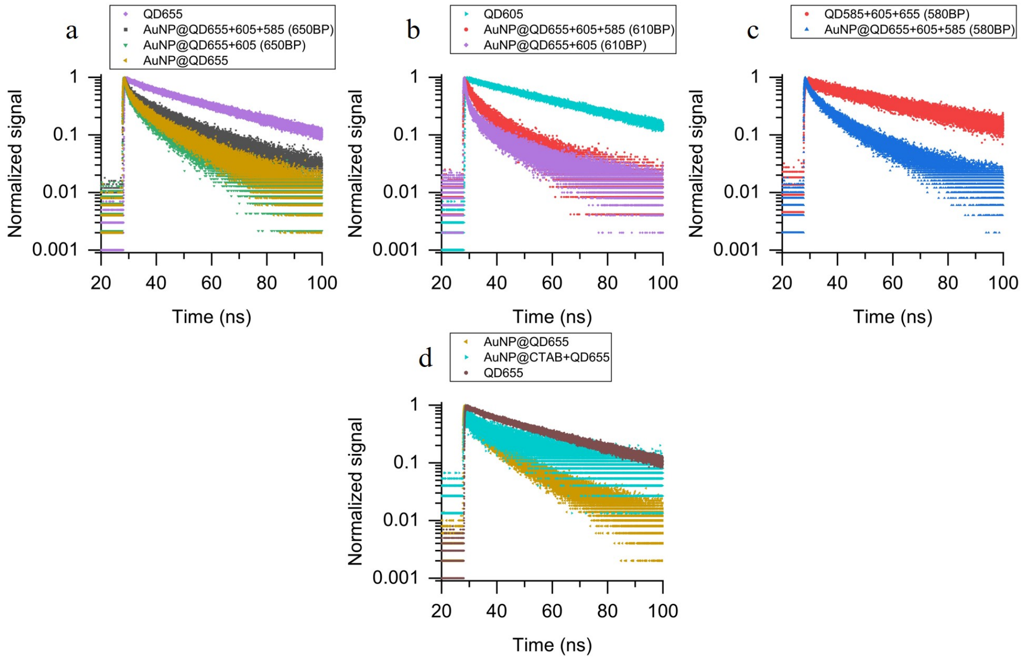

Figure 6.8: Lifetime decay curves of colloidal LbL in solution for different mixtures of QDs measured at (a) 655 nm, (b) 605 nm, and (c) 585 nm. (d) Comparison of the lifetime decay curves for AuNP@QD655 with and without PE layers (denoted as AuNP@CTAB).

mixtures do not appear to affect the measured lifetimes at each of the QD emission wavelengths. This is in comparison to the LbL encapsulation samples by electrostatic attachment seen in Fig. 6.8. In all cases, a reduction in the lifetime can be seen in the presence of AuNP - greater than the QD mixtures alone. As before, the lifetimes are extracted using the iterative reconvolution algorithm and are plotted in Fig. 6.9.

Firstly, the as-made AuNPs (AuNP@CTAB) were conjugated with the negatively charged caroxylated QDs (as per the electrostatic fabrication protocol) and the lifetime of the solution measured. This was used as a baseline comparison to test the efficacy of electrostatic attraction between the PE capped AuNPs and QDs. The lifetime decay curves obtained for the AuNP@CTAB and PE-capped AuNP mixed with QDs are shown in Fig. 6.8d with the extracted lifetimes plotted in Fig. 6.9a. Despite the surface zeta potential for both the CTAB and polyDADMAC

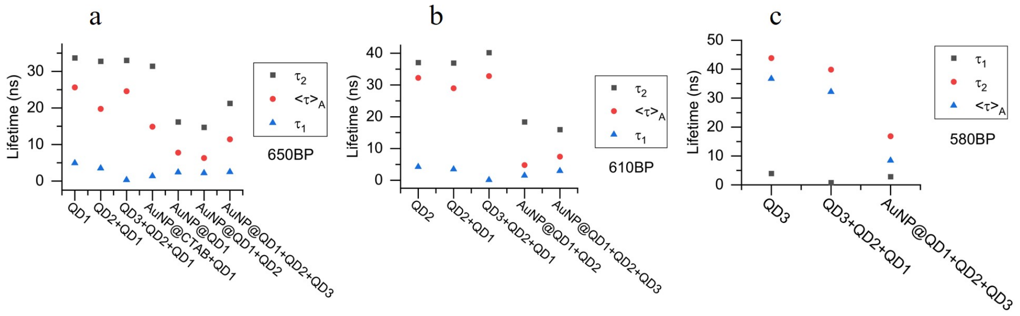

Figure 6.9: Extracted lifetime components (fast - blue triangles, slow - black squares, amplitude average - red circles) for the AuNP@QD samples measured at (a) 655 nm, (b) 605 nm, and (c) 585 nm.

capping having no discernible difference within the margin of error, it is evident from the decay curves that the PE layers have a profound effect on the attraction to QDs. Firstly, the lifetime decay curve background for the AuNP@CTAB-QD mixture is much greater than the PE capped AuNP sample indicating that the QD signal is much weaker, suggesting the QDs are either lower in concentration (after centrifugation) or are quenched more strongly by the AuNPs.

Secondly, the extracted lifetime values show a significant decrease in the amplitude averaged lifetime for the PE-capped AuNPs compared with AuNP@CTAB. Although not shown in the figures, the faster lifetime component amplitude increased from 0.28 (bare QDs) to 0.55 (AuNP@CTAB) and again to 0.61 (PE-capped AuNP). This increase suggests a greater proportion of the population (of QDs) is modified by the AuNP [19]. These two observations combined seems to indicate that the QDs are successfully binding to the PE capped AuNPs, and not to AuNP@CTAB where unbound QDs are discarded due to the centrifugation washes.

Then, the plasmon decay rate of QD655 can be calculated as before using the PE capped AuNP@QD655 lifetime and the QD only as a reference, yielding a k_{sp} of 0.090 ± 0.009 ns^{-1}. This is clearly much lower than the plasmon decay rate achieved in the conjugated system but is still greater than in the film based samples. This is possibly due to the fact that the QDs used in the conjugation are different - with a much lower PLQY (about 0.54), the radiative decay rate is not as high as with the carboxyl QDs here (PLQY of over 0.90). Therefore, the radiative decay pathway for the carboxyl QDs (used in this section) will likely be dominant, or at least comparable to the plasmon decay. Assuming the plasmon coupled decay is radiative and does not influence the QD intrinsic decay, then the PLQY of the carboxyl QDs cannot increase significantly without going above unity which is not physical. In addition, the increase in the value of k_{sp} here relative to the film structure (an enhancement of roughly 3.9 times) can also be attributed to the greater proportion of QD655 in a region of electric field enhancement around the AuNP, as suggested before.

Much like in the previous section, the lifetime behaviour and energy transfer decay rates of the constituent QDs surrounding a central, PE capped AuNP are investigated. Continuing with QD655, the addition of QD605 appears to maintain the measured average lifetime - only a slight decrease is recorded (see Fig. 6.9a). However, with the addition of QD585, this lifetime increases significantly to 11.42 ns. This behaviour is also observed in the QD605 case where the average lifetime increases going from the LSP-coupled 2QD to the 3QD case. In both samples, this rise can be attributed to an energy transfer [204], as seen in the film based structure, in which the donor QD585 increases the number of excitons in either layers. Therefore, it is of no surprise that we see a drastic reduction in the QD585 lifetime in the full AuNP coupled 3QD structure as shown in Fig. 6.9c. With these lifetimes, we can then calculate the energy extraction/transfer rate for QD605 and QD585, with and without plasmonic coupling (Table 6.3).

It is worth noting that for the AuNP coupled structures, the calculation $1/\tau_{DA@AuNP} - 1/\tau_D$ (middle column of Table 6.3) provides information about the energy transfer rate *and* plasmon decay rate. Therefore, in order to extract k_{ET}, k_{sp} must also be

Sample	$1/\tau_{DA@AuNP} - 1/\tau_D$ (ns^{-1})	k_{ET} (ns^{-1})
QD605+655 (610)	-	0.003
QD605+655@AuNP (610)	0.177	0.163
QD585+605+655 (610)	-	0
QD585+605+655@AuNP (610)	0.103	0.089
QD585+605+655 (580)	-	0.004
QD585+605+655@AuNP (580)	0.092	0.083

Table 6.3: Summary of the calculated energy transfer rates for the 2 and 3 QD structures in solution for with and without AuNP, measured at either 610 nm or 580 nm, indicated by the parentheses. The third column (k_{ET}) values are extracted from the second column by subtracting the film based k_{sp} values, where applicable, which are 0.014 ns^{-1}, and 0.009 ns^{-1} for QD605 and QD585, respectively.

known. Fortunately, as the nanoparticles used here are the same as in the film based structures, the k_{sp} values for the film structure (0.014 ns^{-1} for QD605, and 0.009 ns^{-1} for QD585) can be assumed to be approximately equal to the solution based LbL structures. However, this is only valid if the environment is kept constant in either case, which is not the case as the QDs are in a stronger localized field around the AuNP. Nevertheless, it is still a useful calculation to estimate the *differences* in the energy extraction rates, as k_{sp} is only expected to vary with distance and not with the presence of other QDs.

If the LSP-coupled energy extraction rates for the outer-most QD is examined in the two and three QD samples (e.g., for **QD605**+655 and **QD585**+605+655), an enhancement of 54 and 20 times are seen, respectively. A decline in the enhancement from the QD605 layer compared with the QD585 layer is an expected result owing to the greater separation from the AuNP surface for QD585, compared with QD605. What is interesting to note, however is the reduction in the extraction rate for the QD605 layer in the QD585+605+655@AuNP case compared with QD605+655@AuNP i.e., with the addition of the outermost QD585 layer. An initial inspection would indicate that the energy transfer efficiency has reduced due to the prescence of QD585 but this would not seem likely. Instead, it is more probable that the energy transfer from QD585 to QD605 only *appears* to reduce the transfer efficiency from QD605 to QD655, as the fluorescence lifetime of the QD605 layer increases. As discussed previously, this increase in lifetime is indicative of energy transfer for an acceptor. Thus, the modification of the energy transfer rate alone cannot be used to draw conclusions for a system that acts both as a donor and an acceptor. It is surprising to see that the addition of the QD585 layer has such a profound effect on the calculated k_{ET} of QD605 in the presence of AuNP despite having found previously that the metal should have little effect on the outer most QD layer.

6.4 Conclusion

To summarise, layers of QDs were used to encapsulate a AuNP in solution where the different layers consisted of different emission energy QDs. The first layer immediately next to the AuNP surface consisted of the lowest energy emission QDs (QD655) and sequential layers consisted of higher energy QDs. Two methods were used to fabricate such a system: the first method (termed "conjugated") involved the use of conjugated QDs with either Streptavidin or Biotin, and exploited these biological molecule's naturally high affinity to each other. This resulted in a relatively simple fabrication procedure, requiring minimal mixing times and washing steps producing relatively high yields. As the molecules were small, the separation between nanoparticles were minimal leading to extremely high exciton energy transfer rates of up to 4.8 ns^{-1}. However, this method required one to functionalize the AuNP surface, which proved to be somewhat difficult due to the close packing and high affinity of the CTAB capping molecules. This method also limits the separation between constituent nanoparticles to a fixed distance unless linker molecules of known lengths are used which are terminated with Streptavidin/Biotin at either ends. In reality, these are often polymers, such as polyethylene glycol (PEG), which are not rigid and can change their conformation which varies their length in solution depending on the environment conditions, including pH and salt content.

The second method (termed "LbL") utilised polyelectrolyte layers to encapsulate the AuNP by exploiting the CTAB and carboxylated QD charge at neutral pH to encourage electrostatic attraction between the nanoparticles. Although the fabrication required considerably more washing steps, resulting in lower overall yields, this method generally affords the user exquisite control of the distance between nanoparticles, in steps of approximately 2-3 nm depending on the number of spacer layers used. The energy transfer rate achieved is not as high as in the conjugated system, at 0.163 ns^{-1} which is an order of magnitude lower.

In either method, there still exists a rate limiting step for the energy transfer of excitons across the whole system, as observed for film-based structures in chapter 5. For the LbL and conjugated AuNP coupled 3QD layer systems, the rate limiting step appears to be the extraction from QD585 layer due to the lower energy extraction rate measured in comparison to the intermediate QD605 layer energy transfer rate and QD655 surface plamon decay rate. This may be attributed to the decrease in the quenching effect due to LSP-coupling and decreased enhancement of the FRET rate - both of which are affected by the increased distance from the AuNP surface.

Nevertheless, this demonstrates that AuNPs and QDs can be used to construct a core-shell like structure involving the encapsulation of the central AuNP with layers of QDs. Such a structure was shown to greatly affect the energy transfer dynamics of photo-generated excitons in the QD layers through plasmonic enhancement. From the sequential layering of QDs (starting with lowest, at the AuNP surface, to highest emission energies), it is likely that the energy transfer is unidirectional.

Chapter 7

Conclusion

To summarise, the thesis can be separated into two parts: the first, dealing with top-down approaches in fabricating gold-QD structures with particle level control of the placement. In the second part, non-lithographic self-assembled methods for constructing gold-QD complexes were explored with the context of harvesting and directed transfer of energy.

The top down method of choice was Electron Beam Lithography, where multiple writes were used over the same substrate surface. The motivation behind was to develop a multilayered QD system around AuNPs arrays where the relative positions of nanoparticles could be controlled and fixed to a substrate using self assembled methods. It was found that such a technique could be a viable option for nanometric control of an arbitrary number of nanoparticles: it would allow one to study distance dependent properties such as energy transfer and plasmonic coupling with relative ease, accuracy, and reproducibility.

Due to potential throughput issues that plague EBL, alternative methods to fabricate substrate based Au-QD structures were explored. Through self-assembled procedures, AuNP and QD films were layered on top of each other, separated by polyelectrolyte films that were constructed *via* the layer-by-layer method. Up to 3 layers of differing QD species were used, starting with the lowest emission energy QDs on top of AuNPs and ending with the highest energy QDs as the top-most layer. By measuring the lifetimes of different combinations of QDs with and without AuNP coupling, the excitonic behaviour across the different structures could be modelled. It was found that, not only was it highly probable that the excitons were funnelled across the layers in a unidirectional manner (from high to low energy QD films), the Au-QD complex exhibits a rate limiting step in which the excitons reach a so-called "bottleneck". A characteristic increase in the density of excitons in the acceptor layers was observed; the greatest increase was found in the intermediate QD605 layer, suggesting the transfer from this layer to the final QD655 was the rate limiting transfer pathway. Therefore, careful consideration of rate engineering, alongside bandgap engineering, should be taken for optimising the transfer of excitons across multi-layered structures. Furthermore, the model introduced in Chapter 5 was the result of a developed methodology to investigate the photo-dynamics of excitons in complex multilayered structures in which numerous de-excitation pathways are possible. This helped to explain the excitonic migration between the layers and allowed the estimation of the amount of energy transferred to the AuNP layer. To this end, the energy transferred was calculated to increase 6-fold from 1QD- to 3QD-layers essentially meaning the structure may act as an energy harvester.

From simulations, AuNPs on a glass substrate under normal incidence exhibited electric field enhancements of up to 7 times, mostly in the lateral regions around the AuNPs and near the substrate. Since most QDs in the structure resided in the top half space of the AuNPs, blocked by the PE layers, they were not in the region of the greatest field enhancement. For this reason, the last part of the thesis focussed on moving away from the 2D stratified Au-QD structure, towards a 3D core-shell Au-QD complex. Two different methods were used to construct the 3D complexes, consisting of a central AuNP surrounded by shell layers of QDs (in the same sequence as the substrate based samples). The two methods differed only in their choice of separating layers, using Streptavidin-Biotin linker proteins (termed "conjugated"), or PE layers (termed "LbL" instead). Both methods were successful, exhibiting large modifications to the fluorescence lifetimes of the QD shells. The plasmon coupled decay rate of excitons, k_{sp}, for the first QD layer was found to reach up to 0.4 ns^{-1} for the conjugated system and 0.09 ns^{-1} for the LbL system, both are greater than in the film based system of 0.02 ns^{-1}. Not only was the plasmon decay rate observed to increase, the LSP-coupled energy transfer rates for the 3QD@AuNP samples were also observed to increase by up to 3 times for the QD585 and QD605 layers in the electrostatic LbL sample compared to the 3QD@AuNP film sample. Similarly, the conjugated system saw an enhancement of the energy transfer rate of approximately 2 times for the QD585, and nearly 100 times for the QD605 compared to the same film system. This increase in the energy transfer rate is attributed to the distribution of QDs over the entire AuNP surface. This increases the likelihood that a greater proportion of QDs are in a region of greater field enhancement, in comparison to the fixed film system.

In all of these cases, it could be said that the Au-QD complexes act as energy harvesters, increasing the effective absorption cross section of the overall structure compared to the constituent nanoparticles individually. To the best of my knowledge, no other study has previously delved into a similar system involving the use of localised surface plasmon resonance coupled to multilayered films (greater than two layers) of QDs. Combined with the high precision control of nanoparticle positioning from lithographic techniques, it is exciting to see what the future holds in terms of directed transfer of energy across nanoparticle structures for applications including solar harvesting, purification, and light emitting devices, to name a few.

Publications

Miao Zhao, Edward Leggett, Struan Bourke, Souzana Poursanidou, Sadie Carter-Searjeant, Steve Po, Marciano Palma do Carmo, Lea Ann Dailey, Philip Manning, Sean G. Ryan, Laura Urbano, Mark A. Green, and Aliaksandra Rakovich. Theranostic Near-Infrared-Active Conjugated Polymer Nanoparticles . ACS Nano 15, 8790–8802 (2021).

Steve Po, Aliaksandra Rakovich. Energy Transfer Dynamics in Graded-Bandgap Quantum Dot Thin Films coupled to Gold Nanoparticles. Manuscript in preparation (2023).

Conferences

Hybrid plasmonic-SERS based biosensing. S. Po, M.P. Carmo, M. Zhao, S. Anguiano, M.L. Guyon, A. Reynoso, E. Cortes, S. Maier, A. Fainstein, L. Pedano, A. Rakovich. Oral presentation. 19th International Conference Laser Optics 2020, 2-6 November 2020, St. Petersburg, Russia.

Light harvesting complexes using biomimetic metallic nanoparticle-quantum dot assemblies. Steve Po, Marciano Palma do Carmo, Miao Zhao, America Mendoza, David Mack, Monica Mota, Aliaksandra Rakovich. Poster presentation. SPIE Photonics Europe 2022, 3-7 April 2022, Strasbourg, France.

Bibliography

1. IEA. *Electricity Information: Overview* accessed 2023-04-12. License: CC BY 4.0. 2021. `https://www.iea.org/reports/electricity-information-overview`.
2. WorldData.info. *Energy consumption in the United Kingdom* accessed 2023-04-12. `https://www.worlddata.info/europe/united-kingdom/energy-consumption.php`.
3. In Data, O. W. *Energy consumption by source* accessed 2023-04-12. `https://ourworldindata.org/grapher/energy-consumption-by-source-and-country?country=~GBR`.
4. IEA. *Solar PV* accessed = 2023-04-12. 2022. `https://www.iea.org/reports/solar-pv`.
5. Office of Energy Efficiency & Renewable Energy, U. D. o. E. *Solar Integration: Solar Energy and Storage Basics* accessed 2023-04-12. `https://www.energy.gov/eere/solar/solar-integration-solar-energy-and-storage-basics`.
6. Wang, S., Lu, A. & Zhong, C.-J. Hydrogen production from water electrolysis: role of catalysts. *Nano Convergence* **8,** 4. ISSN: 2196-5404. `https://doi.org/10.1186/s40580-021-00254-x` (2021).

7. Hodges, A. *et al.* A high-performance capillary-fed electrolysis cell promises more cost-competitive renewable hydrogen. *Nature Communications* **13,** 1304. ISSN: 2041-1723. `https://doi.org/10.1038/s41467-022-28953-x` (2022).

8. Ezendam, S. *et al.* Hybrid Plasmonic Nanomaterials for Hydrogen Generation and Carbon Dioxide Reduction. *ACS Energy Letters* **7.** doi: 10.1021/acsenergylett.1c02241, 778–815. `https://doi.org/10.1021/acsenergylett.1c02241` (2022).

9. Simoncelli, S. *et al.* Monitoring plasmonic hot-carrier chemical reactions at the single particle level. *Faraday Discussions* **214,** 73–87. ISSN: 1359-6640. `http://dx.doi.org/10.1039/C8FD00138C` (2019).

10. Reddy, H. *et al.* Determining plasmonic hot-carrier energy distributions via single-molecule transport measurements. *Science* **369,** 423–426. `https://www.science.org/doi/abs/10.1126/science.abb3457` (2020).

11. Ahlawat, M., Mittal, D. & Govind Rao, V. Plasmon-induced hot-hole generation and extraction at nano-heterointerfaces for photocatalysis. *Communications Materials* **2,** 114. ISSN: 2662-4443. `https://doi.org/10.1038/s43246-021-00220-4` (2021).

12. Cushing, S. K. *et al.* Photocatalytic Activity Enhanced by Plasmonic Resonant Energy Transfer from Metal to Semiconductor. *Journal of the American Chemical Society* **134.** doi: 10.1021/ja305603t, 15033–15041. ISSN: 0002-7863. `https://doi.org/10.1021/ja305603t` (2012).

13. Li, J. *et al.* Plasmon-induced resonance energy transfer for solar energy conversion. *Nature Photonics* **9,** 601–607. ISSN: 1749-4893. `https://doi.org/10.1038/nphoton.2015.142` (2015).

14. Zhang, Y. *et al.* Surface-Plasmon-Driven Hot Electron Photochemistry. *Chemical Reviews* **118.** doi: 10.1021/acs.chemrev.7b00430, 2927–2954. ISSN: 0009-2665. `https://doi.org/10.1021/acs.chemrev.7b00430` (2018).

15. Walters, R. J., van Loon, R. V. A., Brunets, I., Schmitz, J. & Polman, A. A silicon-based electrical source of surface plasmon polaritons. *Nature Materials* **9,** 21–25. ISSN: 1476-4660. `https://doi.org/10.1038/nmat2595` (2010).

16. Jun, Y. C., Kekatpure, R. D., White, J. S. & Brongersma, M. L. Nonresonant enhancement of spontaneous emission in metal-dielectric-metal plasmon waveguide structures. *Physical Review B* **78,** 153111. `https://link.aps.org/doi/10.1103/PhysRevB.78.153111` (2008).

17. Kruger, P. Appropriate technologies for large-scale production of electricity and hydrogen fuel. *International Journal of Hydrogen Energy* **33,** 5881–5886. ISSN: 0360-3199. `https://www.sciencedirect.com/science/article/pii/S0360319908009749` (2008).

18. Stokes, G. G. XXX. On the change of refrangibility of light. *Philosophical Transactions of the Royal Society of London* **142,** 463–562. `https://doi.org/10.1098/rstl.1852.0022` (1852).

19. Lakowicz, J. R. *Principles of Fluorescence Spectroscopy* 3rd ed., 954. ISBN: 978-0-387-31278-1 (Springer New York, NY, 2006).

20. Szöllősi, J., Damjanovich, S. & Mátyus, L. Principles of Resonance Energy Transfer. *Current Protocols in Cytometry* **9,** 1.12.1–1.12.13. ISSN: 1934-9297. `https://currentprotocols.onlinelibrary.wiley.com/doi/abs/10.1002/0471142956.cy0112s09` (1999).

21. Andrews, D. & Bradshaw, D. in *Encyclopedia of Applied Spectroscopy* (ed Andrews, D. L.) 533–554 (Wiley, 2009). ISBN: 978-3-527-40773-6. `https://ueaeprints.uea.ac.uk/id/eprint/51136/`.

22. Jones, G. A. & Bradshaw, D. S. Resonance Energy Transfer: From Fundamental Theory to Recent Applications. *Frontiers in Physics* **7.** ISSN: 2296-424X. `https://www.frontiersin.org/articles/10.3389/fphy.2019.00100` (2019).

23. Valeur, B. in *Molecular Fluorescence* 247–272 (2001). `https://onlinelibrary.wiley.com/doi/abs/10.1002/3527600248.ch9`.

24. Clapp, A. R. *et al.* Fluorescence Resonance Energy Transfer Between Quantum Dot Donors and Dye-Labeled Protein Acceptors. *Journal of the American Chemical Society* **126,** 301–310. ISSN: 0002-7863. `https://doi.org/10.1021/ja037088b` (2004).

25. Wang, H. *et al.* Controlled transition dipole alignment of energy donor and energy acceptor molecules in doped organic crystals, and the effect on intermolecular Förster energy transfer. *Physical Chemistry Chemical Physics* **15,** 3527. ISSN: 1463-9076. `https://dx.doi.org/10.1039/c3cp43800g` (2013).

26. Akhavan, S., Akgul, M. Z., Hernandez-Martinez, P. L. & Demir, H. V. Plasmon-Enhanced Energy Transfer in Photosensitive Nanocrystal Device. *ACS Nano* **11,** 5430–5439. ISSN: 1936-0851. `https://doi.org/10.1021/acsnano.6b08392` (2017).

27. Hernández-Martínez, P. L., Govorov, A. O. & Demir, H. V. Förster-Type Nonradiative Energy Transfer for Assemblies of Arrayed Nanostructures: Confinement Dimension vs Stacking Dimension. *The Journal of Physical Chemistry C* **118,** 4951–4958. ISSN: 1932-7447. `https://doi.org/10.1021/jp409833b` (2014).

28. Achermann, M., Jeong, S., Balet, L., Montano, G. A. & Hollingsworth, J. A. Efficient Quantum Dot-Quantum Dot and Quantum Dot-Dye Energy Trans-

fer in Biotemplated Assemblies. *ACS Nano* **5,** 1761–1768. ISSN: 1936-0851. `https://doi.org/10.1021/nn102365v` (2011).

29. Massey, M., Algar, W. R. & Krull, U. J. Fluorescence resonance energy transfer (FRET) for DNA biosensors: FRET pairs and Förster distances for various dye–DNA conjugates. *Analytica Chimica Acta* **568,** 181–189. ISSN: 0003-2670. `https://www.sciencedirect.com/science/article/pii/S0003267005021094` (2006).

30. Müller, S., Galliardt, H., Schneider, J., Barisas, B. & Seidel, T. Quantification of Förster resonance energy transfer by monitoring sensitized emission in living plant cells. *Frontiers in Plant Science* **4.** ISSN: 1664-462X. `https://www.frontiersin.org/article/10.3389/fpls.2013.00413` (2013).

31. Qiao, Y., Luo, Y., Long, N., Xing, Y. & Tu, J. Single-Molecular Förster Resonance Energy Transfer Measurement on Structures and Interactions of Biomolecules. *Micromachines* **12,** 492. ISSN: 2072-666X (2021).

32. Roberts, M. S. *et al.* Non-invasive imaging of skin physiology and percutaneous penetration using fluorescence spectral and lifetime imaging with multiphoton and confocal microscopy. *European Journal of Pharmaceutics and Biopharmaceutics* **77,** 469–488. ISSN: 0939-6411. `https://www.sciencedirect.com/science/article/pii/S0939641110003644` (2011).

33. Langhals, H. & Schlücker, T. Dependence of the Fluorescent Lifetime τ on the Concentration at High Dilution. *The Journal of Physical Chemistry Letters* **13,** 7568–7573. `https://doi.org/10.1021/acs.jpclett.2c01447` (2022).

34. Maier, S. *Plasmonics: Fundamentals and applications* 1st ed. (Springer, 2006).

35. Bohren, C. F. & Huffman, D. R. *Absorption and Scattering of Light by Small Particles* `https://dx.doi.org/10.1002/9783527618156` (Wiley, 1998).

36. Jackson, J. D. *Classical Electrodynamics* 3rd ed. (Wiley, 1999).

37. Purcell, E. M. Spontaneous Emission Probabilities at Radio Frequencies. *Physical Review* **69,** 681. `http://link.aps.org/doi/10.1103/PhysRev.69.674.2` (1946).

38. Ratchford, D., Shafiei, F., Kim, S., Gray, S. K. & Li, X. Manipulating Coupling between a Single Semiconductor Quantum Dot and Single Gold Nanoparticle. *Nano Letters* **11,** 1049–1054. ISSN: 1530-6984. `https://doi.org/10.1021/nl103906f` (2011).

39. Liaw, J.-W., Chen, J.-H., Chen, C.-S. & Kuo, M.-K. Purcell effect of nanoshell dimer on single molecule's fluorescence. *Optics Express* **17,** 13532–13540. `https://opg.optica.org/oe/abstract.cfm?URI=oe-17-16-13532` (2009).

40. Srinivasan, V. & Ramamurthy, S. S. Purcell Factor: A Tunable Metric for Plasmon-Coupled Fluorescence Emission Enhancements in Cermet Nanocavities. *The Journal of Physical Chemistry C* **120,** 2908–2913. ISSN: 1932-7447. `https://doi.org/10.1021/acs.jpcc.5b11311` (2016).

41. Tsurumachi, N. *et al.* Dependence of Purcell effect on fluorescence wavelength in dye molecules on metal–dielectric multilayer hyperbolic metamaterials. *Japanese Journal of Applied Physics* **55,** 02BB05. ISSN: 1347-4065 0021-4922. `https://dx.doi.org/10.7567/JJAP.55.02BB05` (2016).

42. Morozov, K. M. *et al.* Revising of the Purcell effect in periodic metal-dielectric structures: the role of absorption. *Scientific Reports* **9,** 9604. ISSN: 2045-2322. `https://doi.org/10.1038/s41598-019-46071-5` (2019).

43. Shimizu, K. T., Woo, W. K., Fisher, B. R., Eisler, H. J. & Bawendi, M. G. Surface-Enhanced Emission from Single Semiconductor Nanocrystals. *Physical Review Letters* **89.** ISSN: 0031-9007. `https://dx.doi.org/10.1103/physrevlett.89.117401` (2002).

44. Cade, N. I. *et al.* Plasmonic Enhancement of Fluorescence and Raman Scattering by Metal Nanotips. *NanoBiotechnology* **3,** 203–211. ISSN: 1551-1294. `https://doi.org/10.1007/s12030-009-9020-x` (2007).

45. Huang, F. M. & Richards, D. Fluorescence enhancement and energy transfer in apertureless scanning near-field optical microscopy. *Journal of Optics A: Pure and Applied Optics* **8,** S234. ISSN: 1464-4258. `https://dx.doi.org/10.1088/1464-4258/8/4/S25` (2006).

46. Anger, P., Bharadwaj, P. & Novotny, L. Enhancement and Quenching of Single-Molecule Fluorescence. *Physical Review Letters* **96.** ISSN: 0031-9007. `https://dx.doi.org/10.1103/physrevlett.96.113002` (2006).

47. Bharadwaj, P. & Novotny, L. Spectral dependence of single molecule fluorescence enhancement. *Optics Express* **15,** 14266–14274. `https://opg.optica.org/oe/abstract.cfm?URI=oe-15-21-14266` (2007).

48. Borrero Landazabal, D., Meza Olivo, A. A., Garay Palmett, K. & Salas Montiel, R. Reduction of the fluorescence lifetime of quantum dots in presence of plasmonic nanostructures. *Journal of Physics: Conference Series* **1159,** 012004. ISSN: 1742-6596 1742-6588. `https://dx.doi.org/10.1088/1742-6596/1159/1/012004` (2019).

49. Cho, H. *et al.* Importance of Purcell factor for optimizing structure of organic light-emitting diodes. *Optics Express* **27,** 11057–11068. `https://opg.optica.org/oe/abstract.cfm?URI=oe-27-8-11057` (2019).

50. Dulkeith, E. *et al.* Gold Nanoparticles Quench Fluorescence by Phase Induced Radiative Rate Suppression. *Nano Letters* **5,** 585–589. ISSN: 1530-6984. `https://doi.org/10.1021/nl0480969` (2005).

51. Aussenegg, F. R., Leitner, A., Lippitsch, M. E., Reinisch, H. & Riegler, M. Novel aspects of fluorescence lifetime for molecules positioned close to metal surfaces. *Surface Science* **189-190,** 935–945. ISSN: 0039-6028. `https://www.sciencedirect.com/science/article/pii/S0039602887805319` (1987).

52. Song, J.-H., Atay, T., Shi, S., Urabe, H. & Nurmikko, A. V. Large Enhancement of Fluorescence Efficiency from CdSe/ZnS Quantum Dots Induced by Resonant Coupling to Spatially Controlled Surface Plasmons. *Nano Letters* **5.** doi: 10.1021/nl050813r, 1557–1561. ISSN: 1530-6984. `https://doi.org/10.1021/nl050813r` (2005).

53. Shin, T. *et al.* Exciton Recombination, Energy-, and Charge Transfer in Single- and Multilayer Quantum-Dot Films on Silver Plasmonic Resonators. *Scientific Reports* **6,** 26204. ISSN: 2045-2322. `https://doi.org/10.1038/srep26204` (2016).

54. Ekimov, A. I., Efros, A. L. & Onushchenko, A. A. Quantum size effect in semiconductor microcrystals. *Solid State Communications* **56,** 921–924. ISSN: 0038-1098. `https://www.sciencedirect.com/science/article/pii/S0038109885800259` (1985).

55. Loss, D. & DiVincenzo, D. P. Quantum computation with quantum dots. *Physical Review A* **57.** PRA, 120–126. `https://link.aps.org/doi/10.1103/PhysRevA.57.120` (1998).

56. Mashford, B. S. *et al.* High-efficiency quantum-dot light-emitting devices with enhanced charge injection. *Nature Photonics* **7,** 407–412. ISSN: 1749-4893. `https://doi.org/10.1038/nphoton.2013.70` (2013).

57. Geiregat, P., Van Thourhout, D. & Hens, Z. A bright future for colloidal quantum dot lasers. *NPG Asia Materials* **11,** 41. ISSN: 1884-4057. `https://doi.org/10.1038/s41427-019-0141-y` (2019).

58. Jaliel, G. *et al.* Experimental Realization of a Quantum Dot Energy Harvester. *Physical Review Letters* **123.** PRL, 117701. `https://link.aps.org/doi/10.1103/PhysRevLett.123.117701` (2019).

59. Kim, T.-H. *et al.* Full-colour quantum dot displays fabricated by transfer printing. *Nature Photonics* **5,** 176–182. ISSN: 1749-4885. `https://dx.doi.org/10.1038/nphoton.2011.12` (2011).

60. Choi, M. K., Yang, J., Hyeon, T. & Kim, D.-H. Flexible quantum dot light-emitting diodes for next-generation displays. *npj Flexible Electronics* **2,** 10. ISSN: 2397-4621. `https://doi.org/10.1038/s41528-018-0023-3` (2018).

61. Huang, Y.-M. *et al.* Advances in Quantum-Dot-Based Displays. *Nanomaterials* **10,** 1327. ISSN: 2079-4991. `https://dx.doi.org/10.3390/nano10071327` (2020).

62. Yang, J. *et al.* Toward Full-Color Electroluminescent Quantum Dot Displays. *Nano Letters* **21,** 26–33. ISSN: 1530-6984. `https://doi.org/10.1021/acs.nanolett.0c03939` (2021).

63. Panchuk-Voloshina, N. *et al.* Alexa Dyes, a Series of New Fluorescent Dyes that Yield Exceptionally Bright, Photostable Conjugates. *Journal of Histochemistry & Cytochemistry* **47,** 1179–1188. ISSN: 0022-1554 (1999).

64. Resch-Genger, U., Grabolle, M., Cavaliere-Jaricot, S., Nitschke, R. & Nann, T. Quantum dots versus organic dyes as fluorescent labels. *Nature Methods* **5,** 763–775. ISSN: 1548-7105. `https://doi.org/10.1038/nmeth.1248` (2008).

65. Nakonechnyi, I. *et al.* P-239: Late-News Poster: Quantum Dots for Display Applications, Thermal and Photostability through Shell Design. *SID Symposium Digest of Technical Papers* **48,** 1722–1724. ISSN: 0097-966X. `https://sid.onlinelibrary.wiley.com/doi/abs/10.1002/sdtp.11986` (2017).

66. Jasieniak, J., Califano, M. & Watkins, S. E. Size-Dependent Valence and Conduction Band-Edge Energies of Semiconductor Nanocrystals. *ACS Nano* **5,** 5888–5902. ISSN: 1936-0851. `https://dx.doi.org/10.1021/nn201681s` (2011).

67. Cingarapu, S., Yang, Z., Sorensen, C. M. & Klabunde, K. J. Synthesis of CdSe/ZnS and CdTe/ZnS Quantum Dots: Refined Digestive Ripening. *Journal of Nanomaterials* **2012,** 312087. ISSN: 1687-4110. `https://doi.org/10.1155/2012/312087` (2012).

68. Murray, C. B., Norris, D. J. & Bawendi, M. G. Synthesis and characterization of nearly monodisperse CdE (E = sulfur, selenium, tellurium) semiconductor nanocrystallites. *Journal of the American Chemical Society* **115,** 8706–8715. ISSN: 0002-7863. `https://doi.org/10.1021/ja00072a025` (1993).

69. Davoodi, M., Davar, F., Mandani, S., Rezaei, B. & Shalan, A. E. CdSe Quantum Dot Nanoparticles: Synthesis and Application in the Development of Molecularly Imprinted Polymer-Based Dual Optical Sensors. *Industrial & Engineering Chemistry Research* **60,** 12328–12342. ISSN: 0888-5885. `https://doi.org/10.1021/acs.iecr.1c02124` (2021).

70. Liu, J. *et al.* Assessing Clinical Prospects of Silicon Quantum Dots: Studies in Mice and Monkeys. *ACS Nano* **7,** 7303–7310. ISSN: 1936-0851. `https://doi.org/10.1021/nn4029234` (2013).

71. Nirmal, M. *et al.* Fluorescence intermittency in single cadmium selenide nanocrystals. *Nature* **383,** 802–804. ISSN: 1476-4687. `https://doi.org/10.1038/383802a0` (1996).

72. Efros, A. L. Almost always bright. *Nature Materials* **7,** 612–613. ISSN: 1476-4660. `https://doi.org/10.1038/nmat2239` (2008).

73. Frantsuzov, P. A., Volkán-Kacsó, S. & Jankó, B. Universality of the Fluorescence Intermittency in Nanoscale Systems: Experiment and Theory. *Nano Letters* **13,** 402–408. ISSN: 1530-6984. `https://doi.org/10.1021/nl3035674` (2013).

74. Mahler, B. *et al.* Towards non-blinking colloidal quantum dots. *Nature Materials* **7,** 659–664. ISSN: 1476-4660. `https://doi.org/10.1038/nmat2222` (2008).

75. Hohng, S. & Ha, T. Near-Complete Suppression of Quantum Dot Blinking in Ambient Conditions. *Journal of the American Chemical Society* **126.** doi: 10.1021/ja039686w, 1324–1325. ISSN: 0002-7863. `https://doi.org/10.1021/ja039686w` (2004).

76. Lidke, K. A., Rieger, B., Jovin, T. M. & Heintzmann, R. Superresolution by localization of quantum dots using blinking statistics. *Optics Express* **13,** 7052–7062. `https://opg.optica.org/oe/abstract.cfm?URI=oe-13-18-7052` (2005).

77. Chien, F.-C., Kuo, C. W. & Chen, P. Localization imaging using blinking quantum dots. *The Analyst* **136,** 1608. ISSN: 0003-2654. `https://dx.doi.org/10.1039/c0an00859a` (2011).

78. Wang, Y., Fruhwirth, G., Cai, E., Ng, T. & Selvin, P. R. 3D Super-Resolution Imaging with Blinking Quantum Dots. *Nano Letters* **13,** 5233–5241. ISSN: 1530-6984. `https://doi.org/10.1021/nl4026665` (2013).

79. and, A. L. E. & Rosen, M. The Electronic Structure of Semiconductor Nanocrystals. *Annual Review of Materials Science* **30,** 475–521. `https://www.annualreviews.org/doi/abs/10.1146/annurev.matsci.30.1.475` (2000).

80. Kyhm, K., Kim, J. H., Kim, S. M. & Yang, H.-s. Gain dynamics and excitonic transition in CdSe colloidal quantum dots. *Optical Materials* **30,** 158–160. ISSN: 0925-3467. `https://www.sciencedirect.com/science/article/pii/S0925346706004137` (2007).

81. Brus, L. E. A simple model for the ionization potential, electron affinity, and aqueous redox potentials of small semiconductor crystallites. *The Journal of Chemical Physics* **79,** 5566–5571. ISSN: 0021-9606. `https://dx.doi.org/10.1063/1.445676` (1983).

82. Trindade, T., O'Brien, P. & Pickett, N. L. Nanocrystalline Semiconductors: Synthesis, Properties, and Perspectives. *Chemistry of Materials* **13,** 3843–3858. ISSN: 0897-4756. `https://doi.org/10.1021/cm000843p` (2001).

83. Agrawal, D. C. in *Introduction to Nanoscience and Nanomaterials* 117–139 (WORLD SCIENTIFIC, 2012). ISBN: 978-981-4397-97-1. `https://doi.org/10.1142/9789814397988_0004`.

84. Kim, S., Fisher, B., Eisler, H.-J. & Bawendi, M. Type-II Quantum Dots: CdTe/CdSe(Core/Shell) and CdSe/ZnTe(Core/Shell) Heterostructures. *Journal of the American Chemical Society* **125.** doi: 10.1021/ja0361749, 11466–11467. ISSN: 0002-7863. `https://doi.org/10.1021/ja0361749` (2003).

85. Nandan, Y. & Mehata, M. S. Wavefunction Engineering of Type-I/Type-II Excitons of CdSe/CdS Core-Shell Quantum Dots. *Scientific Reports* **9,** 2. ISSN: 2045-2322. `https://doi.org/10.1038/s41598-018-37676-3` (2019).

86. Yu, P. Y. & Cardona, M. in *Fundamentals of Semiconductors: Physics and Materials Properties* (eds Yu, P. Y. & Cardona, M.) 469–551 (Springer Berlin Heidelberg, Berlin, Heidelberg, 1996). ISBN: 978-3-540-26475-0. `https://doi.org/10.1007/3-540-26475-2_9`.

87. Ji, B., Koley, S., Slobodkin, I., Remennik, S. & Banin, U. ZnSe/ZnS Core/Shell Quantum Dots with Superior Optical Properties through Thermodynamic Shell Growth. *Nano Letters* **20.** doi: 10.1021/acs.nanolett.9b05020, 2387–2395. ISSN: 1530-6984. `https://doi.org/10.1021/acs.nanolett.9b05020` (2020).

88. Renschler, C. L. & Harrah, L. A. Determination of quantum yields of fluorescence by optimizing the fluorescence intensity. *Analytical Chemistry* **55,** 798–800. ISSN: 0003-2700. `https://doi.org/10.1021/ac00255a050` (1983).

89. Williams, A. T. R., Winfield, S. A. & Miller, J. N. Relative fluorescence quantum yields using a computer-controlled luminescence spectrometer. *The Analyst* **108,** 1067. ISSN: 0003-2654. `https://dx.doi.org/10.1039/an9830801067` (1983).

90. Crosby, G. A. & Demas, J. N. Measurement of photoluminescence quantum yields. Review. *The Journal of Physical Chemistry* **75,** 991–1024. ISSN: 0022-3654. `https://doi.org/10.1021/j100678a001` (1971).

91. Tranter, G. in *Encyclopedia of Spectroscopy and Spectrometry (Second Edition)* (ed Lindon, J. C.) 2881–2885 (Academic Press, Oxford, 2010). ISBN: 978-0-12-374413-5. `https://www.sciencedirect.com/science/article/pii/B9780123744135000750`.

92. Stetefeld, J., Mckenna, S. A. & Patel, T. R. Dynamic light scattering: a practical guide and applications in biomedical sciences. *Biophysical Reviews* **8,** 409–427. ISSN: 1867-2450. `https://dx.doi.org/10.1007/s12551-016-0218-6` (2016).

93. Tscharnuter, W. in *Encyclopedia of Analytical Chemistry* (John Wiley & Sons, Ltd, 2006). ISBN: 9780470027318. eprint: `https://onlinelibrary.wiley.`

com/doi/pdf/10.1002/9780470027318.a1512. https://onlinelibrary.wiley.com/doi/abs/10.1002/9780470027318.a1512.

94. Pusey, P. N. in *Photon Correlation and Light Beating Spectroscopy* (eds Cummins, H. Z. & Pike, E. R.) 387–428 (Springer US, Boston, MA, 1974). ISBN: 978-1-4615-8906-8. https://doi.org/10.1007/978-1-4615-8906-8_10.

95. Stetefeld, J., McKenna, S. A. & Patel, T. R. Dynamic light scattering: a practical guide and applications in biomedical sciences. *Biophysical Reviews* **8,** 409–427. ISSN: 1867-2469. https://doi.org/10.1007/s12551-016-0218-6 (2016).

96. Maguire, C. M., Rösslein, M., Wick, P. & Prina-Mello, A. Characterisation of particles in solution – a perspective on light scattering and comparative technologies. *Science and Technology of Advanced Materials* **19,** 732–745. ISSN: 1468-6996. https://dx.doi.org/10.1080/14686996.2018.1517587 (2018).

97. Malvern. *Zetasizer Nano User Manual* English. Malvern (2013).

98. O'Connor, D. *Time-Correlated Single Photon Counting* ISBN: 9780323141444 (Academic Press, 1984).

99. Hirvonen, L. M., Petrášek, Z., Beeby, A. & Suhling, K. Sub-μs time resolution in wide-field time-correlated single photon counting microscopy obtained from the photon event phosphor decay. *New Journal of Physics* **17,** 023032. ISSN: 1367-2630. https://dx.doi.org/10.1088/1367-2630/17/2/023032 (2015).

100. Kagan, C. R., Murray, C. B. & Bawendi, M. G. Long-range resonance transfer of electronic excitations in close-packed CdSe quantum-dot solids. *Physical Review B* **54,** 8633–8643. ISSN: 0163-1829. https://dx.doi.org/10.1103/physrevb.54.8633 (1996).

101. Sillen, A. & Engelborghs, Y. The Correct Use of "Average" Fluorescence Parameters. *Photochemistry and Photobiology* **67,** 475–486. eprint: `https://onlinelibrary.wiley.com/doi/pdf/10.1111/j.1751-1097.1998.tb09082.x`. `https://onlinelibrary.wiley.com/doi/abs/10.1111/j.1751-1097.1998.tb09082.x` (1998).

102. Neri, L. *et al.* Note: Dead time causes and correction method for single photon avalanche diode devices. *Review of Scientific Instruments* **81,** 086102. eprint: `https://doi.org/10.1063/1.3476317`. `https://doi.org/10.1063/1.3476317` (2010).

103. Wahl, M. *Time-Correlated Single Photon Counting* tech. rep. (PicoQuant). `https://www.picoquant.com/images/uploads/page/files/7253/technote_tcspc.pdf`.

104. Smith, D. A., McKenzie, G., Jones, A. C. & Smith, T. A. Analysis of time-correlated single photon counting data: a comparative evaluation of deterministic and probabilistic approaches. *Methods and Applications in Fluorescence* **5,** 042001. ISSN: 2050-6120. `https://dx.doi.org/10.1088/2050-6120/aa8055` (2017).

105. McKinnon, A. E., Szabo, A. G. & Miller, D. R. The deconvolution of photoluminescence data. *The Journal of Physical Chemistry* **81,** 1564–1570. ISSN: 0022-3654. `https://doi.org/10.1021/j100531a009` (1977).

106. Pacheco-Liñán, P. J., Bravo, I., Nueda, M. L., Albaladejo, J. & Garzón-Ruiz, A. Functionalized CdSe/ZnS Quantum Dots for Intracellular pH Measurements by Fluorescence Lifetime Imaging Microscopy. *ACS Sensors* **5.** doi: 10.1021/acssensors.0c00719, 2106–2117. `https://doi.org/10.1021/acssensors.0c00719` (2020).

107. Herrera-Ochoa, D., Pacheco-Liñán, P. J., Bravo, I. & Garzón-Ruiz, A. A Novel Quantum Dot-Based pH Probe for Long-Term Fluorescence Lifetime Imaging Microscopy Experiments in Living Cells. *ACS Applied Materials & Interfaces* **14,** 2578–2586. ISSN: 1944-8244. `https://doi.org/10.1021/acsami.1c19926` (2022).

108. Ripoll, C., Orte, A., Paniza, L. & Ruedas-Rama, M. J. A Quantum Dot-Based FLIM Glucose Nanosensor. *Sensors* **19,** 4992. ISSN: 1424-8220. `https://www.mdpi.com/1424-8220/19/22/4992` (2019).

109. Loura, L. & Prieto, M. FRET in Membrane Biophysics: An Overview. *Frontiers in Physiology* **2.** ISSN: 1664-042X. `https://www.frontiersin.org/articles/10.3389/fphys.2011.00082` (2011).

110. Cheng, X. *et al.* Enhancing Quantum Dots for Bioimaging using Advanced Surface Chemistry and Advanced Optical Microscopy: Application to Silicon Quantum Dots (SiQDs). *Advanced Materials* **27.** https://doi.org/10.1002/adma.201503223, 6144–6150. ISSN: 0935-9648. `https://doi.org/10.1002/adma.201503223` (2015).

111. Datta, R., Heaster, T., Sharick, J., Gillette, A. & Skala, M. Fluorescence lifetime imaging microscopy: fundamentals and advances in instrumentation, analysis, and applications. *Journal of Biomedical Optics* **25,** 071203. `https://doi.org/10.1117/1.JBO.25.7.071203` (2020).

112. Ruan, Q., Shao, L., Shu, Y., Wang, J. & Wu, H. Growth of Monodisperse Gold Nanospheres with Diameters from 20 nm to 220 nm and Their Core/Satellite Nanostructures. *Advanced Optical Materials* **2,** 65–73. ISSN: 2195-1071. `https://onlinelibrary.wiley.com/doi/abs/10.1002/adom.201300359` (2014).

113. Gómez-Graña, S. *et al.* Surfactant (Bi)Layers on Gold Nanorods. *Langmuir* **28,** 1453–1459. ISSN: 0743-7463. https://doi.org/10.1021/la203451p (2012).

114. Pérez-Juste, J., Liz-Marzán, L. M., Carnie, S., Chan, D. Y. C. & Mulvaney, P. Electric-Field-Directed Growth of Gold Nanorods in Aqueous Surfactant Solutions. *Advanced Functional Materials* **14,** 571–579. ISSN: 1616-301X. https://doi.org/10.1002/adfm.200305068 (2004).

115. Souza, T. G. F., Ciminelli, V. S. T. & Mohallem, N. D. S. A comparison of TEM and DLS methods to characterize size distribution of ceramic nanoparticles. *Journal of Physics: Conference Series* **733,** 012039. ISSN: 1742-6596 1742-6588. https://dx.doi.org/10.1088/1742-6596/733/1/012039 (2016).

116. Carr, D. W. & Tiberio, R. C. Direct-write Electron Beam Lithography: History and State of the Art. *MRS Online Proceedings Library* **584,** 33–43. ISSN: 1946-4274. https://doi.org/10.1557/PROC-584-33 (1999).

117. Yamazaki, K. & Namatsu, H. 5-nm-Order Electron-Beam Lithography for Nanodevice Fabrication. *Japanese Journal of Applied Physics* **43,** 3767. ISSN: 1347-4065 0021-4922. https://dx.doi.org/10.1143/JJAP.43.3767 (2004).

118. Maalouf, A., Gadonna, M. & Bosc, D. An improvement in standard photolithography resolution based on Kirchhoff diffraction studies. *Journal of Physics D: Applied Physics* **42,** 015106. ISSN: 0022-3727. https://dx.doi.org/10.1088/0022-3727/42/1/015106 (2009).

119. Tanenbaum, D. M. High resolution electron beam lithography using ZEP-520 and KRS resists at low voltage. *Journal of Vacuum Science & Technology B: Microelectronics and Nanometer Structures* **14,** 3829. ISSN: 0734-211X. https://dx.doi.org/10.1116/1.588676 (1996).

120. Chen, Y., Macintyre, D. & Thoms, S. Fabrication of T-shaped gates using UVIII chemically amplified DUV resist and PMMA. **35,** 338–339. ISSN: 0013-5194. `https://digital-library.theiet.org/content/journals/10.1049/el_19990196` (1999).

121. Koshelev, K. *et al.* Comparison between ZEP and PMMA resists for nanoscale electron beam lithography experimentally and by numerical modeling. *Journal of Vacuum Science & Technology B* **29.** doi: 10.1116/1.3640794, 06F306. ISSN: 2166-2746. `https://doi.org/10.1116/1.3640794` (2011).

122. Namatsu, H. Three-dimensional siloxane resist for the formation of nanopatterns with minimum linewidth fluctuations. *Journal of Vacuum Science; Technology B: Microelectronics and Nanometer Structures* **16,** 69. ISSN: 0734-211X. `https://dx.doi.org/10.1116/1.589837` (1998).

123. Bonam, R., Verhagen, P., Munder, A. & Hartley, J. Performance characterization of negative resists for sub-10-nm electron beam lithography. *Journal of Vacuum Science & Technology B, Nanotechnology and Microelectronics: Materials, Processing, Measurement, and Phenomena* **28,** C6C34–C6C40. ISSN: 2166-2746. `https://dx.doi.org/10.1116/1.3517721` (2010).

124. Tan, Y. S., Liu, H., Ruan, Q., Wang, H. & Yang, J. K. W. Plasma-assisted filling electron beam lithography for high throughput patterning of large area closed polygon nanostructures. *Nanoscale* **12,** 10584–10591. ISSN: 2040-3364. `https://dx.doi.org/10.1039/d0nr01032d` (2020).

125. Koval, Y. Mechanism of etching and surface relief development of PMMA under low-energy ion bombardment. *Journal of Vacuum Science & Technology B: Microelectronics and Nanometer Structures* **22,** 843. ISSN: 0734-211X. `https://dx.doi.org/10.1116/1.1689306` (2004).

126. Sidorov, F. A. & Rogozhin, A. E. Microscopic simulation of e-beam induced PMMA chain scissions with temperature effect. *Journal of Physics: Conference Series* **1695,** 012202. ISSN: 1742-6596 1742-6588. `https://dx.doi.org/10.1088/1742-6596/1695/1/012202` (2020).

127. Scott, L. & Lucio, P. in *Advances in Diverse Industrial Applications of Nanocomposites* (ed Boreddy, R.) Ch. 21 (IntechOpen, Rijeka, 2011). `https://doi.org/10.5772/15624`.

128. Ren, L. & Chen, B. Proximity effect in electron beam lithography. *Proceedings. 7th International Conference on Solid-State and Integrated Circuits Technology, 2004.* **1,** 579–582 vol.1 (2004).

129. Prakash, S. & Yeom, J. in *Nanofluidics and Microfluidics* (eds Prakash, S. & Yeom, J.) 87–170 (William Andrew Publishing, 2014). ISBN: 978-1-4377-4469-9. `https://www.sciencedirect.com/science/article/pii/B9781437744699000044`.

130. Åstrand, M., Frisk, T., Ohlin, H. & Vogt, U. Understanding dose correction for high-resolution 50 kV electron-beam lithography on thick resist layers. *Micro and Nano Engineering* **16,** 100141. ISSN: 2590-0072. `https://www.sciencedirect.com/science/article/pii/S2590007222000387` (2022).

131. Koleva, E. *et al.* Modeling approaches for electron beam lithography. *Journal of Physics: Conference Series* **1089,** 012016. ISSN: 1742-6596 1742-6588. `https://dx.doi.org/10.1088/1742-6596/1089/1/012016` (2018).

132. Zhou, J. & Yang, X. Monte Carlo simulation of process parameters in electron beam lithography for thick resist patterning. *Journal of Vacuum Science & Technology B: Microelectronics and Nanometer Structures Processing, Measurement, and Phenomena* **24,** 1202–1209. `https://avs.scitation.org/doi/abs/10.1116/1.2192543` (2006).

133. Soo-Young, L. & Cook, B. D. PYRAMID-a hierarchical, rule-based approach toward proximity effect correction. I. Exposure estimation. *IEEE Transactions on Semiconductor Manufacturing* **11,** 108–116. ISSN: 1558-2345 (1998).

134. Wind, S. J., Gerber, P. D. & Rothuizen, H. Accuracy and efficiency in electron beam proximity effect correction. *Journal of Vacuum Science & Technology B: Microelectronics and Nanometer Structures Processing, Measurement, and Phenomena* **16,** 3262–3268. `https://avs.scitation.org/doi/abs/10.1116/1.590361` (1998).

135. Pala, N. & Karabiyik, M. in *Encyclopedia of Nanotechnology* (ed Bhushan, B.) 1033–1057 (Springer Netherlands, Dordrecht, 2016). ISBN: 978-94-017-9780-1. `https://doi.org/10.1007/978-94-017-9780-1_344`.

136. Goldstein, J. I. *et al. Scanning Electron Microscopy and X-Ray Microanalysis* ISBN: 978-0-306-47292-3 (Springer New York, NY, 2003).

137. Chen, Y., Peng, K. & Cui, Z. Fabrication of ultra-short T gates by a two-step electron beam lithography process. *Microelectronic Engineering* **73-74,** 662–665. ISSN: 0167-9317. `https://www.sciencedirect.com/science/article/pii/S0167931704001789` (2004).

138. Koller, D. M. *et al.* Three-dimensional SU-8 sub-micrometer structuring by electron beam lithography. *Microelectronic Engineering* **85,** 1639–1641. ISSN: 0167-9317. `https://www.sciencedirect.com/science/article/pii/S0167931708001603` (2008).

139. Koller, D. M. *et al.* Direct fabrication of micro/nano fluidic channels by electron beam lithography. *Microelectronic Engineering* **86,** 1314–1316. ISSN: 0167-9317. `https://www.sciencedirect.com/science/article/pii/S0167931708005352` (2009).

140. Abu Hatab, N. A., Oran, J. M. & Sepaniak, M. J. Surface-Enhanced Raman Spectroscopy Substrates Created via Electron Beam Lithography and Nanotransfer Printing. *ACS Nano* **2.** doi: 10.1021/nn7003487, 377–385. ISSN: 1936-0851. `https://doi.org/10.1021/nn7003487` (2008).

141. Bhandari, D. *et al.* Stamping plasmonic nanoarrays on SERS-supporting platforms. *Journal of Raman Spectroscopy* **42,** 1916–1924. ISSN: 0377-0486. `https://analyticalsciencejournals.onlinelibrary.wiley.com/doi/abs/10.1002/jrs.2940` (2011).

142. Adya, A. K. & Canetta, E. in *Animal Biotechnology (Second Edition)* (eds Verma, A. S. & Singh, A.) 309–326 (Academic Press, Boston, 2020). ISBN: 978-0-12-811710-1. `https://www.sciencedirect.com/science/article/pii/B9780128117101000148`.

143. Ferraro, J. R. *Introductory Raman Spectroscopy, Second Edition* 2nd ed. ISBN: 9780122541056 (Academic Press, 2003).

144. Misra, A. K., Sharma, S. K., Acosta, T. E., Porter, J. N. & Bates, D. E. Single-Pulse Standoff Raman Detection of Chemicals from 120 m Distance during Daytime. *Applied Spectroscopy* **66,** 1279–1285. ISSN: 0003-7028. `https://doi.org/10.1366/12-06617` (2012).

145. Misra, A. K., Sharma, S. K., Acosta, T. E., Porter, J. N. & Bates, D. E. Single-Pulse Standoff Raman Detection of Chemicals from 120 m Distance during Daytime. *Applied Spectroscopy* **66,** 1279–1285. ISSN: 0003-7028. `https://doi.org/10.1366/12-06617` (2012).

146. Trentelman, K. & Turner, N. Investigation of the painting materials and techniques of the late-15th century manuscript illuminator Jean Bourdichon. *Journal of Raman Spectroscopy* **40,** 577–584. ISSN: 0377-0486. `https://doi.org/10.1002/jrs.2186` (2009).

147. Haran, G. Single-Molecule Raman Spectroscopy: A Probe of Surface Dynamics and Plasmonic Fields. *Accounts of Chemical Research* **43,** 1135–1143. ISSN: 0001-4842. `https://doi.org/10.1021/ar100031v` (2010).

148. Langer, J. *et al.* Present and Future of Surface-Enhanced Raman Scattering. *ACS Nano* **14.** doi: 10.1021/acsnano.9b04224, 28–117. ISSN: 1936-0851. `https://doi.org/10.1021/acsnano.9b04224` (2020).

149. Vourdas, N., Boudouvis, A. G. & Gogolides, E. Plasma etch rate measurements of thin PMMA films and correlation with the glass transition temperature. *Journal of Physics: Conference Series* **10,** 405. ISSN: 1742-6596 1742-6588. `https://dx.doi.org/10.1088/1742-6596/10/1/099` (2005).

150. Gupta, V., Madaan, N., Jensen, D. S., Kunzler, S. C. & Linford, M. R. Hydrogen Plasma Treatment of Silicon Dioxide for Improved Silane Deposition. *Langmuir* **29.** doi: 10.1021/la304491x, 3604–3609. ISSN: 0743-7463. `https://doi.org/10.1021/la304491x` (2013).

151. Ratner, B. D. & Hoffman, A. S. in *Biomaterials Science (Third Edition)* (eds Ratner, B. D., Hoffman, A. S., Schoen, F. J. & Lemons, J. E.) 259–276 (Academic Press, 2013). ISBN: 978-0-12-374626-9. `https://www.sciencedirect.com/science/article/pii/B9780080877808000279`.

152. Yoon, G. *et al.* Fabrication of three-dimensional suspended, interlayered and hierarchical nanostructures by accuracy-improved electron beam lithography overlay. *Scientific Reports* **7,** 6668. ISSN: 2045-2322. `https://doi.org/10.1038/s41598-017-06833-5` (2017).

153. Zheng, Y. *et al.* Gutenberg-Style Printing of Self-Assembled Nanoparticle Arrays: Electrostatic Nanoparticle Immobilization and DNA-Mediated Transfer. *Angewandte Chemie* **123,** 4490–4494. ISSN: 0044-8249. `https://onlinelibrary.wiley.com/doi/abs/10.1002/ange.201006991` (2011).

154. Zhu, S., Fan, C., Wang, J., He, J. & Liang, E. Surface-enhanced Raman scattering of 4-mercaptobenzoic acid and hemoglobin adsorbed on self-assembled Ag monolayer films with different shapes. *Applied Physics A* **117,** 1075–1083. ISSN: 1432-0630. `https://doi.org/10.1007/s00339-014-8548-3` (2014).

155. Jiao, Y. *et al.* Patterned nanoporous gold as an effective SERS template. *Nanotechnology* **22,** 295302. ISSN: 0957-4484. `https://dx.doi.org/10.1088/0957-4484/22/29/295302` (2011).

156. Ma, Q. *et al.* Surface-enhanced Raman scattering substrate based on cysteamine-modified gold nanoparticle aggregation for highly sensitive pentachlorophenol detection. *RSC Advances* **6,** 85285–85292. ISSN: 2046-2069. `https://dx.doi.org/10.1039/c6ra15774b` (2016).

157. Lee, J. B. *et al.* Template Dissolution Interfacial Patterning of Single Colloids for Nanoelectrochemistry and Nanosensing. *ACS Nano* **14.** doi: 10.1021/acsnano.0c09319, 17693–17703. ISSN: 1936-0851. `https://doi.org/10.1021/acsnano.0c09319` (2020).

158. Indrasekara, A. S. D. S. *et al.* Dimeric Gold Nanoparticle Assemblies as Tags for SERS-Based Cancer Detection. *Advanced Healthcare Materials* **2,** 1370–1376. ISSN: 2192-2640. `https://onlinelibrary.wiley.com/doi/abs/10.1002/adhm.201200370` (2013).

159. Guo, R. *et al.* Controlling quantum dot emission by plasmonic nanoarrays. *Optics Express* **23,** 28206–28215. `https://opg.optica.org/oe/abstract.cfm?URI=oe-23-22-28206` (2015).

160. Rakovich, A., Albella, P. & Maier, S. A. Plasmonic Control of Radiative Properties of Semiconductor Quantum Dots Coupled to Plasmonic Ring Cavities. *ACS Nano* **9,** 2648–2658. ISSN: 1936-0851. `https://doi.org/10.1021/nn506433e` (2015).

161. Yu, H. S. C. *et al.* Precise Capillary-Assisted Nanoparticle Assembly in Reusable Templates. *Particle & Particle Systems Characterization* **39,** 2100288. ISSN: 0934-0866. `https://onlinelibrary.wiley.com/doi/abs/10.1002/ppsc.202100288` (2022).

162. Pioli, R. *et al.* Sequential capillarity-assisted particle assembly in a microfluidic channel. *Lab on a Chip* **21,** 888–895. ISSN: 1473-0197. `http://dx.doi.org/10.1039/D0LC00962H` (2021).

163. Huang, L. *et al.* Sub-wavelength patterned pulse laser lithography for efficient fabrication of large-area metasurfaces. *Nature Communications* **13,** 5823. ISSN: 2041-1723. `https://doi.org/10.1038/s41467-022-33644-8` (2022).

164. Feng, C. L. *et al.* Functional Quantum-Dot/Dendrimer Nanotubes for Sensitive Detection of DNA Hybridization. *Small* **4,** 566–571. ISSN: 1613-6810. `https://doi.org/10.1002/smll.200700453` (2008).

165. Mamedov, A. A., Belov, A., Giersig, M., Mamedova, N. N. & Kotov, N. A. Nanorainbows: Graded Semiconductor Films from Quantum Dots. *Journal of the American Chemical Society* **123.** doi: 10.1021/ja015857q, 7738–7739. ISSN: 0002-7863. `https://doi.org/10.1021/ja015857q` (2001).

166. Franzl, T., Klar, T. A., Schietinger, S., Rogach, A. L. & Feldmann, J. Exciton Recycling in Graded Gap Nanocrystal Structures. *Nano Letters* **4,** 1599–1603. ISSN: 1530-6984. `https://doi.org/10.1021/nl049322h` (2004).

167. Chen, H. *et al.* Drug loaded multilayered gold nanorods for combined photothermal and chemotherapy. *Biomaterials Science* **2,** 996–1006. ISSN: 2047-4830 (2014).

168. Feng, L. *et al.* Preparation of gold nanorods with different aspect ratio and the optical response to solution refractive index. *Journal of Experimental Nanoscience* **10,** 258–267. ISSN: 1745-8080 (2015).

169. Fuller, M. & Kper, I. Polyelectrolyte-Coated Gold Nanoparticles: The Effect of Salt and Polyelectrolyte Concentration on Colloidal Stability. *Polymers* **10,** 1336. ISSN: 2073-4360 (2018).

170. Seker, U. O. S., Ozel, T. & Demir, H. V. Peptide-Mediated Constructs of Quantum Dot Nanocomposites for Enzymatic Control of Nonradiative Energy Transfer. *Nano Letters* **11,** 1530–1539. ISSN: 1530-6984. `https://doi.org/10.1021/nl104295b` (2011).

171. Zhao, J. *et al.* Efficient CdSe/CdS Quantum Dot Light-Emitting Diodes Using a Thermally Polymerized Hole Transport Layer. *Nano Letters* **6.** doi: 10.1021/nl052417e, 463–467. ISSN: 1530-6984. `https://doi.org/10.1021/nl052417e` (2006).

172. Zhang, H., Su, Q. & Chen, S. Suppressing Förster Resonance Energy Transfer in Close-Packed Quantum-Dot Thin Film: Toward Efficient Quantum-Dot Light-Emitting Diodes with External Quantum Efficiency over 21.6%. *Advanced Optical Materials* **8,** 1902092. ISSN: 2195-1071. `https://onlinelibrary.wiley.com/doi/abs/10.1002/adom.201902092` (2020).

173. Jiang, Z. *et al.* Ultra-sensitive tandem colloidal quantum-dot photodetectors. *Nanoscale* **7,** 16195–16199. ISSN: 2040-3364. `https://dx.doi.org/10.1039/c5nr03791c` (2015).

174. Kim, J. *et al.* A skin-like two-dimensionally pixelized full-color quantum dot photodetector. *Science Advances* **5,** eaax8801. `https://www.science.org/doi/abs/10.1126/sciadv.aax8801` (2019).

175. Livache, C. *et al.* A colloidal quantum dot infrared photodetector and its use for intraband detection. *Nature Communications* **10,** 2125. ISSN: 2041-1723. `https://doi.org/10.1038/s41467-019-10170-8` (2019).

176. Gole, A., Jana, N. R., Selvan, S. T. & Ying, J. Y. Langmuir-Blodgett Thin Films of Quantum Dots: Synthesis, Surface Modification, and Fluorescence Resonance Energy Transfer (FRET) Studies. *Langmuir* **24.** doi: 10.1021/la8000224, 8181–8186. ISSN: 0743-7463. `https://doi.org/10.1021/la8000224` (2008).

177. Ji, X. *et al.* Surface Chemistry Studies of (CdSe)ZnS Quantum Dots at the Air-Water Interface. *Langmuir* **21.** doi: 10.1021/la050327j, 5377–5382. ISSN: 0743-7463. `https://doi.org/10.1021/la050327j` (2005).

178. Nguyen, T. C., Can, T. T. T. & Choi, W.-S. Optimization of Quantum Dot Thin Films using Electrohydrodynamic Jet Spraying for Solution-Processed Quantum Dot Light-Emitting Diodes. *Scientific Reports* **9,** 13885. ISSN: 2045-2322. `https://doi.org/10.1038/s41598-019-50181-5` (2019).

179. Li, M. *et al.* CdTe nanocrystal–polymer composite thin film without fluorescence resonance energy transfer by using polymer nanospheres as nanocrystal carriers. *Journal of Colloid and Interface Science* **346,** 330–336. ISSN: 0021-9797. `https://www.sciencedirect.com/science/article/pii/S0021979710002900` (2010).

180. Cao, W. *et al.* Difference in hot carrier cooling rate between Langmuir–Blodgett and drop cast PbS QD films due to strong electron–phonon coupling. *Nanoscale* **9,** 17133–17142. ISSN: 2040-3364. `https://dx.doi.org/10.1039/c7nr05247b` (2017).

181. Samanta, A., Zhou, Y., Zou, S., Yan, H. & Liu, Y. Fluorescence Quenching of Quantum Dots by Gold Nanoparticles: A Potential Long Range Spectroscopic

Ruler. *Nano Letters* **14.** doi: 10.1021/nl501709s, 5052–5057. ISSN: 1530-6984. `https://doi.org/10.1021/nl501709s` (2014).

182. Zhao, L., Ming, T., Shao, L., Chen, H. & Wang, J. Plasmon-Controlled Förster Resonance Energy Transfer. *The Journal of Physical Chemistry C* **116.** doi: 10.1021/jp300916a, 8287–8296. ISSN: 1932-7447. `https://doi.org/10.1021/jp300916a` (2012).

183. Shahbazyan, T. V. Local Density of States for Nanoplasmonics. *Physical Review Letters* **117.** ISSN: 0031-9007. `https://dx.doi.org/10.1103/physrevlett.117.207401` (2016).

184. Gersten, J. I. & Nitzan, A. Accelerated energy transfer between molecules near a solid particle. *Chemical Physics Letters* **104,** 31–37. ISSN: 0009-2614. `https://www.sciencedirect.com/science/article/pii/0009261484853002` (1984).

185. Dung, H. T., Knöll, L. & Welsch, D.-G. Intermolecular energy transfer in the presence of dispersing and absorbing media. *Physical Review A* **65.** ISSN: 1050-2947. `https://dx.doi.org/10.1103/physreva.65.043813` (2002).

186. Hsu, L.-Y., Ding, W. & Schatz, G. C. Plasmon-Coupled Resonance Energy Transfer. *The Journal of Physical Chemistry Letters* **8,** 2357–2367. `https://doi.org/10.1021/acs.jpclett.7b00526` (2017).

187. Su, X.-R., Zhang, W., Zhou, L., Peng, X.-N. & Wang, Q.-Q. Plasmon-enhanced Förster energy transfer between semiconductor quantum dots: multipole effects. *Optics Express* **18,** 6516–6521. `https://opg.optica.org/oe/abstract.cfm?URI=oe-18-7-6516` (2010).

188. Wiącek, A. E., Gozdecka, A., Jurak, M., Przykaza, K. & Terpiłowski, K. Wettability of plasma modified glass surface with bioglass layer in polysaccharide

solution. *Colloids and Surfaces A: Physicochemical and Engineering Aspects* **551,** 185–194. ISSN: 09277757 (2018).

189. Chernomordik, B. D., Marshall, A. R., Pach, G. F., Luther, J. M. & Beard, M. C. Quantum Dot Solar Cell Fabrication Protocols. *Chemistry of Materials* **29,** 189–198. ISSN: 0897-4756. `https://dx.doi.org/10.1021/acs.chemmater.6b02939` (2017).

190. Noh, M. *et al.* Fluorescence quenching caused by aggregation of water-soluble CdSe quantum dots. *Colloids and Surfaces A: Physicochemical and Engineering Aspects* **359,** 39–44. ISSN: 0927-7757. `https://www.sciencedirect.com/science/article/pii/S092777571000083X` (2010).

191. Oh, I. *et al.* Enhancement of Energy Transfer Efficiency with Structural Control of Multichromophore Light-Harvesting Assembly. *Advanced Science* **7,** 2001623. ISSN: 2198-3844. `https://doi.org/10.1002/advs.202001623` (2020).

192. Grevtseva, I. G. *et al.* The structural and luminescence properties of plexcitonic structures based on Ag2S/l-Cys quantum dots and Au nanorods. *RSC Advances* **12,** 6525–6532. `http://dx.doi.org/10.1039/D1RA08806H` (2022).

193. Dhami, S. *et al.* PHTHALOCYANINE FLUORESCENCE AT HIGH CONCENTRATION: DIMERS OR REABSORPTION EFFECT? *Photochemistry and Photobiology* **61,** 341–346. ISSN: 0031-8655. `https://onlinelibrary.wiley.com/doi/abs/10.1111/j.1751-1097.1995.tb08619.x` (1995).

194. Yang, P., Li, C. L. & Murase, N. Highly Photoluminescent Multilayer QD-Glass Films Prepared by LbL Self-Assembly. *Langmuir* **21,** 8913–8917. ISSN: 0743-7463. `https://doi.org/10.1021/la050397q` (2005).

195. Lunz, M., Bradley, A. L., Chen, W.-Y. & Gun'ko, Y. K. Förster resonant energy transfer in quantum dot layers. *Superlattices and Microstructures* **47,** 98–102. ISSN: 0749-6036. `https://www.sciencedirect.com/science/article/pii/S0749603609001220` (2010).

196. Richardson, J. J., Björnmalm, M. & Caruso, F. Technology-driven layer-by-layer assembly of nanofilms. *Science* **348.** doi: 10.1126/science.aaa2491, aaa2491. `https://doi.org/10.1126/science.aaa2491` (2015).

197. Caruso, F., Lichtenfeld, H., Donath, E. & Möhwald, H. Investigation of Electrostatic Interactions in Polyelectrolyte Multilayer Films: Binding of Anionic Fluorescent Probes to Layers Assembled onto Colloids. *Macromolecules* **32,** 2317–2328. ISSN: 0024-9297. `https://doi.org/10.1021/ma980674i` (1999).

198. Kokufuta, E. & Takahashi, K. Adsorption of poly(diallyldimethylammonium chloride) on colloid silica from water and salt solution. *Macromolecules* **19.** doi: 10.1021/ma00156a019, 351–354. ISSN: 0024-9297. `https://doi.org/10.1021/ma00156a019` (1986).

199. Muskens, O. L., Giannini, V., Sánchez-Gil, J. A. & Gómez Rivas, J. Strong Enhancement of the Radiative Decay Rate of Emitters by Single Plasmonic Nanoantennas. *Nano Letters* **7.** doi: 10.1021/nl0715847, 2871–2875. ISSN: 1530-6984. `https://doi.org/10.1021/nl0715847` (2007).

200. Ozel, T. *et al.* Observation of Selective Plasmon-Exciton Coupling in Nonradiative Energy Transfer: Donor-Selective versus Acceptor-Selective Plexcitons. *Nano Letters* **13.** doi: 10.1021/nl4009106, 3065–3072. ISSN: 1530-6984. `https://doi.org/10.1021/nl4009106` (2013).

201. Abadeer, N. S., Brennan, M. R., Wilson, W. L. & Murphy, C. J. Distance and Plasmon Wavelength Dependent Fluorescence of Molecules Bound to Silica-

Coated Gold Nanorods. *ACS Nano* **8.** doi: 10.1021/nn502887j, 8392–8406. ISSN: 1936-0851. `https://doi.org/10.1021/nn502887j` (2014).

202. Li, M. *et al.* Size-Dependent Energy Transfer between CdSe/ZnS Quantum Dots and Gold Nanoparticles. *The Journal of Physical Chemistry Letters* **2,** 2125–2129. `https://doi.org/10.1021/jz201002g` (2011).

203. Jennings, T. L., Singh, M. P. & Strouse, G. F. Fluorescent Lifetime Quenching near d = 1.5 nm Gold Nanoparticles: Probing NSET Validity. *Journal of the American Chemical Society* **128.** doi: 10.1021/ja0583665, 5462–5467. ISSN: 0002-7863. `https://doi.org/10.1021/ja0583665` (2006).

204. Cao, J. *et al.* Plasmon-Coupled Förster Resonance Energy Transfer between Silicon Quantum Dots. *The Journal of Physical Chemistry C* **123,** 23604–23609. ISSN: 1932-7447. `https://doi.org/10.1021/acs.jpcc.9b05637` (2019).

205. Zong, H., Wang, X., Mu, X., Wang, J. & Sun, M. Plasmon-Enhanced Fluorescence Resonance Energy Transfer. *The Chemical Record* **19,** 818–842. ISSN: 1527-8999. `https://doi.org/10.1002/tcr.201800181` (2019).

206. Bohlen, J. *et al.* Plasmon-assisted Förster resonance energy transfer at the single-molecule level in the moderate quenching regime. *Nanoscale* **11,** 7674–7681. ISSN: 2040-3364. `http://dx.doi.org/10.1039/C9NR01204D` (2019).

207. Jain, P. K., Lee, K. S., El-Sayed, I. H. & El-Sayed, M. A. Calculated Absorption and Scattering Properties of Gold Nanoparticles of Different Size, Shape, and Composition: Applications in Biological Imaging and Biomedicine. *The Journal of Physical Chemistry B* **110.** doi: 10.1021/jp057170o, 7238–7248. ISSN: 1520-6106. `https://doi.org/10.1021/jp057170o` (2006).

208. Li, M., Cushing, S. K. & Wu, N. Plasmon-enhanced optical sensors: a review. *The Analyst* **140,** 386–406. ISSN: 0003-2654. `https://dx.doi.org/10.1039/c4an01079e` (2015).

209. Lee, E. M. Y. & Tisdale, W. A. Determination of Exciton Diffusion Length by Transient Photoluminescence Quenching and Its Application to Quantum Dot Films. *The Journal of Physical Chemistry C* **119,** 9005–9015. ISSN: 1932-7447. `https://doi.org/10.1021/jp512634c` (2015).

210. Carretero-Palacios, S., Jiménez-Solano, A. & Míguez, H. Plasmonic Nanoparticles as Light-Harvesting Enhancers in Perovskite Solar Cells: A User's Guide. *ACS Energy Letters* **1,** 323–331. `https://doi.org/10.1021/acsenergylett.6b00138` (2016).

211. Sastry, M., Lala, N., Patil, V., Chavan, S. P. & Chittiboyina, A. G. Optical Absorption Study of the Biotin-Avidin Interaction on Colloidal Silver and Gold Particles. *Langmuir* **14,** 4138–4142. ISSN: 0743-7463. `https://doi.org/10.1021/la9800755` (1998).

212. Gole, A. & Murphy, C. J. Biotin-Streptavidin-Induced Aggregation of Gold Nanorods: Tuning Rod-Rod Orientation. *Langmuir* **21,** 10756–10762. ISSN: 0743-7463. `https://doi.org/10.1021/la0512704` (2005).

213. Fullam, S., Rao, S. N. & Fitzmaurice, D. Noncovalent Self-Assembly of Silver Nanocrystal Aggregates in Solution. *The Journal of Physical Chemistry B* **104,** 6164–6173. ISSN: 1520-6106. `https://dx.doi.org/10.1021/jp0006173` (2000).

214. Tian, L., Chen, E., Gandra, N., Abbas, A. & Singamaneni, S. Gold Nanorods as Plasmonic Nanotransducers: Distance-Dependent Refractive Index Sensitivity. *Langmuir* **28,** 17435–17442. ISSN: 0743-7463 (2012).

215. Kinnear, C. *et al.* Gold Nanorods: Controlling Their Surface Chemistry and Complete Detoxification by a Two-Step Place Exchange. *Angewandte Chemie International Edition* **52,** 1934–1938. ISSN: 1433-7851. `https://onlinelibrary.wiley.com/doi/abs/10.1002/anie.201208568` (2013).

216. Seyden-Penne, J. *Reductions by the alumino- and Borohydrides in organic synthesis* (Wiley-VCH, 1997).

217. He, J. *et al.* The facile removal of CTAB from the surface of gold nanorods. *Colloids and Surfaces B: Biointerfaces* **163,** 140–145. ISSN: 0927-7765. `https://www.sciencedirect.com/science/article/pii/S0927776517308597` (2018).

218. Deraedt, C. *et al.* Sodium borohydride stabilizes very active gold nanoparticle catalysts. *Chemical Communications* **50,** 14194–14196. ISSN: 1359-7345. `http://dx.doi.org/10.1039/C4CC05946H` (2014).

219. Ansar, S. M. *et al.* Removal of Molecular Adsorbates on Gold Nanoparticles Using Sodium Borohydride in Water. *Nano Letters* **13,** 1226–1229. ISSN: 1530-6984. `https://doi.org/10.1021/nl304703w` (2013).

220. Fuller, M. A. & Köper, I. Biomedical applications of polyelectrolyte coated spherical gold nanoparticles. *Nano Convergence* **6,** 11. ISSN: 2196-5404. `https://doi.org/10.1186/s40580-019-0183-4` (2019).

221. Pissuwan, D. & Niidome, T. Polyelectrolyte-coated gold nanorods and their biomedical applications. *Nanoscale* **7,** 59–65. ISSN: 2040-3364. `http://dx.doi.org/10.1039/C4NR04350B` (2015).

222. Gole, A. & Murphy, C. J. Polyelectrolyte-Coated Gold Nanorods: Synthesis, Characterization and Immobilization. *Chemistry of Materials* **17.** doi: 10.1021/cm048297d, 1325–1330. ISSN: 0897-4756. `https://doi.org/10.1021/cm048297d` (2005).

223. Manson, J., Kumar, D., Meenan, B. J. & Dixon, D. Polyethylene glycol functionalized gold nanoparticles: the influence of capping density on stability in various media. *Gold Bulletin* **44,** 99–105. ISSN: 2190-7579. `https://doi.org/10.1007/s13404-011-0015-8` (2011).

224. Moon, S., Won, Y. & Kim, D. Y. Analog mean-delay method for high-speed fluorescence lifetime measurement. *Optics Express* **17,** 2834–2849. `https://opg.optica.org/oe/abstract.cfm?URI=oe-17-4-2834` (2009).

225. *Lifetime Data of Selected Fluorophores* Accessed: 2023-02-22. `https://iss.com/resources#lifetime-data-of-selected-fluorophores`.

226. Himmelhaus, M., Krishnamoorthy, S. & Francois, A. Optical Sensors Based on Whispering Gallery Modes in Fluorescent Microbeads: Response to Specific Interactions. *Sensors* **10,** 6257–6274. ISSN: 1424-8220. `https://www.mdpi.com/1424-8220/10/6/6257` (2010).

227. Kuzuya, A., Numajiri, K., Kimura, M. & Komiyama, M. Single-Molecule Accommodation of Streptavidin in Nanometer-Scale Wells Formed in DNA Nanostructures. *Nucleic Acids Symposium Series* **52,** 681–682. ISSN: 0261-3166. `https://doi.org/10.1093/nass/nrn344` (2008).

228. Avvakumova, S. *et al.* in *Biomedical Applications of Functionalized Nanomaterials* (eds Sarmento, B. & das Neves, J.) 139–169 (Elsevier, 2018). ISBN: 978-0-323-50878-0. `https://www.sciencedirect.com/science/article/pii/B9780323508780000069`.

229. Gersten, J. & Nitzan, A. Spectroscopic properties of molecules interacting with small dielectric particles. *The Journal of Chemical Physics* **75,** 1139–1152. `https://aip.scitation.org/doi/abs/10.1063/1.442161` (1981).

230. Okamoto, K., Vyawahare, S. & Scherer, A. Surface-plasmon enhanced bright emission from CdSe quantum-dot nanocrystals. *Journal of the Optical Society of America B* **23,** 1674–1678. `https://opg.optica.org/josab/abstract.cfm?URI=josab-23-8-1674` (2006).